Spring 1-1-2014

From Material Design to Device: Structural and Thermodynamic Considerations for Solid-Phase Lithium-Ion Electrolytes

Brian E. Francisco
University of Colorado at Boulder, bfran33@gmail.com

Recommended Citation

Francisco, Brian E., "From Material Design to Device: Structural and Thermodynamic Considerations for Solid-Phase Lithium-Ion Electrolytes" (2014). *Mechanical Engineering Graduate Theses & Dissertations*. 98.
https://scholar.colorado.edu/mcen_gradetds/98

From Material Design to Device: Structural and Thermodynamic Considerations for Solid-Phase Lithium-Ion Electrolytes

by

Brian E. Francisco

B.S., Mechanical Engineering, University of New Haven, 2009

M.S., Mechanical Engineering, University of Colorado Boulder, 2011

A thesis submitted to the
Faculty of the Graduate School of the
University of Colorado in partial fulfillment
of the requirements for the degree of
Doctor of Philosophy
Department of Mechanical Engineering
2014

This thesis entitled:
From Material Design to Device: Structural and Thermodynamic Considerations for Solid-Phase Lithium-Ion Electrolytes
written by Brian E. Francisco
has been approved for the Department of Mechanical Engineering

Prof. Conrad Stoldt

Prof. Yifu Ding

Prof. John Daily

Prof. Todd Murray

Prof. Kurt Maute

Date

The final copy of this thesis has been examined by the signatories, and we find that both the content and the form meet acceptable presentation standards of scholarly work in the above mentioned discipline.

Francisco, Brian E. (Ph.D., Materials Science)

From Material Design to Device: Structural and Thermodynamic Considerations for Solid-Phase Lithium-Ion Electrolytes

Thesis directed by Prof. Conrad Stoldt

Too often, we check the battery status of our favorite gadget and wonder: "Is it going to make it?" At some point in the not-so-distant future, I believe we will not have to ask this question. Until then, it is the incremental movement of the boundaries of our understandings of energy storage sciences that bring us closer to the next breakthrough technology.

In this thesis, we investigate a material which may one day play a key role in enabling fast-charging, long-lasting energy storage devices: the solid-state electrolyte. While this material has begun to replace liquid electrolytes in batteries, we envisioned a potential use in supercapacitors as well. Our work in solid-state supercapacitor development involved the incorporation of a sulfide-based electrolyte system as both the separator and source of double-layer ions. We demonstrated supercapacitance through a nanostructuring of the electrode layers. While a working device is certainly a meaningful contribution to the field of solid-state energy storage, we desired a deeper understanding of the physics that enables the demonstrated supercapacitance.

To this end, we next undertook study of ion mobility in a solid-state electrolyte using an air-stable system based on lithium germanium phosphate. We synthesized materials with varying chemistries in order to obtain a better understanding of how structural substitutions affect lithium-ion movement. We discover that a common synthetic approach to "improving" electrolyte performance can have the unintended consequences of trapping lithium ions, leading to decreases in conductivity.

Going one step deeper, we ultimately undertook a detailed study of the thermodynamic parameters that govern ion conduction. Through a thorough analysis of structure, we were able to provide physical explanations for observed trends in activation energy and conductivity. Finally,

we provide strong evidence for a physical interpretation of entropy parameters based on the site occupancies of lithium ions.

It is hoped that the work conducted in the creation of this thesis can be used to guide forthcoming developments in the battery and supercapacitor communities. To control device operation, it is necessary to understand material function. To understand material function, it is necessary to understand governing parameters from the bottom up. This thesis contributes to a foundation from which to design the power source of tomorrow's favorite gadget.

Dedication

Some are born with the tools for success already in hand, while others must forge their own. I would like to dedicate this work to those who set goals outside of their comfort zones, and worked tenaciously to achieve them. There is truly nothing that cannot be accomplished with planning, focus, and drive.

Acknowledgements

I would like to acknowledge some colleagues for a willingness to indulge in technical discussions, share resources, and drop what they were doing to help when I walked in demanding something: Alex MacPherson, Ilya Lisenker, and Shikhar Jha.

As I'm sure is the case with any doctoral program, you can drive yourself mad without a counterbalance to the tremendous frustrations that come with exploring the unknown. I need to thank the great community of friends I've made during my time in Boulder for always planning some kind of relief. I'll carry the memories we've made in the great outdoors with me always.

Finally, I need to thank my family. While at times it was tough to articulate what it was I was doing here and why it was taking so long, not once did your support or pride waver. This confidence in me often picked me up when I had lost my own. Mom, you were always there to listen to my complicated, often technical tales and offer your best support. Dad, you always made sure I knew how proud everyone was, and that when you work hard, you can reach any goal you set. Chris, you've been extremely patient as our friendship has often been on hold during this work. I hope that at the close of the last chapter of this thesis, we begin a new chapter of brotherhood.

Contents

Chapter

Tables

Table

Figures

Figure

Chapter 1

State-of-the-Art in Non-Battery Energy Storage

1.1 Introduction

Current state-of-the-art supercapacitors (SCs) can generally be divided into two classes based upon on the charge storage mechanism: Electric Double Layer Capacitors (EDLCs) and Pseudocapacitors. EDLCs store charge by the reversible development of a double layer of ions at electrolyte/electrode interfaces within the device. Figure 1.1 shows a depiction of the common state-of-the-art architecture. EDLCs usually employ simple carbon materials and demonstrate stable cycling characteristics. While the specific power of EDLC devices can be high (>10 kW/kg), specific energy is generally low (<10 Wh/kg) [10]. In an effort to increase the specific energy of SCs, devices that store charge via reversible surface-redox reactions have been developed. As the reactions that take place are fast and occur only on the surface, this type of charge storage was termed pseudocapacitance and devices based on this principle called Pseudocapacitors. Most often, the electrodes of these devices employ a conducting polymer or metal oxide material that is reversibly doped with ions from the electrolyte. This process causes volume changes which eventually lead to capacity fade with cycling. The specific energy of pseudocapacitors is higher than EDLCs, but as the doping process is slower than a double layer formation, they often have lower specific power.

Performance of SCs is defined in terms of capacitance, energy, and power. Capacitance, C, is a function charge carriers (ions), electrolyte solution (solvents), and electrode/electrolyte interfacial area in an EDLC, and interfacial area and doping capacity in pseudocapacitors. Specific energy, E, is defined $\mathrm{E} = \frac{1}{2}\mathrm{C}\cdot\mathrm{V}^2$ where V is the maximum voltage reached during charging. While specific

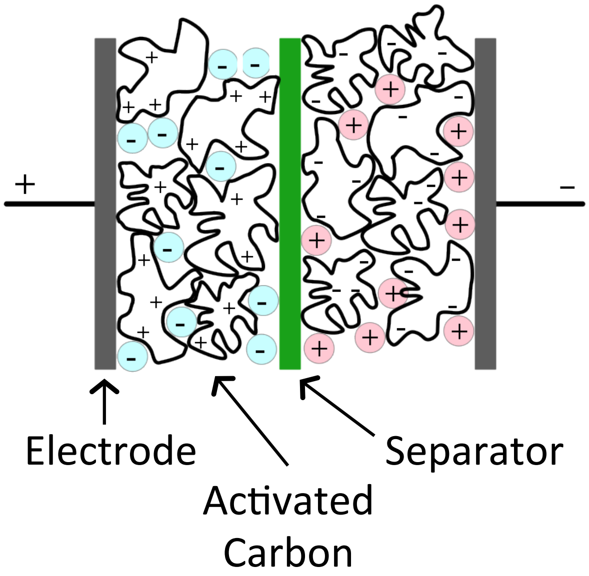

Figure 1.1: Electric Double Layer Capacitors (EDLCs) commonly employ activated carbon with liquid electrolytes to create electrodes with high surface areas, which are capable of high specific capacitance.

capacitance is important, the dominant factor in achieving high specific energy is the operating voltage of the supercapacitor. Specific power, P, is governed by the relation $P = V^2/(4 \cdot ESR)$ where ESR is the Equivalent Series Resistance of the device. ESR is a combination of the bulk electrode, interfacial, and bulk electrolyte resistances to charge propagation. Liquid electrolytes have low resistance to ion conduction and carbon electrodes have negligible resistance to electron flow, so devices employing these components usually have high specific power. In pseudocapacitors, there is an additional charge-transfer resistance adding to the ESR, which slightly reduces power capability.

1.2 Electrolytes

State-of-the-art electrolytes used in SCs are either liquids or polymers. A liquid electrolyte consists of an acid (H_2SO_4), base (KOH), or neutral salt ($LiPF_6$) which dissociates in an aqueous or organic solvent, providing the charged ions to build a double layer [11, 4]. Aqueous solvents have the advantages of being non-toxic and environmentally friendly, but limit cell voltage to 1 V due to the electrochemical decomposition of water at 1.23 V. Organic solvents such as ethylene carbonate have stability windows up to 3 V, but are toxic, environmentally harmful, and most seriously, flammable. Liquid electrolytes offer ease of infiltration into highly porous electrodes that can contribute to high capacitance, but come with serious risks. Leakage of the electrolyte from the cell will be harmful to both humans and the environment. The flammability of the organic solvents creates a roadblock to use in electric or hybrid vehicles, as the solvent may catch fire in the event of an accident or improper cell management.

Polymer electrolytes have been developed to reduce the risks of electrolyte leakage and flammability concerns. This type of electrolyte consists of a polymer such as polyvinyl alcohol (PVA) doped with an acidic salt (H_3PO_4) or basic salt (KOH) [12, 13]. The PVA acts as a solvent for the acidic or basic salts, and consequently both cations and anions are mobile. Nafion, an ionomer developed by the DuPont chemical corporation, has also been adopted for its proton conduction abilities [8, 2]. PVA-acid and Nafion are the most common polymer electrolytes, and are most often used in cells with pseudocapacitive polymer electrodes that dope/de-dope with protons. These polymer electrolytes offer the advantages of flexibility and solvent leakage is minimal. However, flexible supercapacitors are currently a niche application [7]. Drawbacks of using polymer electrolytes include lower conductivity than liquids and the temperature limits of the polymer material.

1.3 Electrodes

Electrodes used in state-of-the-art SCs can be broadly divided into those for EDLCs and those for pseudocapacitors. For EDLCs, several allotropes of carbon are employed in various electrode architectures. Carbon nanotubes, activated carbon / carbon black, and graphene are all currently used.

Carbon nanotubes, whether multi-wall or single-wall, are engineered into mesoporous networks which offer easy infiltration of electrolyte, high surface area, and very low electrical resistance [3]. Nanotube networks are most often created by dispersing CNTs in a liquid solution to form an ink and painting them onto a current collector or electrode separator [4]. This makes networks of carbon nanotubes both an effective and easy-to-manufacture electrode. Electrodes of this architecture have demonstrated specific capacitance upwards of 200 F/g.

Activated carbon (AC) has a very high surface area, but often the pores contributing to the surface area are so small that ions in solution cannot access them. Unless pore size is tuned to ion size, a portion of the available surface area of AC will not contribute to double layer capacitance [9]. Carbon black (CB) can also provide a high surface area for double layer capacitors and is a common byproduct of industrial processes, meaning lower cost. However, the amorphous nature of CB leads to higher resistivity. When AC and CB are used in powder forms, they require binders to hold them together to form an electrode [13, 5]. The inclusion of a binder, which has no energy storage capability, lowers the specific energy and power of the device. The best electrodes made with AC or CB commonly display specific capacitance of 100-200 F/g [11].

Graphene has been used in a limited number of SC devices to date. Graphene has been more often employed in conjunction with polymers in pseudocapacitive devices and is underdeveloped for use in EDLCs [2, 14]. While graphene can provide very high surface area, there are tremendous challenges in manufacturing an electrode that utilizes its potential. The best graphene-based SC demonstrated so far required a multi-step, time-consuming, resource-inefficient fabrication process [12].

Electrode materials for pseudocapacitors typically involve a material that undergoes reversible redox reactions with H^+ ions or the lighter of the alkali metals (Li, Na, K) to store charge in the surface region. One class of pseudocapacitive materials is conducting polymers, of which the most commonly used is polyaniline (PANI). While polyaniline electrodes have demonstrated high capacitance (480 F/g), the PANI undergoes swelling during the H^+ doping process which leads to capacity fade with cycling [14]. PANI based electrodes are also constructed with conductive additives to boost electron conductivity within the electrode, which add unnecessary weight. Oxide materials, such as RuO_2 and MnO_2, are also used as pseudocapacitive materials that undergo reversible doping with protons or the lighter of the alkali metals [6]. While these materials have each demonstrated the potential for high capacitance (~1000 F/g), each faces large roadblocks for wide scale implementation. RuO_2 is too expensive to be considered a viable commercial option, and MnO_2 has a low electrical conductivity which means specific power of packaged devices will be lower than those based on other materials.

Finally, there has been recent interest in using materials typically considered to belong in batteries as the pseudocapacitive electrode in combination with an EDLC electrode in an asymmetric SC architecture. In this case, the device is often referred to as a hybrid supercapacitor/battery or hybrid cell. Materials such as TiO_2, $Li_4Ti_5O_{12}$, and $LiMn_2O_4$ offer reversible intercalation of ions from the electrolyte while operating at a higher voltage relative to a reference couple such as Li/Li^+ [1]. If incorporated as a negative electrode, these materials may effectively set the cell lower operating voltage to that of their redox reaction, which shifts the maximum and average cell voltage to higher values, thus increasing energy density.

1.4 An Emerging Opportunity - Solid-State Architecture

While a great number of combinations of electrolytes and electrodes have been studied for use in SCs and hybrid SCs, there are no currently available options that achieve high specific energy and power while also remaining safe and reliable for varied applications. All-solid-state device architectures offer a number of attractive characteristics as compared to architectures that include liquid or polymeric materials. First and foremost, all-solid-state architectures are safe and durable as compared to their liquid counterparts. They are not, to our knowledge, flammable, hazardous, or subject to thermal runaway. They also do not run the risk of solvent leakage and/or corrosion. They are also stable over a very large voltage range up to 10 V. As a consequence, all-solid-state architectures necessitate fewer safety precautions in the final packaged form. Without liquid or polymeric materials, cycling stability is also improved since unwanted interfacial chemical reactions are minimized, and similarly, self-discharge (in solid-state batteries) is minimal or nonexistent at conventional operating temperatures. This class of device is also stable over a much wider temperature range than liquid based systems.

Based on this emerging opportunity presented by solid-state architectures, we embarked on a project to create a simple solid-state supercapacitor. In Chapter 2, we detail a device created with a sulfide-based solid electrolyte, including electrochemical performance and thoughts on future development.

References

[1] Glenn G Amatucci, Fadwa Badway, Aurelien Du Pasquier, and Tao Zheng. An Asymmetric Hybrid Nonaqueous Energy Storage Cell. Journal of The Electrochemical Society, 148(8):A930–A939, 2001.

[2] Bong Gill Choi, Jinkee Hong, Won Hi Hong, Paula T Hammond, and HoSeok Park. Facilitated Ion Transport in All-Solid-State Flexible Supercapacitors. ACS nano, 5(9):7205–7213, 2011.

[3] E Frackowiak and F Beguin. Electrochemical storage of energy in carbon nanotubes and nanostructured carbons. Carbon, 40(10):1775–1787, 2002.

[4] L. Hu, J.W. Choi, Y. Yang, S. Jeong, F. La Mantia, L.F. Cui, and Y. Cui. Highly conductive paper for energy-storage devices. Proceedings of the National Academy of Sciences, 106(51):21490–21494, 2009.

[5] A Krause, P Kossyrev, M Oljaca, S Passerini, M Winter, and A Balducci. Electrochemical double layer capacitor and lithium-ion capacitor based on carbon black. Journal Of Power Sources, 196(20):8836–8842, October 2011.

[6] Seung Woo Lee, Junhyung Kim, Shuo Chen, Paula T Hammond, and Yang Shao-Horn. Carbon Nanotube/Manganese Oxide Ultrathin Film Electrodes for Electrochemical Capacitors. ACS nano, 4(7):3889–3896, 2010.

[7] Qiang Liu, Munir H Nayfeh, and Siu-Tung Yau. Brushed-on flexible supercapacitor sheets using a nanocomposite of polyaniline and carbon nanotubes. Journal Of Power Sources, 195(21):7480–7483, November 2010.

[8] F Lufrano and P Staiti. Performance improvement of Nafion based solid state electrochemical supercapacitor. Electrochimica Acta, 49(16):2683–2689, 2004.

[9] DY Qu and H Shi. Studies of activated carbons used in double-layer capacitors. Journal Of Power Sources, 74(1):99–107, 1998.

[10] Dang Sheng Su and Robert Schloegl. Nanostructured Carbon and Carbon Nanocomposites for Electrochemical Energy Storage Applications. Chemsuschem, 3(2):136–168, 2010.

[11] Bin Xu, Feng Wu, Shi Chen, Cunzhong Zhang, Gaoping Cao, and Yusheng Yang. Activated carbon fiber cloths as electrodes for high performance electric double layer capacitors. Electrochimica Acta, 52(13):4595–4598, 2007.

[12] JJ Yoo, K Balakrishnan, J Huang, V Meunier, BG Sumpter, A Srivastava, M Conway, AL Mohana Reddy, J Yu, and R Vajtai. Ultrathin Planar Graphene Supercapacitors. Nano Letters, 11:1423–1427, 2011.

[13] Haijun Yu, Jihuai Wu, Leqing Fan, Kaiqing Xu, Xin Zhong, Youzhen Lin, and Jianming Lin. Improvement of the performance for quasi-solid-state supercapacitor by using PVA-KOH-KI polymer gel electrolyte. Electrochimica Acta, 56(20):6881–6886, 2011.

[14] K Zhang, L Zhang, and X Zhao. Graphene/polyaniline nanofiber composites as supercapacitor electrodes. Chemistry of Materials, 2010.

Chapter 2

Nanostructured All-Solid-State Supercapacitor Based on Li_2S-P_2S_5 Glass Ceramic Electrolyte

2.1 Abstract

While today's lithium-ion batteries offer acceptable energy storage capability, they lack the ability to be cycled repeatedly more than a couple thousand times. Electrochemical capacitors, i.e. Supercapacitors, are being developed whose lifetimes exceed one million cycles and power densities surpass those of batteries by several times. Here, we present an all-solid-state supercapacitor using a Li_2S-P_2S_5 glass-ceramic electrolyte as both separator and ion conductor. Three device architectures are examined including two with nanostructured electrodes which incorporate multi-walled carbon nanotubes (MWCNTs). Cyclic voltammograms and electrochemical impedance measurements demonstrate that these devices develop reversible double layer capacitance, and a maximum of 7.75 F/g is achieved in the device constructed by mechanically-mixing the nanostructured electrodes. Electrochemical impedance spectroscopy explains non-idealities observed when MWCNTs are incorporated in the electrode layers.[1]

2.2 Introduction and Motivation

Currently, two of the most viable electrical energy storage technologies based on performance and ease of implementation are secondary lithium batteries and electrochemical supercapacitors

---

[1] Adapted with permission from: Francisco, B. E., Jones, C. M. , Lee, S.-H., and Stoldt, C. R., *Applied Physics Letters* **2012**, 100, 103902. Copyright 2012 American Institute of Physics.

(SCs). As today's high performing lithium-ion batteries have lifetimes of <2000 cycles, supercapacitors with lifetimes exceeding 10^6 cycles are very attractive as modern energy storage solutions [20]. Present supercapacitors offer power densities greater than 4x those of batteries, and the gap is continually growing with new developments in energy storage materials [13]. With energy densities approaching those of commercial batteries, supercapacitors are poised to complement or even replace traditional batteries in many systems [13, 19].

Accordingly, research activity into various supercapacitor architectures has increased dramatically in recent years. Nearly all commercially available SCs utilize liquid electrolytes as the medium for ion transport [13, 6]. These devices are capable of impressive performance but are inherently dangerous due to the flammability of the electrolytes used and the potential for environmental harm resulting from accidental leakage. These points necessitate special safety precautions in device packaging, which add to the bulk of the devices. SCs with polymer-based electrolytes have been explored to replace liquid electrolytes [14], but the lower ionic conductivity of polymers limits potential power output. SCs utilizing polymers in the electrodes as pseudocapacitive materials can exhibit high levels of charge storage but face a consequence of performance degradation over time not seen with strictly-double-layer devices [5, 8, 18]

In this work, we demonstrate an all-solid-state supercapacitor based upon Li_2S-P_2S_5 glass-ceramic electrolyte, where lithium ions are used directly in a double-layer configuration to store charge. The Li_2S-P_2S_5 material system was chosen due to its high Li-ion conductivity (>1x10^{-3} S/cm) [4, 10, 9, 16]. Here, we evaluate three device configurations using the Li_2S-P_2S_5 glass-ceramic electrolyte. The most basic configuration (Device A) utilizes porous, conductive carbon paper as the electrodes and concurrently as the current collectors. In order to increase the interfacial contact between the solid-state electrolyte (SSE) and the electrodes beyond that of the basic device, multiwall carbon nanotubes (MWCNTs) were incorporated into a nanostructured electrode layer lying between the bulk SSE separator and carbon paper. Two general device architectures were studied that incorporate MWCNTs, one having nanostructured electrode layers fabricated by hand mixing (Device B), and the other fabricated by mechanical mixing (Device C). Figure 2.1 shows the main features of the device design.

2.3 Material Synthesis and Device Creation

The SSE was synthesized via planetary ball-milling from Li_2S and P_2S_5 [Alfa 99.9%, Aldrich 99%] in an 80-20 mol % ratio, and subsequently heat treated to form a semi-crystalline powder with particle sizes from about 1-5 μm [4, 16]. The resulting glass-ceramic material serves as the source of double-layer ions, the ion conductive medium, and the electrode separator in our devices. In devices B and C, the nanostructured electrode layer was prepared by mixing 5 wt% of as-received MWCNTs [Nanocyl NC7000] with SSE. Several nanotube loadings were evaluated and 5 wt% was determined to deliver the highest specific capacitance (Figure 2.2). Mixing of the MWCNTs and SSE was accomplished either with 15 minutes of mortar and pestle by hand (Device B) or via 15 minutes of planetary ball-milling using twenty stainless steel balls in a stainless steel jar spun at 450 rpm. (Device C). All handling and assembly was performed inside a dry, argon-filled glove box to minimize exposure of the SSE to atmospheric moisture. The bulk separator layer between the electrodes was composed of 100 mg of SSE, measuring approximately 450 μm in thickness. Device A was formed by pressing a piece of conductive carbon paper [Spectracarb 2050A-0850] onto each side of the SSE separator layer in a 13 mm diameter PEEK-lined die with titanium plungers at 3.8 ton/cm^2 for 15 minutes (Figure 2.3). Devices B and C included 15 mg of 5 wt%-MWCNT nanostructured composite electrode material dispersed in a thin layer across both faces of the SSE separator. This procedure yields 1.5 mg of MWCNTs in each device, which is the basis for our specific capacitance calculations. Carbon paper was added as a current collector behind each nanostructured electrode and an identical die and pressing procedure was used to complete fabrication in the case of Devices B and C.

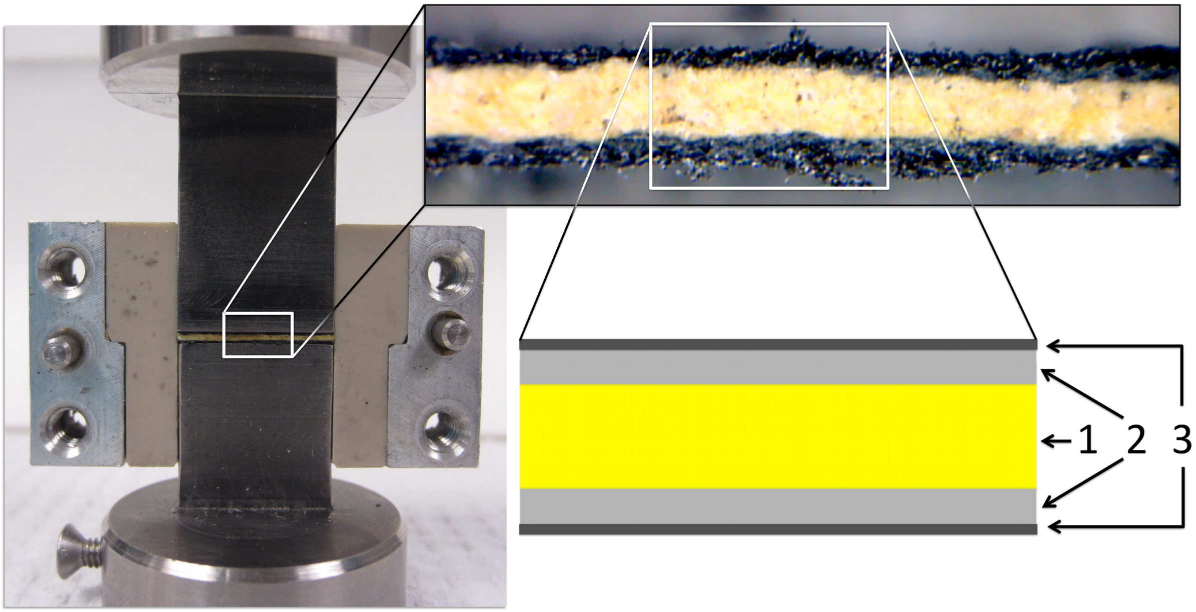

Figure 2.1: Optical image of the all-solid-state supercapacitor as fabricated within the press (left), and a close-up view of the device architecture with corresponding schematic indentifying the 1) SSE separator, 2) nanostructured electrodes (not present in Device A), and 3) carbon paper current collectors (right).

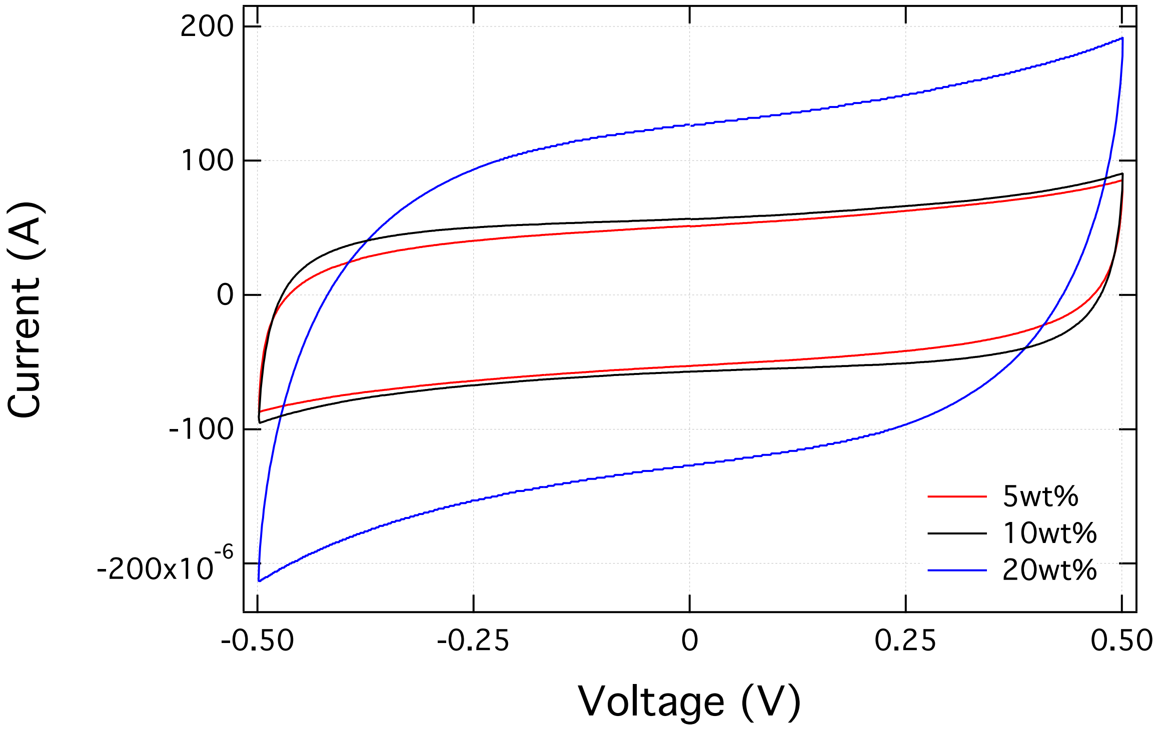

Figure 2.2: CV curves of MWCNT composite electrodes with 5, 10, and 20 wt% nanotube loading. In terms of specific capacitance, a 5 wt% composite delivers the best performance.

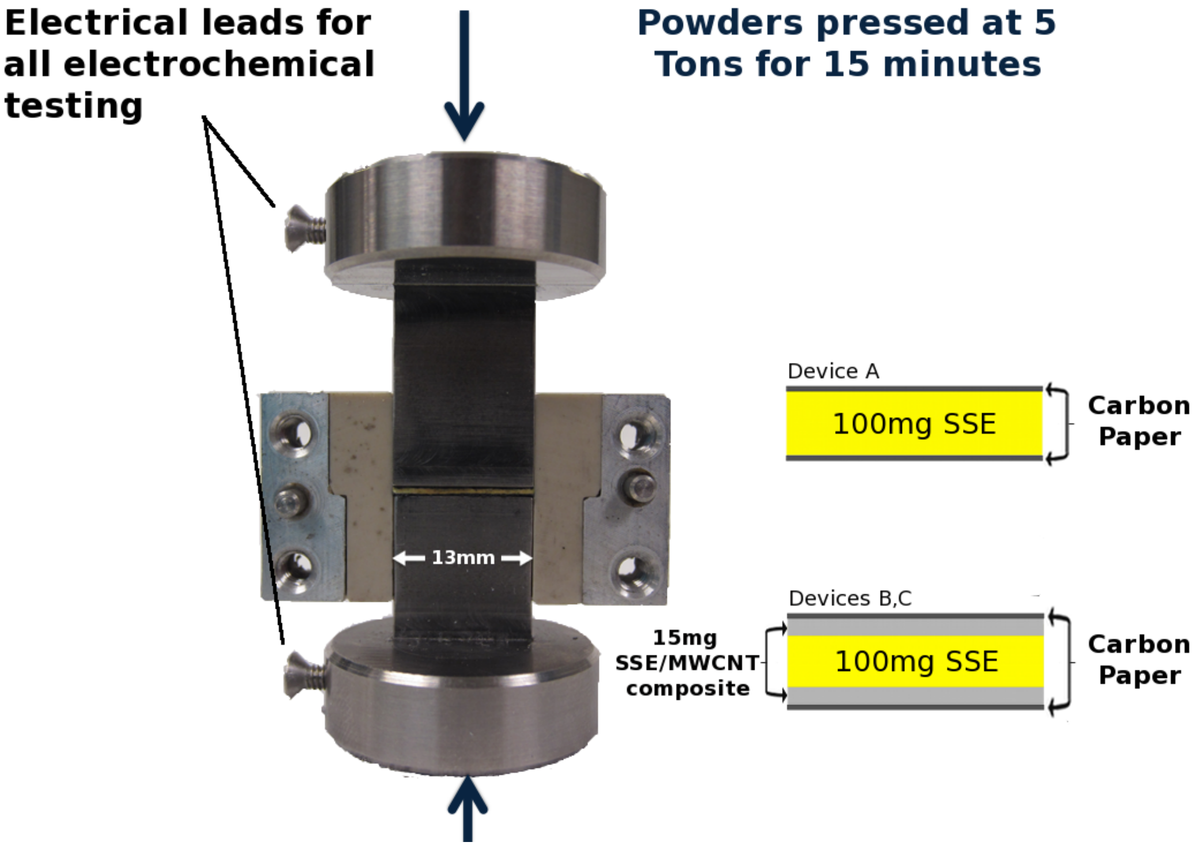

Figure 2.3: Further details of supercapacitor device manufacture.

2.4 Results and Discussion

2.4.1 Electrode Composite Characterization

Neither composite mixing method caused chemical changes to the components of the composite electrodes. Figure 2.4 shows Raman spectra (Jasco NRS-3100, 532 nm excitation) of the unmodified SSE, the hand-mixed composite, and the ball-milled composite. For reference, spectrum (a) shows the characteristic features of industrial grade MWCNTs, with the D band at 1348 cm^{-1}, attributable to amorphous carbon, having greater intensity than the graphitic G band at 1590 cm^{-1} [7]. Also observed are broad peaks at 1092 cm^{-1} and 556 cm^{-1} which in the peer-reviewed version of this work slipped through as being attributed to carbonaceous impurities [12], but in reality simply belong to the glass slide. Spectrum (b) shows unmodified SSE, the main feature of which is a peak at 420 cm^{-1} attributed to the primary $PS_4{}^{3-}$ structural unit of the SSE [15]. This peak is unchanged in the spectra of the composites ((c) and (d)), showing that the local bonding environments in the SSE have not changed during composite manufacture.

Of particular note in Figure 2.4 is the presence of MWCNT Raman peaks in the ball-milled composite (spectrum (d)) and their absence in the hand-mixed composite (spectrum (c)). This speaks to the degree of mixing in the composites. The unmodified SSE has a mustard yellow color. When hand-mixed with MWCNTs, the resulting composite develops a light gray color. While the light gray color indicates a low degree of mixing within the composite, the mixing is not sufficient to generate a significant response from the MWCNTs in a Raman spectrum. When MWCNTs are ball-milled with the SSE, the resulting composite develops a black appearance. In this latter case, the as-received MWCNT aggregates become broken up and better dispersed throughout the SSE such that their Raman response becomes significant. This Raman data lends qualitative support to the observation that ball-milling of the composite puts more carbon in contact with SSE.

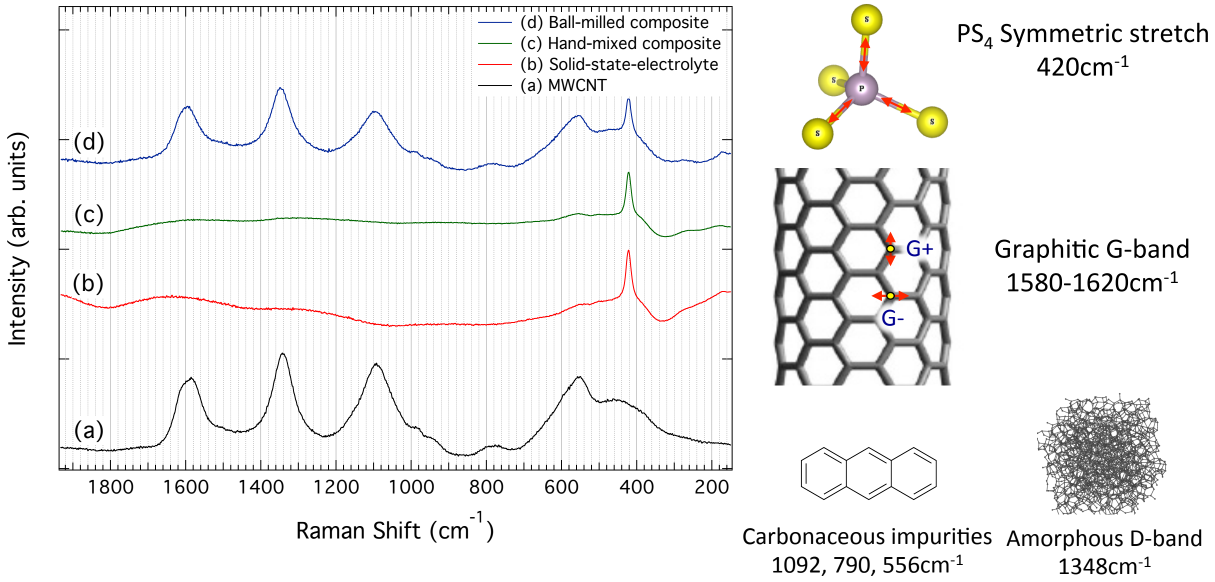

Figure 2.4: Raman spectra of (a) ball-milled SSE+MWCNT composite electrode, (b) hand-mixed SSE+MWCNT composite electrode, (c) Li_2S-P_2S_5 solid-state-electrolyte, and (d) MWCNTs. The vibrational signature of MWCNTs is observed in the ball-milled composite but not in the hand-mixed composite, indicating better carbon dispersion with ball-milling. Alongside this plot are models representing the specific vibrations observed.

2.4.2 Operational Principles and Electrochemical Characterization

2.4.2.1 Solid-State Supercapacitor Theory

Device operation is based on the mobility of Li^+ ions within the SSE structure under an applied electrical field. During charging, electrons are pumped from one carbon electrode into the other. This sets up a potential across the device, where Li^+ ions are then attracted to the carbon electrode with excess electrons. On this electrode, the ions migrate to the interface between the SSE and carbon to balance the charge due to the excess electrons. One can imagine a dense inner Helmholtz region close to the interface densely populated by interstitial Li^+ and a diffuse outer Helmholtz region further from the interface, analogous to double-layers in liquid electrolytes [19, 20]. At the opposing electrode, a deficiency of electrons in the carbon in contact with SSE will cause Li^+ to migrate away. This will leave a negative space charge in the SSE due to the lack of positive lithium ions that maintain electrical neutrality within the anionic framework of the glass-ceramic solid. The negative space charge balances the electron deficiency in the carbon. Thus, a double-layer is set up on each electrode due to the migration of cations within the electrolyte and supercapacitance is exhibited. A depiction of this charge storage mechanism is presented in Figure 2.5.

2.4.2.2 Cyclic Voltammetry and Galvanostatic Testing

Electrochemical characterization of the three aforementioned device architectures was carried out in an argon atmosphere, within the dies in which they were fabricated. Cyclic voltammetry (CV) and galvanostatic charge/discharge (CD) testing were used to characterize capacitive performance, with specific capacitance values (+/- 2.6%) extracted from the area under the CV curves. Electrochemical impedance spectroscopy (EIS) was used to approximate equivalent series resistance and to characterize the interface quality between the SSE and the carbon serving as electrodes in each device. CV tests were executed in the 5-100 mVs^{-1} sweep rate range for each device.

Figure 2.6a shows CV curves obtained from each device at a scan rate of 100 mV/s. Here, the

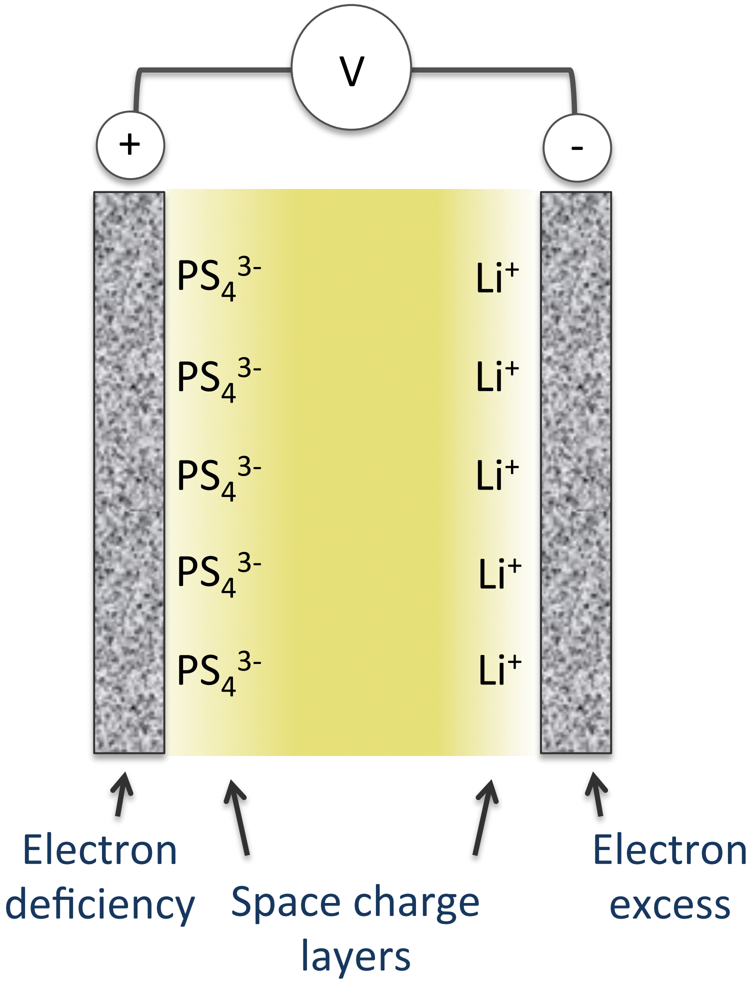

Figure 2.5: Visualization of double-layer charge storage in Li_2S-P_2S_5 solid electrolyte

incorporation of the nanostructured electrode layers within Devices B and C clearly demonstrate the effect that nanostructuring has on the capacitance of these solid-state devices. Device C produces a current three orders of magnitude larger than Device A at the same scan rate, corresponding to a proportionately larger capacitance. Device performance is summarized in Table 2.1. Observed is an increase in capacitance of more than an order of magnitude over Device A with the inclusion of MWCNTs in the nanostructured electrode layers by hand mixing (Device B), and a further increase of over an order of magnitude when the MWCNTs are mechanically mixed with the SSE to form the nanostructured electrode layers (Device C). Specific capacitance in terms of mass of MWCNTs, which is only appropriate to consider for Devices B and C, is highest in Device C with a value of 7.75 F/g.

Table 2.1: Capacitance of each device at various scan rates.

	Capacitance (mF)			Specific Capacitance(F/g)	
CV Scan Rate	Device A No CNTs	Device B Hand-Mixed CNT	Device C Ball-Milled CNT	Device B Hand-Mixed CNT	Device C Ball-Milled CNT
5 mV/s	0.0110	0.78	11.6	0.52	7.75
20 mV/s	0.0069	0.30	7.70	0.20	5.14
50 mV/s	0.0054	0.25	6.50	0.16	4.33
100 mV/s	0.0047	0.23	5.50	0.16	3.67

Figure 2.6b shows the CV series for Device C, for which the nanostructured electrode layers are prepared by mechanical mixing. The curves display a nearly ideal rectangular shape, indicating that double-layers are being efficiently set up within the device [3, 17]. CD curves shown in Figure 2.7 support this result with a nearly ideal sawtooth pattern at a current density of 67 mA/g.

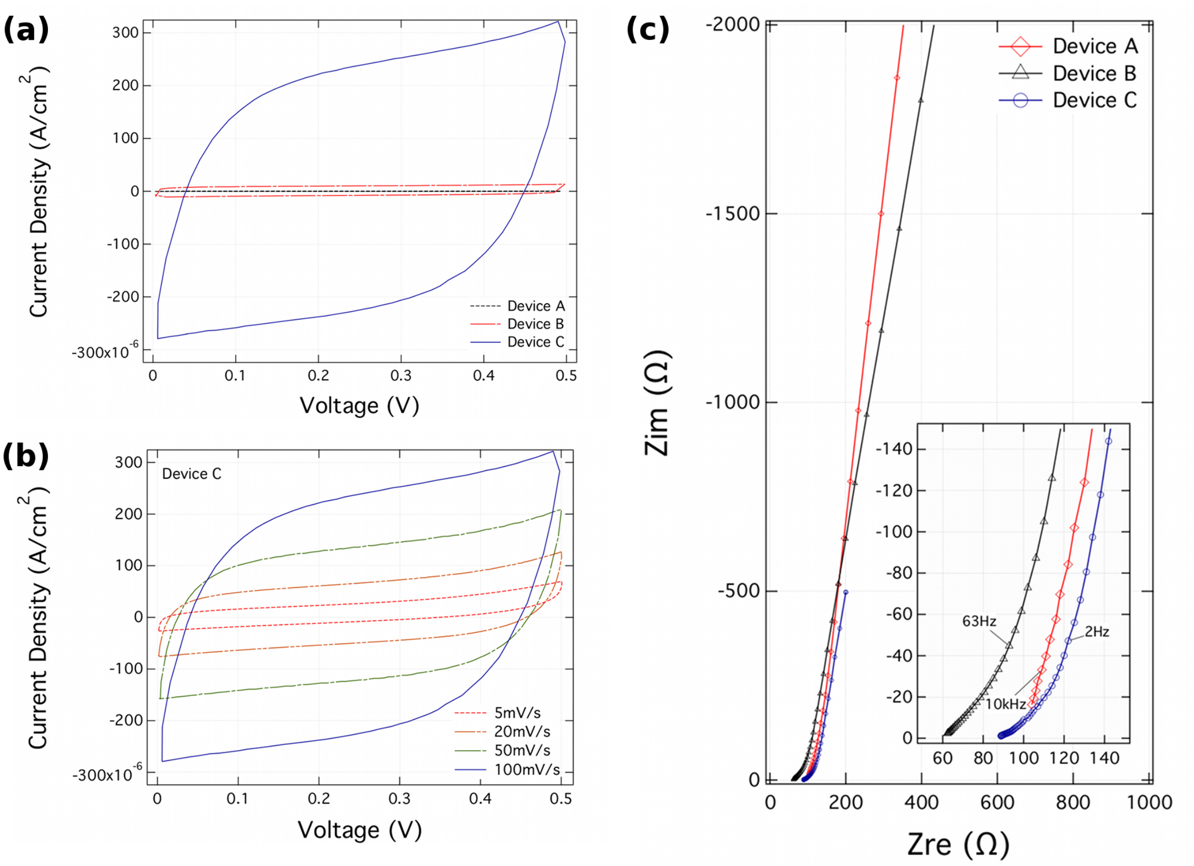

Figure 2.6: Electrochemical properties of the all-solid-state SCs. (a) CV curves from each device recorded at a scan rate of 100 mV/s. Device C produces a current over an order of magnitude greater than the other devices architectures. (b) CV curves for Device C in the scan rate range 5-100 mV/s. The nearly ideal rectangular shape indicates the reversible formation of double-layers at the electrodes, while the rounded corners are a consequence of high ESR. (c) Nyquist representation of impedance data from all three device architectures. A straight line slightly offset from vertical is observed in the full view, a feature typical of electrochemical capacitors. The inset highlights the high frequency response, attributed to varying degrees of CPE behavior.

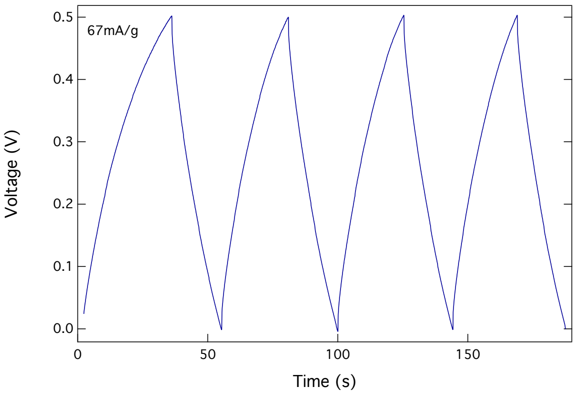

Figure 2.7: Galvanostatic testing results from Device C. The ideal lineshape would be a sawtooth pattern with straight lines; here, curvature is a result of internal cell electrical resistance (ESR).

2.4.2.3 Electrochemical Impedance Spectroscopy

Next, electrochemical impedance spectroscopy was used to help interpret how the inclusion of CNT composites impacts the quality of the electrode interfaces of the devices. Figure 2.6c shows the Nyquist plot of data taken for each device in the 100 mHz - 20 kHz frequency range with an AC amplitude of 10 mV (Solartron 1280c). From this plot, the devices display capacitive behavior, where the slight deviation from a straight vertical line indicates a degree of non-ideality associated with electrochemical capacitors [3, 6, 2, 11]. The inset of Figure 2.6c highlights the high frequency region of the Nyquist plot. In the high frequency range for Devices B and C, a divergence from the linear trend is observed. This is attributed to the presence of a distribution of capacitance values in the device, known as Constant Phase Element (CPE) behavior. By designating an impedance element a CPE, the equivalent circuit model can be simplified from dozens of capacitor-resistor elements with slightly different time constants to one CPE circuit element with a parameter, α, that characterizes the distribution of time constants, and therefore, capacitance values [1, 11]. The value of α can be extracted from the slope of the high frequency region of a plot of log(Zim) vs $\log(f)$. An α value of unity corresponds to an ideal single valued capacitor, and a decrease of α toward zero indicates an increasing distribution of capacitance values across the electrode interfaces. As Figure 2.8 shows, α values decrease overall from Device A to C. The relatively high α value of 0.85 for Device A can be explained by the regular woven pattern of the carbon paper in contact with the bulk SSE layer, which yields relatively uniform interfacial contact. The lower α values in Devices B and C can be interpreted as inhomogeneities in the nanostructured electrodes created by a poor distribution of MWCNTs. Alpha is lower in Device C than in Device B, likely due to the somewhat violent nature of the ball-mill mixing during nanocomposite fabrication which damages some portion of the MWCNTs leading to greater inhomogeneities within the electrodes. Fragmentation may increase ESR in these devices, leading to a deviation from ideal performance and fully rectangular CV curves. However, this fragmentation increases the interfacial contact between carbon and SSE in the electrodes, as reflected in the increased capacitance. This analysis indicates that while incorporating MWCNTs by hand or mechanical mixing drastically increases the specific capacitance, electrode inhomogeneities exist which, if reduced, can further enhance device performance.

2.5 Conclusions

Although the measured specific capacitance in the all solid-state devices detailed here are lower than their liquid electrolyte counterparts, there exists an opportunity to further increase their performance through optimization of the nanostructured electrodes and interfaces. In liquid electrolyte based SCs, achieving high areal contact with electrodes is a relatively simple matter of implementing porous electrode structures. In the solid state, the micron-sized electrolyte particles used in the devices presented here may be a limiting factor in device performance, owing to the limited contact area with the much smaller MWCNTs. If SSE particle size is reduced prior to device integration, it will be possible to put more MWCNTs in contact with SSE, thus increasing specific capacitance and lowering device ESR.

In summary, we have demonstrated a nanostructured Li^+ ion based SC that delivers nearly 10 F/g with the introduction of MWCNTs to the electrodes. By incorporating a SSE as both the electrode separator layer and ionic conduction medium, many of the safety concerns associated with modern liquid electrolyte SCs are addressed while simplifying the device architecture. Through electrochemical testing, the all solid-state device performance is shown to approach that of an ideal capacitor. Impedance analysis reveals that while introducing MWCNTs greatly increases device capacitance, large inhomogeneities are introduced into the nanostructured electrodes that contribute to increased ESR and non-ideal performance. With further engineering of electrodes, it should be possible to increase specific capacitance and reduce ESR to achieve performance approaching or exceeding that of liquid electrolyte based SCs.

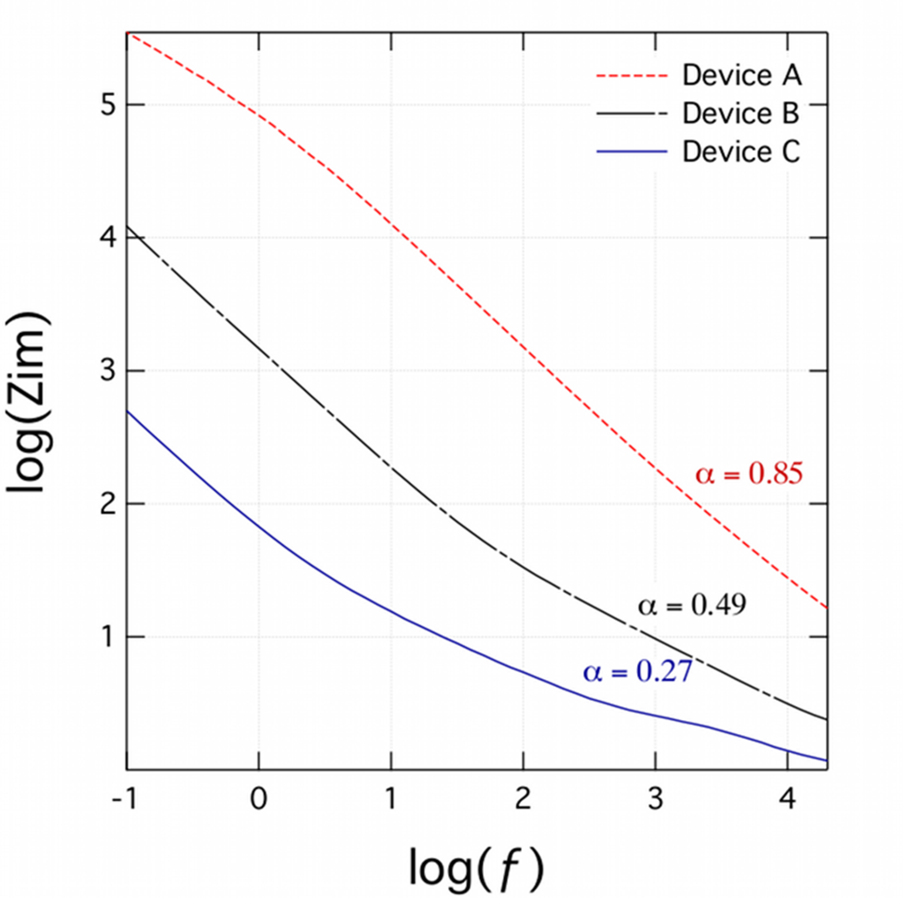

Figure 2.8: Constant Phase Element behavior. Alpha is observed to decrease from Device A → B → C, indicating greater CPE behavior. This is attributed to an increasing degree of inhomogeneity in the electrodes due to the incorporation of MWCNTs.

References

[1] Evgenij Barsoukov and James Ross Macdonald. Impedance Spectroscopy. Theory, Experiment, and Applications. John Wiley & Sons, New Jersey, 2 edition, March 2005.

[2] Bong Gill Choi, Jinkee Hong, Won Hi Hong, Paula T Hammond, and HoSeok Park. Facilitated Ion Transport in All-Solid-State Flexible Supercapacitors. ACS nano, 5(9):7205–7213, 2011.

[3] B E Conway. Electrochemical Supercapacitors. Scientific Fundamentals and Technological Applications. Springer, April 1999.

[4] Akitoshi Hayashi, S Hama, F Mizuno, K Tadanaga, T Minami, and Masahiro Tatsumisago. Characterization of Li2S-P2S5 glass-ceramics as a solid electrolyte for lithium secondary batteries. Solid State Ionics, 175(1-4):683–686, 2004.

[5] M M Khandpekar, R K Kushwaha, and S P Pati. Design, fabrication, and evaluation of a 5 F-5 V prototype of solid-state PANI based supercapacitor. Solid-State Electronics, 62(1):156–160, 2011.

[6] R Kotz, M Hahn, and R Gallay. Temperature behavior and impedance fundamentals of supercapacitors. Journal Of Power Sources, 154(2):550–555, 2006.

[7] John H Lehman, Mauricio Terrones, Elisabeth Mansfield, Katherine E Hurst, and Vincent Meunier. Evaluating the characteristics of multiwall carbon nanotubes. Carbon, 49(8):2581–2602, July 2011.

[8] Qiang Liu, Munir H Nayfeh, and Siu-Tung Yau. Brushed-on flexible supercapacitor sheets using a nanocomposite of polyaniline and carbon nanotubes. Journal Of Power Sources, 195(21):7480–7483, November 2010.

[9] Keiichi Minami, Fuminori Mizuno, Akitoshi Hayashi, and Masahiro Tatsumisago. Lithium ion conductivity of the Li2S-P2S5 glass-based electrolytes prepared by the melt quenching method. Solid State Ionics, 178(11-12):837–841, 2007.

[10] F Mizuno, Akitoshi Hayashi, K Tadanaga, and Masahiro Tatsumisago. High lithium ion conducting glass-ceramics in the system Li2S-P2S5. Solid State Ionics, 177(26-32):2721–2725, 2006.

[11] Mark E Orazem and Bernard Tribollet. Electrochemical Impedance Spectroscopy. John Wiley & Sons, October 2011.

[12] Hideaki Shinohara, Yoshihiro Yamakita, and Koichi Ohno. Raman spectra of polycyclic aromatic hydrocarbons. Comparison of calculated Raman intensity distributions with observed spectra for naphthalene, anthracene, pyrene, and perylene. Journal Of Molecular Structure, 442(1):221–234, 1998.

[13] Riccardo Signorelli, Daniel C Ku, John G Kassakian, and Joel E Schindall. Electrochemical Double-Layer Capacitors Using Carbon Nanotube Electrode Structures. Proceedings of the IEEE, 97(11):1837–1847, 2009.

[14] Graeme A Snook, Pon Kao, and Adam S Best. Conducting-polymer-based supercapacitor devices and electrodes. Journal Of Power Sources, 196(1):1–12, 2011.

[15] M Tachez, JP Malugani, R Mercier, and G Rebert. Ionic-conductivity of and phase-transition in lithium thiophosphate Li3PS4. Solid State Ionics, 14(3):181–185, 1984.

[16] James Trevey, Jum Suk Jang, Yoon Seok Jung, Conrad R Stoldt, and Se-Hee Lee. Glass-ceramic Li2S-P2S5 electrolytes prepared by a single step ball billing process and their application for all-solid-state lithium-ion batteries. Electrochemistry Communications, 11(9):1830–1833, 2009.

[17] JJ Yoo, K Balakrishnan, J Huang, V Meunier, BG Sumpter, A Srivastava, M Conway, AL Mohana Reddy, J Yu, and R Vajtai. Ultrathin Planar Graphene Supercapacitors. Nano Letters, 11:1423–1427, 2011.

[18] Haijun Yu, Jihuai Wu, Leqing Fan, Kaiqing Xu, Xin Zhong, Youzhen Lin, and Jianming Lin. Improvement of the performance for quasi-solid-state supercapacitor by using PVA-KOH-KI polymer gel electrolyte. Electrochimica Acta, 56(20):6881–6886, 2011.

[19] LL Zhang and XS Zhao. Carbon-based materials as supercapacitor electrodes. Chemical Society Reviews, 38(9):2520–2531, 2009.

[20] Xin Zhao, Beatriz Mendoza Sanchez, Peter J Dobson, and Patrick S Grant. The role of nanomaterials in redox-based supercapacitors for next generation energy storage devices. Nanoscale, 3(3):839–855, 2011.

Chapter 3

Phosphate Lithium-Ion Electrolytes

3.1 From Sulfides to Phosphates

In order to build on our work on solid-state supercapacitors in Chapter 2, we needed a better understanding of the mobility of lithium-ions within solid electrolytes. Our physical models of supercapacitance necessitate that ions move freely within the solid-state structure. But how mobile are they really?

To answer this question we needed to design a study that would allow correlations to be drawn between the structure of a solid-state ion conductor and its observed conduction properties. Unfortunately, the Li_2S-P_2S_5 system we used in our supercapacitor development has severe limitations on analysis due to degredation on contact with atmospheric oxygen and moisture [7]. Therefore, to continue to grow our understanding of ion mobility in the solid state, we needed to adopt an air-stable material system. Additionally, a crystalline system was desirable from the standpoint of analyzing structural details. We chose to work with a phosphate-based material system due to advantages in synthesis and stability, and there existing a well-characterized crystal structure. Work on the system we selected began at MIT some 39 years prior to the present work, and it remains a system of high value to the solid-state battery community.

3.2 Super-Ionic Conductors

A breakthrough in solid electrolytes was made by H. Y.-P. Hong in 1976 with the discovery of $Na_{(1+x)}Zr_2Si_xP_{(3\text{-}x)}O_{12}$, a sodium-ion conducting ceramic [5]. This material had a unique crystal structure composed of an anionic metal-phosphate backbone and open three dimensional channels through which alkali ions travel. Based on the superb conduction properties of this framework-type structure, this material was called a Sodium-ion Super Ionic Conductor (NASICON). Any materials with analogous structures were thereafter coined NASICON-type materials.

The general formula for NASICON-type electrolytes may be written as $AM_2X_3O_{12}$, where A is an alkali metal, M can be any number of transition or main group metals, and X is typically phosphorus or silicon [2, 12, 1]. In the NASICON-type structure, an anionic framework of MO_6 octahedra linked to XO_4 tetrahedra leaves large voids that are filled with the charge compensating alkali cations. The voids are interconnected and form three-dimensional conduction channels through which the alkali ions may hop, leading to measured ionic conductivities on the order of liquid electrolytes. A representation of this structure is shown in Figure 3.1, with the 3D conduction channels traced as a visual guide.

A large number of the possible combinations of chemistries that adopt the NASICON framework structure have been synthesized and evaluated as ionic conductors [8, 9, 6]. Those of current interest serve as lithium-ion conductors with the intention of being developed into a separator material for solid-state lithium batteries.

When the focus turned to Li-ion batteries, lithium-conducting analogues saw a rise in development. Lithium titanium phosphate ($LiTi_2(PO_4)_3$) surfaced as a NASICON-type lithium-ion conductor [10], although it was not chemically stable against lithium metal due to the ease of $Ti^{4+/3+}$ reduction. Lithium germanium phosphate ($LiGe_2(PO_4)_3$) was a better candidate for a lithium battery electrolyte, but with a conductivity $<1x10^{-6}$ S/cm, it wasnt practically useful [4]. It was here that work began in tailoring the chemistry of these framework-type conductors in an attempt to increase conductivity.

3.3 Conductivity

In the case of ion-conducting solids such as the NASICON-type materials, ionic conductivity is governed by the relation $\sigma = q \; n \; \mu$, where σ is the conductivity, q is the charge moved by each

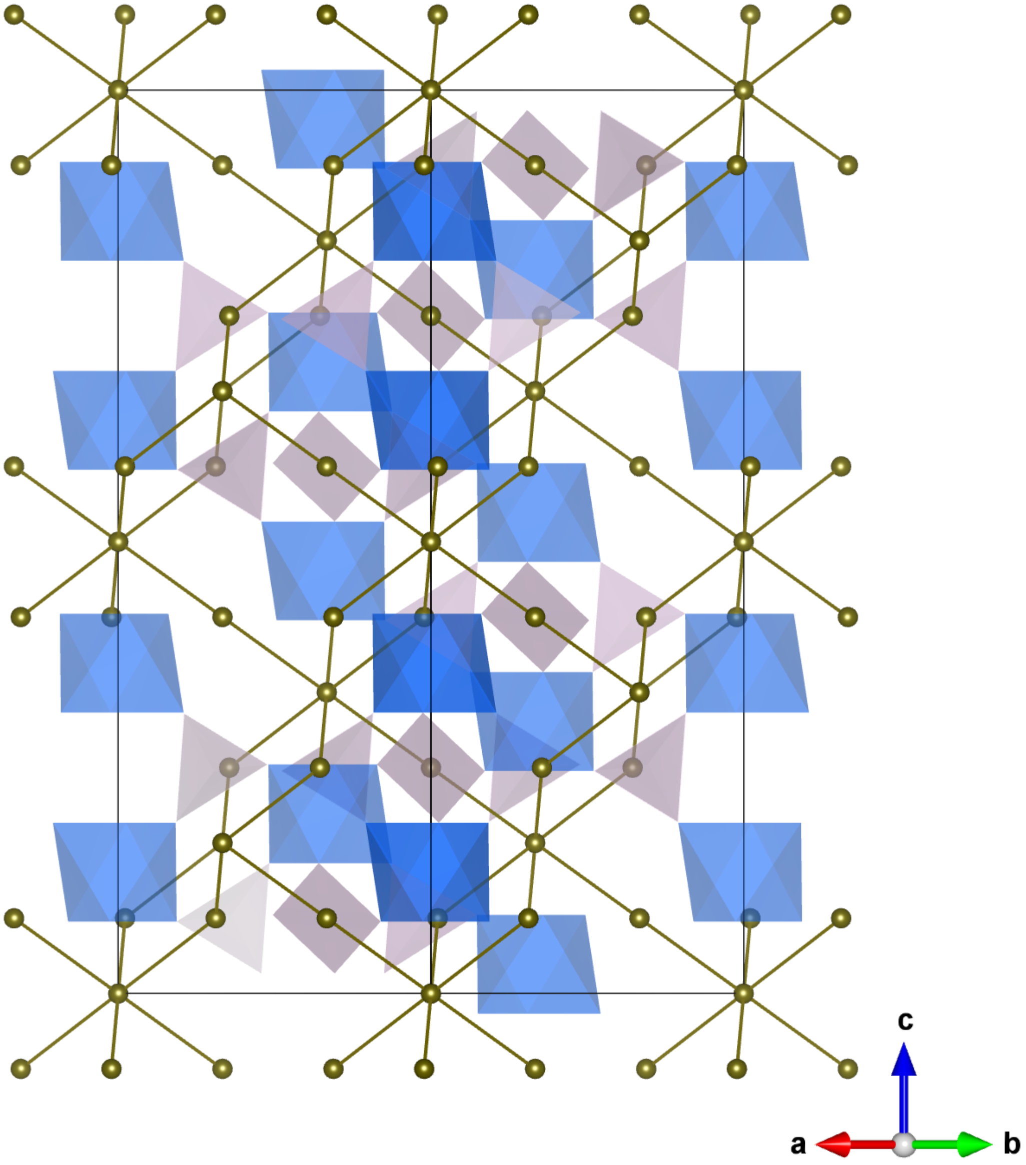

Figure 3.1: The framework of the NASICON structure consists of MO_6 octahedra (blue) linked to PO_4 tetrahedra (purple) through corner-shared oxygen atoms. Lithium atoms (gold) reside in vacancies in this framework. In the representation shown here, every lithium site is shown as being occupied. In real conductors, vacancies are needed for ion hopping, and some of the sites shown here would have only partial occupancy. The conduction channels extend in three dimensions through the framework, leading to high conductivity when this material is processed in polycrystalline form.

carrier, n is the charge carrier density, and μ is the mobility of each carrier [3]. When considering lithium ions as the only charge carriers, two strategies for enhancing conductivity become apparent: increasing the number of lithium ions per unit cell or increasing the mobility of these ions.

In order to increase the conductivity of $LiGe_2(PO_4)_3$, Ge^{4+} can be partially substituted by Al^{3+} following the formula $Li_{(1+x)}Al_xGe_{(2\text{-}x)}(PO_4)_3$ [4]. Since the aluminum ion has approximately the same radius as the germanium ion, the substitution is easily accomplished. The boost in conductivity in this material comes from the extra charge-compensating lithium ions incorporated into the structure with the aluminum.

The alternative strategy to increasing conductivity is to increase ion mobility. In a qualitative sense it can be understood that if the conduction channels are widened, it may be easier for a hopping lithium ion to move through the crystal, leading to an enhanced mobility. Indeed, the activation energy for lithium conduction has been observed to decrease in the series Ge(0.53 Å) → Sn(0.69 Å) → Hf(0.71 Å) for $NaM_2(PO_4)_3$ [11]. Following this line of thought, many researchers have attempted to substitute larger cations for a fraction of the host cations with the effect of increasing the unit cell volume of the material, and thereby opening the conduction pathways.

While substitution with larger cations has been shown to increase unit cell volume, it does not always lead to enhancements in ionic conductivity. If the dopant cation is significantly larger than the host it replaces, local distortions may develop which actually choke conduction pathways and restrict ion conduction.

3.4 Study of the NASICON Electrolyte System

In Chapter 4 we present a study of the $Li[Al,Ge,Sn](PO_4)_3$ system to elucidate the effects on structure and ion mobility when a large size disparity exists between the cations in the structural framework. We find that in the literature, the effects of this size disparity are often ignored. However, as we demonstrate, deleterious consequences can result when size disparity imparts lattice strain.

One unanticipated result of the work in Chapter 4 invlolved insights into the entropy of ion motion. In our data sets we observed pieces of what seemed to be a compositional trend in this mostly unexplored thermodynamic parameter. In this work, we presented a theory on what this entropy value may represent physically. To date, there is no published theory that goes beyond the vague suggestion of this being a configurational entropy. To this suggestion we can say: Of course. The most common interpretation of entropy involves possible configurations of the system, but what might this represent physically? To extend our knowledge about ion-dynamics in solid-state electrolytes, we designed a study using the $\mathrm{Li_{(1+x)}Al_xGe_{(2\text{-}x)}(PO_4)_3}$ family of materials with the goal of rationalizing the source and significance of the entropy of ion motion. The details of this study are presented in Chapter 5, and, although certainly biased to enjoy our own work, we find the results incredibly interesting.

References

[1] James Alamo and Rustum Roy. Crystal chemistry of the $NaZr_2(PO_4)_3$, NZP or CTP, structure family. Journal of Materials Science, 21(2):444–450, February 1986.

[2] N Anantharamulu, K Koteswara Rao, G Rambabu, B Vijaya Kumar, Velchuri Radha, and M Vithal. A wide-ranging review on Nasicon type materials. Journal of Materials Science, 46(9):2821–2837, February 2011.

[3] Peter G Bruce. Solid State Electrochemistry. Cambridge University Press, New York, 1 edition, June 1997.

[4] M Cretin and P Fabry. Comparative study of lithium ion conductors in the system $Li_{1+x}Al_xA_{2x}{}^{IV}$ $(PO_4)_3$ with A^{IV}=Ti or Ge and 0x07 for use as Li^+ sensitive membranes. Journal Of The European Ceramic Society, 19(16):2931–2940, December 1999.

[5] HY-P Hong. Crystal structures and crystal chemistry in the system $Na_{1+x}Zr_2Si_xP_{3x}O_{12}$. Materials Research Bulletin, 11(2):173–182, 1976.

[6] Ana Martinez-Juarez, Carlos Pecharromán, Juan E Iglesias, and José M Rojo. Relationship between Activation Energy and Bottleneck Size for Li^+ Ion Conduction in NASICON Materials of Composition LiMM'$(PO_4)_3$; M, M'= Ge, Ti, Sn, Hf. The Journal of Physical Chemistry B, 102(2):372–375, 1998.

[7] Hiromasa Muramatsu, Akitoshi Hayashi, Takamasa Ohtomo, Sigenori Hama, and Masahiro Tatsumisago. Structural change of Li2S-P2S5 sulfide solid electrolytes in the atmosphere. Solid State Ionics, 182(1):116–119, 2011.

[8] Yuria Saito, Kazuaki Ado, Takashi Asai, Hiroyuki Kageyama, and Osamu Nakamura. Ionic conductivity of NASICON-type conductors Na1. 5M0. 5Zr1. 5 (PO4) 3 (M: Al3+, Ga3+, Cr3+, Sc3+, Fe3+, In3+, Yb3+, Y3+). Solid State Ionics, 58(3-4):327–331, 1992.

[9] P Tarte, A Rulmont, and C Merckaert-Ansay. Vibrational spectrum of nasicon-like, rhombohedral orthophosphates $M^IM_2{}^{IV}(PO_4)_3$. Spectrochimica Acta Part A: Molecular Spectroscopy, 42(9):1009–1016, 1986.

[10] B WANG, M Greenblatt, S Wang, and S J Hwu. Ionic conductivity of lithium titanium phosphate LithiumTi2 (PO4)3(0.2 .ltoreq. x .ltoreq. 1.72) with NASICON-related structures. Chemistry of Materials, 5(1):23–26, January 1993.

[11] Jean-Marc Winand, André Rulmont, and Pierre Tarte. Nouvelles solutions solides $L^{I}(M^{IV})_{2x}(N^{IV})_{x}(PO_4)_3$ ($\underline{L}$ = Li,Na $\underline{M,N}$ = Ge,Sn,Ti,Zr,Hf) Synthèse et étude par diffraction x et conductivité ionique. Journal of Solid State Chemistry, 93(2):341–349, August 1991.

[12] A B Yaroslavtsev and I A Stenina. Complex phosphates with the NASICON structure (M x A2(PO4)3). Russian Journal of Inorganic Chemistry, 51(S1):S97–S116, January 2006.

Chapter 4

Lithium-Ion Trapping from Local Structural Distortions in Sodium Super Ionic Conductor (NASICON) Electrolytes

4.1 Abstract

Herein we report a study on the structural and thermodynamic effects that cation size disparity may have in NASICON-type solid solutions. A sol-gel procedure was used to synthesize two new NASICON-type lithium-ion conductors with nominal compositions $\mathrm{LiGe}_{2-y}\mathrm{Sn}_y(\mathrm{PO}_4)_3$ and $\mathrm{Li}_{1+x}\mathrm{Al}_x\mathrm{Ge}_{2-y-\frac{1}{2}x}\mathrm{Sn}_{y-\frac{1}{2}x}(\mathrm{PO}_4)_3$. The effect of tin substitution on structure and lithium-ion conductivity was studied with powder x-ray diffraction, Raman spectroscopy, and dielectric spectroscopy. It is found that although increased unit cell dimensions derived from x-ray data suggest that tin incorporation should open the conduction bottleneck regions and improve conductivity, a decrease in conductivity is observed. Analysis of the electrical data shows that the conduction activation energy is comprised of contributions from carrier motion and generation, the latter accounting for up to 20% of the total activation energy. This result, currently unreported for NASICON-type materials, is correlated with local structural distortions observed in Raman spectra. It is deduced that the bottleneck regions suffer distortions due to the large ionic radius disparity among cationic constituents, which results in the trapping of charge carriers. Data estimated for the entropy of motion is also presented and discussed considering the most probable thermodynamic equilibrium states.[1]

---

[1] Reprinted with permission from: Francisco, B. E., M'Peko, J.-C., and Stoldt, C. R., *Chemistry of Materials* **2014**, 26(16), 4741-4749. Copyright 2014 American Chemical Society.

4.2 Introduction and Motivation

With the ever-increasing storage capacity demands on rechargeable lithium-ion batteries, research efforts over the last decade have focused on the development of emerging technologies having the potential for improved performance. Lithium-air batteries are one promising candidate but are currently limited by the availability of high-conducting separator materials. First discovered in 1976 [22], materials of the Sodium Super Ionic Conductor (NASICON) family are receiving renewed attention as the mechanically robust, air and water stable separator that is required for lithium-air batteries [29, 33, 16, 39].

In the case of ion-conducting solids such as the NASICON-type materials, conductivity (σ) is governed by the relation $\sigma = c\mu q$, where c is the density of charge carriers, μ is the mobility of the charge carriers, and q is the charge carried by each carrier. When considering lithium ions (Li^+) as the only charge carriers, two primary strategies for enhancing conductivity exist: increasing the number of lithium ions per unit cell or increasing the mobility of the lithium ions. As a key example, the room temperature conductivity of lithium germanium phosphate can be increased by three orders of magnitude by adopting a heterovalent substitution scheme following [38, 24]: $LiGe_2(PO_4)_3 \rightarrow Li_{1+x}Al_xGe_{2-x}(PO_4)_3$. Since the Ge^{4+} (0.53 Å) and Al^{3+} (0.535 Å) ions have nearly the same radius, and there are many unfilled sites available for the additional lithium ions in the structure, the substitution is easily accomplished.

In NASICON crystals of general formula $LiM_2(PO_4)_3$, columns of MO_6 octahedra are linked by PO_4 tetrahedra [22]. Lithium ions reside in two possible sites, the M1 site being 6-fold coordinated and located directly between two stacked MO_6 units, and/or the M2 site which lies in an 8-fold coordinated location between two columns of MO_6 units. During long-range motion, the ions hop between these two sites as they traverse the crystal. Lithium-ion mobility is controlled by the most restrictive point in the conduction pathway. In NASICON-type structures, the largest restriction to lithium-ion motion results from a window between sites M1 and M2 made of three oxygen atoms bound to neighboring M cations. Figure 4.1 shows a representation of a typical NASICON crystal with the 3D conduction pathways drawn. A close-up of the so-called bottleneck region at the intersection of three pathways is depicted in the upper left. In the past, a link between the size of this bottleneck and the size of the M cation has been established [28], but there remains some ambiguity as to whether this causal relationship holds when M is a main group element or when multiple substitutions are enacted.

In this study, we examine the effects of partial Sn^{4+} for Ge^{4+} substitution on the structure and lithium-ion conductivity of NASICON-type materials. Since germanium and tin reside in the same group on the periodic table, their similar electronic structures and tendency to adopt 4+ oxidation states make it possible to focus on the effects that ion size difference has on crystal structure and ion mobility. It is hypothesized that the inclusion of the larger Sn^{4+} (0.69 Å) will open the bottleneck points and promote enhanced lithium-ion mobility. Herein, we report on two new tin-bearing NASICON crystals with nominal compositions $LiGe_{2-y}Sn_y(PO_4)_3$ and $Li_{1+x}Al_xGe_{2-y-\frac{1}{2}x}Sn_{y-\frac{1}{2}x}(PO_4)_3$ and provide a comparison to the analogues without tin. Here, tin-for-germanium substitution was fixed at 50 mol% (y = 1) for ease of comparison. The $M^{4+} \rightarrow Al^{3+} + Li^{+}$ substitution rate was chosen to match the composition of LAGP demonstrated to have the highest conductivity in the series $Li_{1+x}Al_xGe_{2-x}(PO_4)_3$, namely x = 0.5 [24, 7]. We use powder x-ray diffraction to study lattice constants and long-range order, Raman spectroscopy to study the local order of PO_4 groups in the anionic backbone of the structure, and dielectric (electrochemical impedance plus electric modulus) spectroscopy to elucidate the ion hopping dynamics in the bulk of these materials. We use insights gained from structural characterizations to propose explanations for the observed thermodynamics associated with lithium-ion motion in the crystal.

4.3 Experimental Methods

4.3.1 Synthesis of Powders

A Pechini-type sol-gel process using citric acid and ethylene glycol was used to synthesize all of the materials evaluated in this study. All solutions were prepared from as-received precursors in

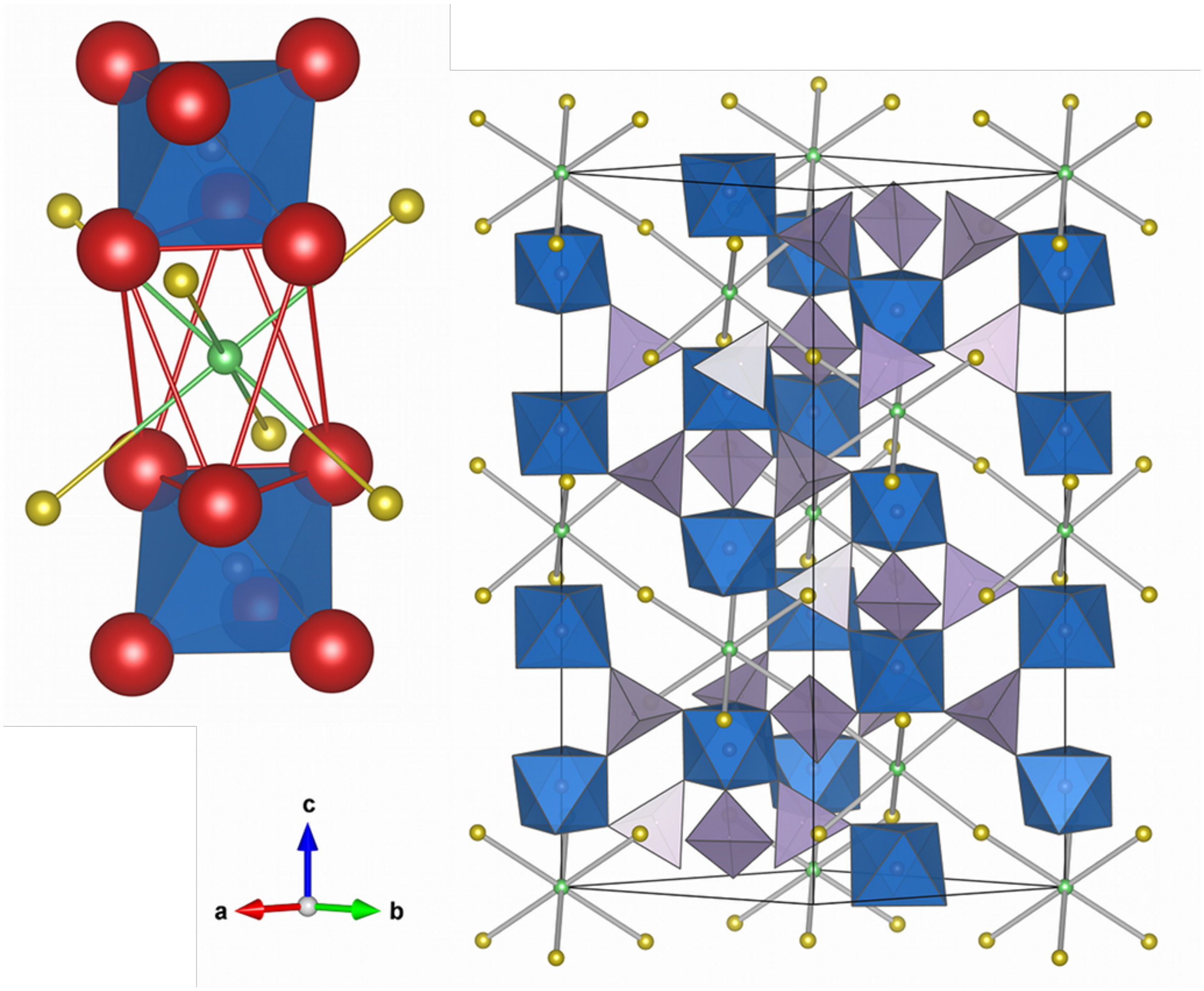

Figure 4.1: Representations of a typical NASICON structure. Blue octahedra are MO_6 units, purple tetrahedra are PO_4 units, green spheres are M1 sites, and yellow spheres are M2 sites. Pathways for Li^+ motion are drawn between M1 and M2 sites. The structure in the upper-left shows a close-up view of the conduction bottleneck region with the constrictive window between oxygen atoms traced in red.

proper stoichiometric ratios. Moisture sensitive precursors were stored in a dry argon glovebox prior to use. Alcoholic and aqueous solutions of precursors were prepared separately and then mixed. The [citric acid + ethylene glycol : metal ion] ratio was fixed at [4:1]. To prepare the alcoholic solutions, $Ge(OC_2H_5)_4$ (Gelest >95%), $Sn(OC_3H_7)_4C_3H_7OH$ (Gelest >95%), and an appropriate amount of citric acid (Alfa 99.5%+) were dissolved in isopropanol under vigorous stirring at 80°C for 1 hr. At the same time, aqueous solutions of $LiNO_3$ (Alfa 99%), $Al(NO_3)_3{\cdot}9H_2O$ (Alfa 98-102%), $NH_4H_2PO_4$ (Sigma ≥99.99%), and an appropriate amount of citric acid dissolved in deionized water were prepared by stirring at 80°C for 1 hr. Next, the aqueous solution was slowly added to the alcoholic solution under vigorous stirring. Ethylene glycol (Mallinckrodt Chemicals 99%) was then added to promote polymerization of the complex upon drying, and the mixture was held at 80°C under stirring for 6 hrs. Finally, the sol was transferred to an oven and dried at 120°C overnight. The resulting dry gel was ground with mortar and pestle and treated for 8 hrs at 500°C to decompose the organics, which left a fine powder coated in carbon residue. This powder was again ground with mortar and pestle and treated an additional 8 hrs at 900°C to burn off carbon residue and complete the reaction to form fine particles of the NASICON-type materials. The final treatment temperature of 900°C was chosen based on previously reported phase purity data for the $LiGe_2(PO_4)_3$ system [18, 26, 38], and on our own observations which show that significant GeO_2 generation, likely driven by lithium loss, occurs above this temperature. For the remainder of this article, we will refer to materials by the following acronyms: LGP = $LiGe_2(PO_4)_3$, LAGP = $Li_{1.5}Al_{0.5}Ge_{1.5}(PO_4)_3$, LGSP = $LiGeSn(PO_4)_3$, and LAGSP = $Li_{1.5}Al_{0.5}Ge_{0.75}Sn_{0.75}(PO_4)_3$.

4.3.2 Powder X-ray Diffraction (XRD)

X-ray diffraction patterns of powdered samples were collected with CuK_α radiation (λ = 1.5418Å) in the range 10-90° 2θ using a Phillips XPert MPD operated at 45 kV and 40 mA. An Xcelerator 1D detector with a step size of 0.008° and collection time of 5 s per step were employed. Sample displacement was corrected by the use of a pure Corundum internal standard. Rietveld-type profile fits of the data were carried out using the General Structure Analysis System (GSAS) software to extract lattice parameters using $LiGe_2(PO_4)_3$ JCPDS #80-1922 and results from Ref [25] as structural models.

4.3.3 Raman Spectroscopy

Raman spectra were recorded in the range 150-1300 cm^{-1} using a JASCO NRS-3100 system equipped with a 532 nm laser at a power level of 22 mW. Raman shift was calibrated using a silicon standard and accuracy was estimated to be ±2.5 cm^{-1}

4.3.4 Electrochemical Impedance Spectroscopy

Samples for EIS measurements and subsequent analysis were prepared by the following procedure. First, powders were dried overnight at 120°C to remove adsorbed water. The dry powder was then deagglomerated and dispersed by gentle roller-milling overnight with zirconia media in a 50:50 mixture of MEK:ethanol with 2.5 wt% Menhaden fish oil (Tape Casting Warehouse). Next, 3 wt% poly(vinyl butryal) (Tape Casting Warehouse) was added as a binder and the mixture was again milled overnight. The resulting slurry was dried back to powder, which then had well dispersed particles and a homogenous incorporation of binder. Cylindrical pellets approximately 12 mm in diameter and 1 mm in thickness were uniaxially pressed from this powder at 377 MPa in a stainless steel die. These "green" pellets were subjected to binder-burnout and a final sintering of 12 hrs at 900°C on platinum foil in air. Final density and porosity was measured using the Archimedes method with deionized water as the buoyant medium. From the theoretical densities estimated from refined x-ray diffraction patterns, porosity in these samples ranged from about 15% to 20% after sintering. The consequences of this residual porosity will be discussed later, however it is worth stressing here that there was no impact on the comparative analysis carried out in this study.

To enable electrical measurements, a Technics Hummer V Sputter Coater was used to deposit 500 nm of pure gold onto each face of the pelletized samples. Pellets were then sealed in a custom apparatus that allowed tests to be conducted in flowing dry argon, thereby excluding the effects of moisture.

Impedance ($Z^* = Z'\ \ iZ''$) and electric modulus ($M^* = 1/C^* = i\omega Z^*$) spectra were recorded in the range 500 mHz - 5 MHz using a Solartron 1250B FRA + 1287 electrochemical interface. Amplitude of perturbation was fixed at 100 mV. In order to distinguish bulk from grain boundary contributions, it was necessary to cool the samples, thereby bringing the naturally high frequency bulk spectral features into the experimental frequency window. Cooling to -70°C was accomplished by submerging the air-tight test apparatus in a bath of ethanol and dry ice.

4.3.5 ICP-OES and Differential Scanning Calorimetry (DSC)

As-synthesized chemical composition of the materials was determined by inductively coupled plasma optical emission spectroscopy (ICP-OES). Average mole fraction deviation from the target composition was less than 3.2% for each constituent (excluding oxygen). All materials considered in this study adopt a high temperature β-NASICON phase at room temperature, but since a conversion to a poorly conducting α phase is possible, we made an attempt to determine this transition temperature. DSC experiments were carried out with a Netzsch DSC 204 F1 Phoenix at a heating/cooling rate of 10°C/min under N_2 flow in the range 150°C to -100°C. No phase transitions were observed in this region, indicating that the β phase is stable to the lower limit of practical operating temperatures.

4.4 Results and Discussion

4.4.1 Phase and Long-Range Order

The conventional NASICON-type solid electrolyte adopts a well-defined structure in the rhombohedral crystal system, where the $M^{4+/3+}$ cations are, to a certain degree, interchangeable and capable of forming solid solutions. Winand et al. [37] have suggested a loose limit on the ionic radius difference between two cations of $\Delta r = 0.1$ Å as the upper limit for good solid solution formation. In the case of the materials studied here, ionic radii as determined by Shannon [32] are:

$Ge^{4+} = 0.53$ Å, $Al^{3+} = 0.535$ Å, $Sn^{4+} = 0.69$ Å. Aluminum and germanium ions have approximately the same radius and can be expected to intermix, but Sn^{4+} and Ge^{4+}, with $\Delta r_{\text{Sn-Ge}} = 0.16$ Å, should not be as amenable to NASICON solid solution formation. Hume-Rothery rules [21] also suggest that this 30% size difference makes solid solution formation unlikely; here, however, the valency, electronegativity, and preferred coordination are similar between the two.

Figure 4.2 shows the powder x-ray diffraction patterns of the four compounds studied in this work. Observed for all but LGSP is a single phase which can be indexed based on $LiGe_2(PO_4)_3$ (JCPDS #80-1922). Shown below the patterns are ticks indicating the peak positions of LGP and LSP ($LiSn_2(PO_4)_3$ JCPDS #87-2078). The tin-bearing phases exhibit peaks located between these two end members, indicating a solid solution of Ge-Sn NASICON phase was formed. This is consistent with previous studies which have reported NASICON solid solutions involving constituents of large size difference [6].

The diffraction pattern of LGP exhibits sharp peaks which is indicative of a well-ordered crystal. In the case of LGSP, however, the diffraction pattern shows broad, overlapping peaks that correspond to two or more NASICON phases with slightly different lattice constants. A similar result was noted in the case of $NaGeSn(PO_4)_3$ [37]. In addition, peaks corresponding to SnP_2O_7 are observed, which can indicate an incomplete reaction [27]. Here, the 900°C calcination temperature may not be high enough to drive the Ge-Sn solid solution formation to completion, due to inadequate mobility of the large Sn^{4+} ion. As a consequence, the long-range order of the crystal is disrupted, likely resulting in small domains of differing compositions close to the nominal LGSP composition, causing the observed broad diffraction peaks.

The diffraction patterns of LAGSP and LAGP both exhibit fairly sharp peaks, confirming NASICON solid solution formation with good long-range crystal ordering. Why LAGSP calcines to a much higher degree than LGSP remains a point in need of further investigation. Possible explanations for enhanced tin cation mobility during calcination include the greater polarizability of Al^{3+} relative to Ge^{4+}, or the higher lithium content which creates additional Li-O bonds which pull electron density away from the path of a migrating tin ion; however, these points remain unclear.

Table 4.1 summarizes the refined lattice constants and unit cell volumes for each material. Similar unit cells are seen for LGP and LAGP, in agreement with previous results [15]. A significant increase in unit cell size is seen for LAGSP, indicating that the incorporation of tin has increased spacing within columns of MO_6 units as well as between them, thereby suggesting an opening of conduction channels. By extension, the estimated hop distance between M1 and M2 sites, as directly extracted from crystal models built from XRD data (such as in Figure 4.1), also increases.

In a qualitative sense, it can be expected that a widening of conduction channels makes Li^+ motion easier and should therefore result in enhanced Li^+ conductivity. This has been observed when comparing Lithium Titanium Phosphate (LTP) with LGP, where the larger unit cell volume of LTP leads to larger conduction channels and lower activation energy [15]. It is worth noting that although LGSP displays the largest unit cell volume and jump distance, these parameters were derived from a diffraction pattern with significantly broadened peaks and are likely overestimated.

Table 4.1: Structural data derived from Rietveld analysis of powder x-ray diffraction data

							Profile Fit Results		
	a (Å)	c (Å)	unit cell V ($Å^3$)	c/a ratio	hop length (Å)	calc density (g/cc)	wRp%	Rp%	χ^2
LAGP	8.25860(7)	20.5794(3)	1215.56(1)	2.49	3.172	3.424	7.56	5.77	1.938
LAGSP	8.411(1)	21.052(3)	1289.8(5)	2.50	3.234	3.494	7.99	6.17	1.421
LGP	8.2756(1)	20.4593(5)	1213.47(3)	2.47	3.171	3.588	25.02*	20.42*	45.98*
LGSP	8.4565(6)	21.083(2)	1305.8(5)	2.49	3.248	3.686	7.67	5.78	1.472

*Orientation effects prevented good calculated intensity fit to the data, however unit cell refinement is reliable

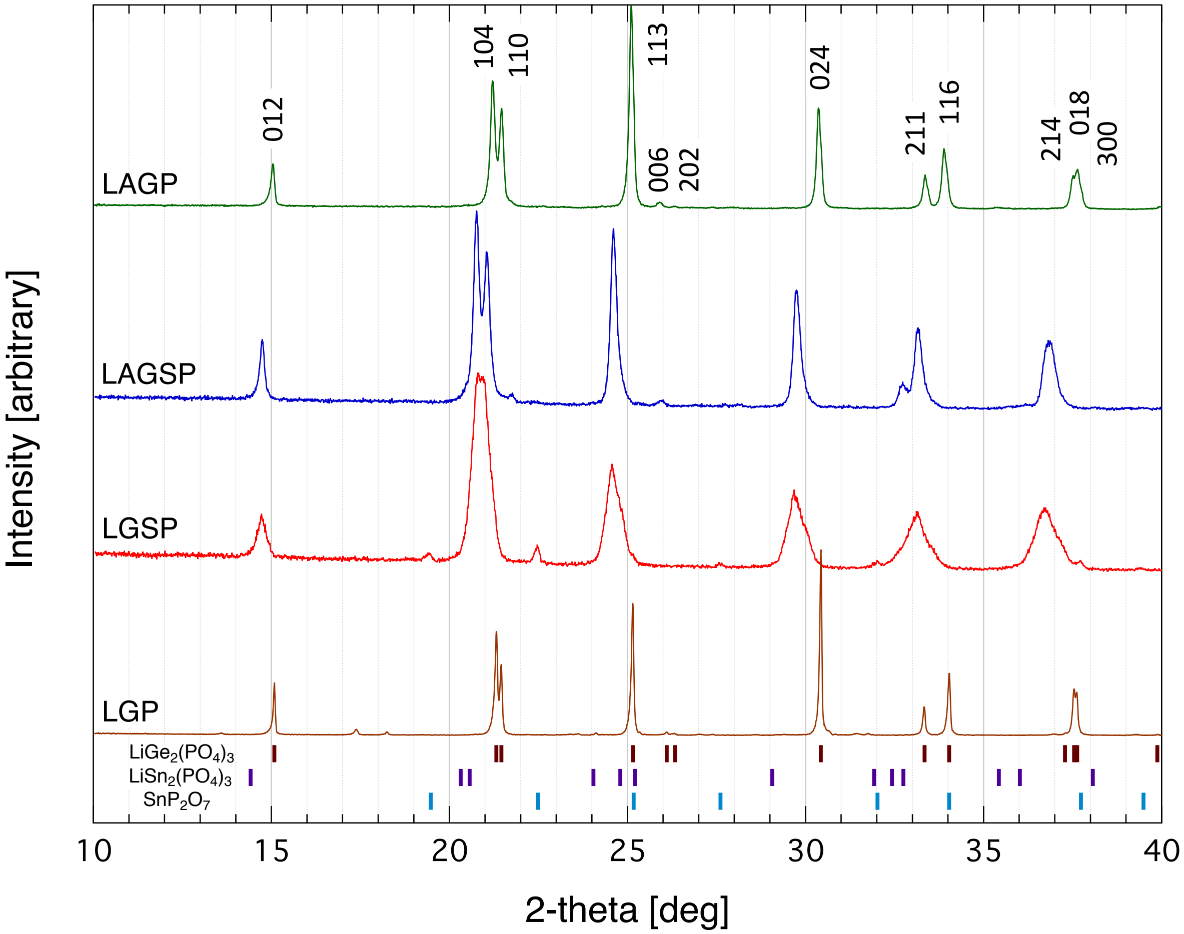

Figure 4.2: X-ray diffraction patterns of the materials studied in this work. Tick marks below the patterns show the peak locations for $LiGe_2(PO_4)_3$ (JCPDS #80-1922), $LiSn_2(PO_4)_3$ (JCPDS #87-2078), and SnP_2O_7 (JCPDS #29-1352) from top to bottom.

4.4.2 Ionic Conductivity

As NASICON materials are renowned to be excellent lithium-ion conductors, we evaluated ionic conductivity for each material using electrochemical impedance spectroscopy (EIS). Figure 4.3a shows a typical complex impedance spectrum, as recorded for LAGSP at -55°C. An equivalent circuit involving resistances (R) and constant phase elements (CPE), as shown in Figure 4.3a, was fit to each spectrum using the software ZView® (Scribner Associates, Inc.). In practice, the impedance spectra approached the Debye model, for which a CPE reduces to a simple capacitive element (C). These models were used to estimate values of R and C for each equivalent circuit.

Following the accepted criterion for order of magnitude of capacitance in electroceramics [12, 17, 19], the features attributed to Li^+ motion in the bulk (high-frequency semicircle, C ~ 10^{-11}F), grain boundaries (intermediate-frequency semicircle, C ~ 10^{-9}F), and at the blocking electrode interfaces (low-frequency spike, C ~ 10^{-6}F) were identified for each material. In this study, however, only the bulk response is considered for analysis. Conductivity data recorded over a range of temperatures is plotted in Figure 4.3b. The bulk conductivity of each material follows the expected Arrhenius relationship:

$$\sigma = \frac{\sigma_0}{T} \exp\left(\frac{-E_a}{kT}\right) \tag{4.1}$$

where E_a is the activation energy for ion conduction, k is the Boltzmann constant, T is the temperature in Kelvin, and σ_0 is the exponential prefactor. From eq 4.1, the slope of the line made by each dataset in Figure 4.3b gives the estimated activation enthalpy for long-range lithium conduction,. Typically, activation energy is reported using the notation E_a, but for the purpose of consistency in the following discussion, we will refer to this parameter as ΔH_c. Figure 4.4 shows the conductivity and activation enthalpy for conduction at room temperature for each material in this study.

As the samples studied here have porosity on the order of 15-20%, the measured conductivities can be expected to be slightly lower than the theoretical conductivity of the material. That is,

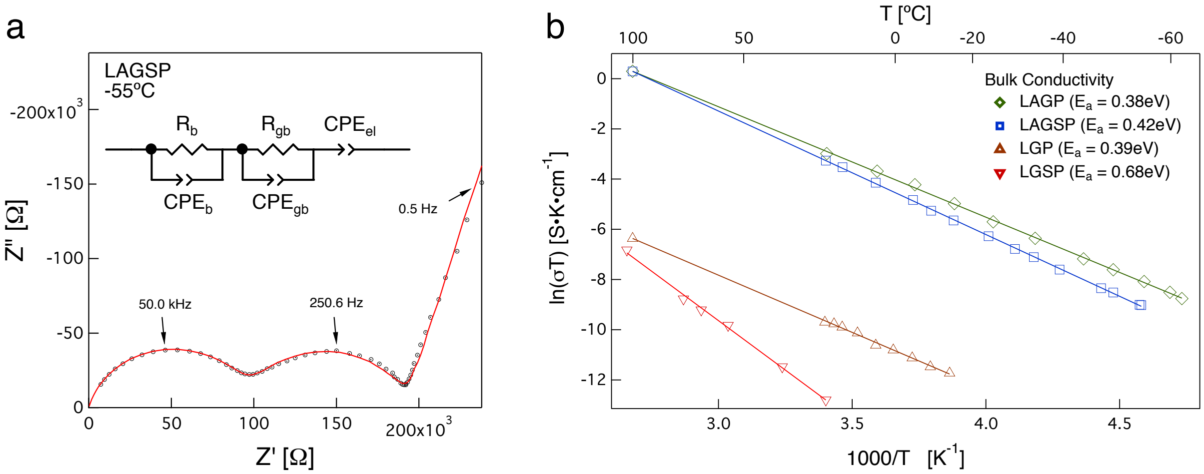

Figure 4.3: (a) Typical complex impedance data, recorded for LAGSP at -55°C (b) Arrhenius plot of conductivity for all materials evaluated. Activation energy, as estimated from the slope of a best-fit line, is displayed in the plot legend.

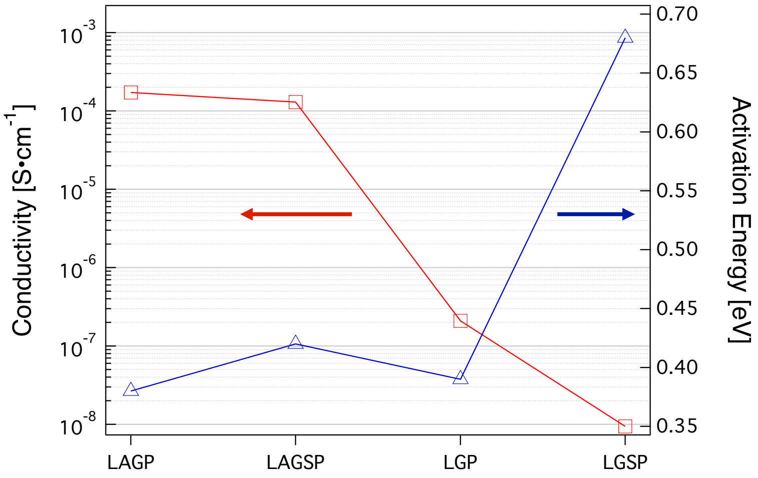

Figure 4.4: Room temperature conductivity and conduction activation energy (ΔH_c) of the materials.

following the Maxwell-Wagner formula derived from the effective medium model [12], the relationship between the experimental total conductivity (σ^{exp}) and extent of porosity (P) follows $\sigma^{exp} = \sigma^{theo}\left[\frac{(2(1-P))}{(2+P)}\right]$, where σ^{theo} is the theoretical total conductivity, and the conductivity of gas-filled pores has been considered to be null. Accordingly, the 15-20% porosity in these samples can affect a drop in total conductivity (mainly from the grain boundary contribution, but also to a limited extent from the bulk) of 20-27% with respect to fully dense samples. We should stress here that as the goals of this study do not involve optimizing conductivity, this porosity does not present a problem. Further, sample density has no impact on the temperature dependence of conductivity, and a standard analysis of activation energy remains valid.

LGP exhibits a low activation energy, but also a low conductivity. The low conductivity of LGP is a function of both the lower Li^+ content as compared to LAGP, and also of Li^+ site occupancy. The thermodynamic reasoning for the latter point will be discussed later. LGSP shows the highest activation energy and lowest conductivity, which is not surprising based on the poor crystal ordering observed by XRD. LAGP and LAGSP both show low activation energies and high conductivities. Compared to LAGP, it is observed that LAGSP has a slightly higher activation energy for conduction and is slightly less conductive at temperatures less than 100°C. This is unexpected based on unit cell information derived from XRD data.

Insight into this unexpected result can be gained by considering the mobility of lithium ions in each material. The prefactor to the Arrhenius expression for ion conductivity encompasses many terms related to structural factors, carrier concentration, hopping frequency, and thermodynamic information on Li^+ motion [23, 14]. A more general expression for the conductivity of any given material is:

$$\sigma = czF\mu \tag{4.2}$$

where c is the concentration of mobile charge carriers, z is the charge on each carrier, F is the Faraday constant, and μ is the mobility of each carrier. Carrier mobility is a function of diffusivity, D, and temperature as follows:

$$\mu = \frac{(zF)D}{kT} \tag{4.3}$$

For solid-state ion conductors, the diffusivity is in turn a function of the structure of the host material and the ion hopping rate (ν) in the material:

$$D = \alpha d^2 \nu \tag{4.4}$$

where α is the reciprocal number of possible jump directions for a mobile ion and d is the jump distance. The thermal activation observed for ion conduction stems from the free energy of ion hopping rate and carrier generation, and follows the form:

$$\nu = \nu_0 \exp\left(\frac{-\Delta G_m}{kT}\right) \tag{4.5}$$

$$\nu_0 = \sqrt{\frac{\Delta H_m}{2m_{Li}d^2}} \tag{4.6}$$

$$c = c_0 \exp\left(\frac{-\Delta G_f}{kT}\right) \tag{4.7}$$

where ν_0 is the fundamental attempt frequency for ion hopping derived from the harmonic potential well expression [35], ΔH_m is the enthalpy of charge carrier motion, m_{Li} is the mass of a lithium cation, c_0 is the concentration of potentially mobile charge carriers, and ΔG_m and ΔG_f are the free energies of ion motion and free carrier formation, respectively. Expanding the free energy terms in eq 4.5 and eq 4.7 and back-substituting up to eq 4.2, the expression for conductivity can now be rewritten as:

$$\sigma = \frac{(z^2F^2)\alpha d^2 c_0 \nu_0 \exp\left(\frac{\Delta S_m + \Delta S_f}{k}\right)}{kT} \exp\left(\frac{-(\Delta H_m + \Delta H_f)}{kT}\right) \tag{4.8}$$

where the exponential prefactor is:

$$\sigma = \frac{(z^2F^2)\alpha d^2 c_0 \nu_0 \exp\left(\frac{\Delta S_m + \Delta S_f}{k}\right)}{k} \tag{4.9}$$

It is clear from eq 4.8 that measured conductivity, and more specifically activation energy for conductivity, is a convolution of free energies of carrier generation and carrier motion. It is possible to separate these contributions and probe only the activation of carrier hopping rate by analysis of the frequency dependence of the bulk spectral feature in EIS data [26, 3, 4, 5, 20]. In the case of solid-state ion conductors, electric modulus spectroscopy often provides more instructive spectra, as the modulus is inversely related to capacitance (M* = 1/C*) and the bulk micro-regions of the material typically have the smallest capacitance by 2-3 orders of magnitude when compared with the grain boundaries [12, 19, 17, 9]. For this analysis, M vs f was plotted and the critical frequency of the loss peak corresponding to the bulk response was followed over the temperature sweeps. Figure 4.5a shows selected data points recorded for LGP that demonstrate the temperature dependence of the imaginary modulus loss peak position. The inset of Figure 4.5a highlights the benefit of working within the modulus formulism, as in contrast to the impedance formulism, the bulk feature is readily observable. From the analysis of $\ln(f_{\text{crit}})$ vs 1000/T shown in Figure 4.5b, the Arrhenius relation for hopping rate ($\nu = f_{\text{crit}}$) from eq 4.10 was solved to extract the bulk hopping enthalpy and entropy terms.

$$\nu = \nu_0 \exp\left(\frac{\Delta S_m}{k}\right) \exp\left(\frac{-\Delta H_m}{kT}\right) \tag{4.10}$$

Of note is that despite a very similar unit cell size, LAGP has a lower hopping enthalpy (ΔH_m) than LGP. This can be rationalized by the fact that LGP has Li^+ only in M1 sites [1], while due to there being more Li^+ than available M1 sites, LAGP has Li^+ in both M1 and M2 [15]. The enthalpy of ion motion is understood as the energy required to strain the lattice and push through the bottleneck plus the energy difference between sites of residence [14]: $\Delta H_m = \Delta H$(fit through bottleneck) + ΔH(site 1 ↔ site 2 energy difference). Having a Li^+ occupying an M2 site lowers the potential of that site and helps lessen the energy difference between M2 and M1 [8]. Therefore, in

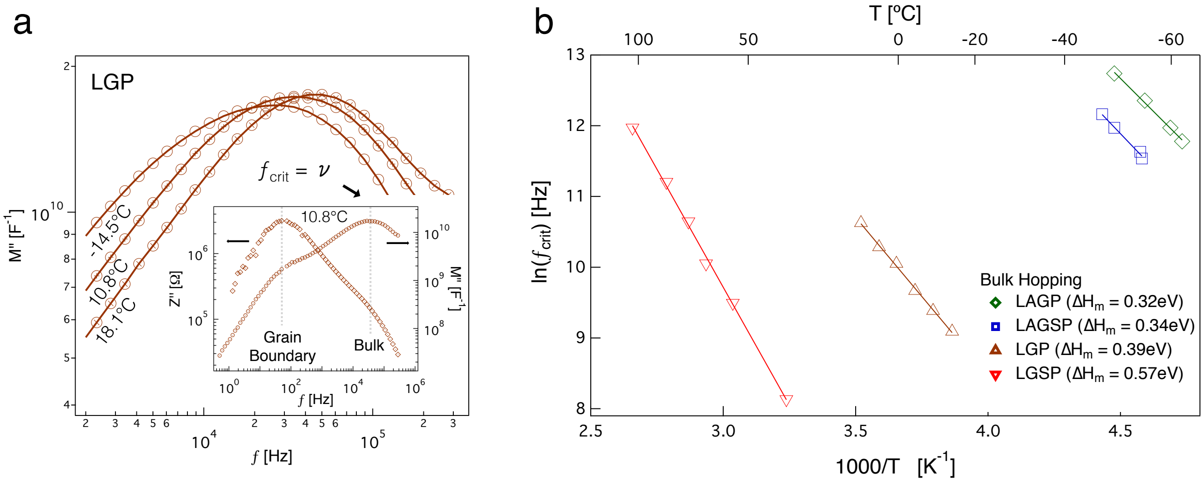

Figure 4.5: (a) Select electric modulus data recorded for LGP showing the temperature dependence. The inset highlights the strength of the electric modulus formulism compared to the impedance formulism in processing the bulk electrical contribution. (b) Arrhenius plot of hopping rate for all materials evaluated. The estimated values of ΔH_m are indicated in the legend.

LAGP, ΔH(M1 ↔ M2 energy difference) is smaller than that of LGP, making ΔH_m smaller.

The enthalpy of motion measured for LAGSP is approximately the same as that of LAGP. Given similar Li^+ occupancy, if the bottleneck was larger in LAGSP than in LAGP as predicted by increased c-axis length, a lower ΔH_m could be expected. This data suggests that local ordering effects in the crystal may affect ion mobility.

The highest ΔH_m is measured for LGSP. Following the lattice-size logic above, LGSP could be expected to have a lower ΔH_m than LGP. However, as XRD patterns have suggested an inhomogeneous structure for LGSP, ion-hopping dynamics are likely also inhomogeneous, and the measured value of ΔH_m should be approached cautiously.

Based on eq 4.8, the difference in activation energy between the values recorded from hopping rate analysis (ΔH_m) and those from conductivity analysis (ΔH_c) must be due to the energy required for free carrier generation (ΔH_f). All of the values of enthalpy and entropy thus derived have been included in Table 4.2. It is worth noting that, in the context of fast ion conductors such as those in the NASICON family, all of the charge carriers are already generated. If charge carriers are present but not participating in conduction, they may for some reason be trapped. In this sense, the difference between measured enthalpies for conduction and hopping may be the additional enthalpy needed to free a trapped charge carrier; $\Delta H_f = \Delta H_{trap} = \Delta H_c - \Delta H_m$. Therefore, eq 4.7 should be understood here as reflecting a change in concentration of charge carriers that are free for motion, having been previously trapped and immobile.

For LGP, all of the potential charge carriers are mobile, as the activation enthalpies for hopping (ΔH_m) and long-range conduction (ΔH_c) are nearly the same. However, for the other compositions, there is a varying degree of additional energy required to free-up charge carriers (Table 4.2).

4.4.3 Entropy

At this point we would like to comment on the observed entropy of motion in this germanium phosphate family, as listed in Table 4.2. While the role and significance of enthalpy terms are fairly

Table 4.2: Summary of results from analysis of impedance and modulus spectroscopy data

			Bulk Hopping		Bulk Li$^+$ Trapping		
	Conductivity, bulk, room temp (S/cm)	Bulk conduction $\Delta \mathrm{H_c}$ (eV)	$\Delta \mathrm{H_m}$ (eV)	$\Delta \mathrm{S_m}$ (J/ mol K)	$\Delta \mathrm{H_c}$ - $\Delta \mathrm{H_m}$ eV	% of total %	RT Diffusivity D_{Li^+} (cm^2/s)
LAGP	1.72E-04 (0.3%)	0.38 (1.0%)	0.32 (3.8%)	2.48	0.06	15.1%	3.82E-09
LAGSP	1.30E-04 (0.2%)	0.42 (0.6%)	0.34 (7.1%)	2.51	0.09	20.5%	2.23E-09
LGP	2.09E-07 (4.1%)	0.39 (2.8%)	0.39 (2.3%)	-24.10	0.01	1.8%	1.18E-11
LGSP	9.42E-09 (24.6%)	0.68 (4.3%)	0.57 (2.1%)	2.29	0.10	15.3%	2.72E-13

well understood, the entropy terms derived from the analysis of dielectric spectroscopy data continue to be a subject of debate [5, 20]. Entropy is a measure of specific ways in which a thermodynamic system can be arranged, with entropy reaching a maximum when equilibrium is reached. In order to define $\Delta \mathrm{S_m}$, we assign the initial state as that of rest, with no applied electric field (no long-range Li$^+$ hopping), and the final state as that of ion motion under an applied field (dynamic long-range Li$^+$ hopping). In the case of LGP, previous studies have confirmed that lithium ions reside exclusively at M1 sites while at rest [1]. Therefore, long-range ion motion through hopping between M1 and M2 sites implies some portion of Li$^+$ are not at the thermodynamically preferred M1 site. This means that the system had a higher entropy at a state of rest (closer to equilibrium), $\Delta \mathrm{S_m}$ is therefore negative, and we can consider ion motion to be entropically hindered.

In the case of LAGP and LAGSP, $\Delta \mathrm{S_m}$ is positive, suggesting that ion motion is entropically favored. This can be interpreted that during ion motion, a higher fraction of the Li$^+$ reside, at least temporarily, on a site of higher thermodynamic preference (lower energy). This calls to question the occupancy of M1 and M2 sites in these aluminum-substituted materials. It is clear that there is more Li$^+$ than there are M1 sites, so some number of Li$^+$ must reside in M2 sites. The bolstered lithium concentration creates new Li-Li repulsive interactions between occupied, neighboring M1 and M2 sites, and the lithium population reconfigures in a way to balance M1 occupancy and Li-Li repulsion. The result is that some Li$^+$ are forced off M1 sites and onto M2 sites to reduce the electrostatic repulsion. Therefore, although the M1 site may be the lower energy, preferred site for a lithium ion, at rest M1 site occupancy is <100% [31, 15, 13]. Now, during a state of dynamic long-range hopping, a greater M1 site occupancy may be temporarily achieved. This makes sense as each M1 site serves as a junction to three conduction pathways and therefore likely spends a greater fraction of time occupied by a passing ion. Therefore the M1/M2 occupancy ratio achieved during long-range motion is slightly more thermodynamically favorable than the site populations at rest, and entropy therefore acts to enhance conductivity.

Although the results shown in Table 4.2 indicate that LGSP has an entropy of motion similar to LAGP and LAGSP, we again attach limited significance to this particular value. As XRD patterns show that there is not a well-defined crystalline phase present, it is currently impossible to define or speculate on site occupancies during rest and steady-state motion in the crystal.

The above discussion may also be approached from the viewpoint of configurational entropy. An M1 site has six neighboring M2 sites, while an M2 site has two neighboring M1 sites. For LGP at rest, all of the lithium ions are sitting on an M1 site and the configurational entropy is already maximized. The average number of options for a lithium jump is six. During steady-state long-range motion some fraction of the lithium ions are now on an M2 site. If you were to take a snapshot of the lithium occupancy in this state and evaluate the number of jump options for each lithium ion, the average number would now be less than six. Therefore, configurational entropy is lower during long-range motion than it is at rest and ΔS_m is negative. A similar rationale can be applied to the aluminum-substituted materials that have a higher fraction of lithium ions on M1 sites during long-range motion as compared to rest.

It is noted that the ΔS_m values measured for LAGP and LAGSP are similar. As these materials likely have comparable M1/M2 site occupancies at rest, as discussed earlier and indicated by similar c/a ratios and lithium concentrations, ion-dynamics during long-range motion should be similar, resulting in a comparable entropy of motion.

In NASICON-type materials containing a mixture of cations of differing size, local distortions not observable with x-ray diffraction may begin to influence ion conductivity. Although XRD may suggest a larger bottleneck size based on increased unit cell dimensions, local distortions can alter bottleneck geometry in a way that actually constricts the conduction pathway [36]. To this end, we describe next the use of vibrational spectroscopy to analyze the local structure of each electrolyte material.

4.4.4 Local Structural Order

Raman spectra were recorded for all materials in order to evaluate the local order of each structure. In phosphate compounds of this nature, the Raman response mainly results from the vibrations of the PO_4 structural group itself [10]. In the case of the NASICON materials in the present study, this PO_4 group provides the link between columns of MO_6 octahedra, sharing oxygen atoms with the $M^{4+/3+}$ and Li^+ ions in the structure. Factor group analysis of these compounds with space group $R\overline{3}c$ dictates 14 Raman active vibrational modes: 6 stretching modes and 8 bending modes for the PO_4 structural unit [34]. Figure 4.6a depicts a portion of a NASICON unit cell as a visual aid for understanding how local structure may influence the vibrational spectrum. Figure 4.6b displays the Raman spectra recorded in the range 200-1300 cm^{-1} for these materials. The observed spectra display sets of peaks in good agreement with the factor group analysis. Peaks in the range 300-500 cm^{-1} may be attributed to components of ν_2 symmetric bending, while those in the range 500-800 cm^{-1} will be components of ν_4 anti-symmetric bending. The higher energy stretching modes are observed in the range 900-1300 cm^{-1}. At present it is difficult to distinguish symmetric (ν_1) from anti-symmetric modes (ν_3), but all of the 6 total expected modes are observed.

From Figure 4.6b, the spectrum of LGP is observed to have sharp, well-defined peaks, while the other compositions demonstrate varying degrees of peak broadness. Previous work by Barj et al. [11] has shown that peak broadening in the Raman spectra of NASICON materials can be attributed to disorder in the PO_4 sublattice. As the stretching modes ν_1 and ν_3 are very sensitive to disorder, it is instructive to focus on the spectral region where they are observed. Figure 4.7 shows a close-up of the range 850-1300 cm^{-1} with the results of a multi-peak fitting analysis accompanying each spectrum. Regarding LGP, the XRD pattern (Figure 4.2) indicates reasonable long-range

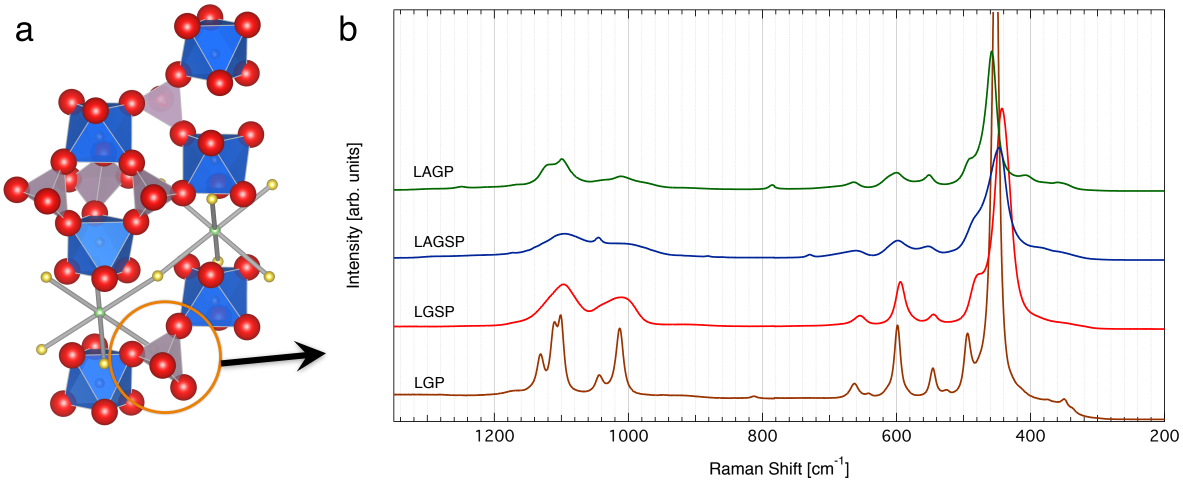

Figure 4.6: (a) Representative depiction of the short-range order in a NASICON crystal responsible for vibrational spectra. (b) Raman spectra recorded for the electrolyte materials in the range 200-1300 cm^{-1}.

ordering and the sharp peaks in the Raman spectrum likewise suggest a high degree of local order in the PO_4 structural units. Indeed, NMR studies have concluded that for single M^{4+} NASICON materials PO_4 distortion is insignificant [30]. If we now consider the substitution of Al^{3+} + Li^+ for Ge^{4+} to create LAGP, we observe that Raman peaks broaden slightly. As Ge^{4+} and Al^{3+} have very similar ionic radii, this broadening can be attributed to the extra Li^+ occupying the M2 site in the structure [11]. With Li^+ in M2 sites, new Li-O bonds are formed and the result is a slight smearing of the vibrational bands of the PO_4 units. Also observed in the spectrum of LAGP (Figure 4.7) is a broad low-intensity peak near 975 cm^{-1} likely due to GeO_2 impurity.

Interesting to note is that peaks from LGSP are actually narrower than those from LAGSP. Barj et al. assert that in poorly calcined materials, i.e. those with a higher degree of cation disorder, the PO_4 sublattice remains more ordered. If calcination is allowed to carry on closer to completion, cation ordering increases at the expense of PO_4 order. Our data may suggest this as well, since LGSP shows poor cation ordering in XRD while LAGSP shows a much higher degree of ordering.

With the additional substitution of tin into LAGP to form LAGSP, we observe a large additional broadening of the vibrational bands. In this case, tin, aluminum, and germanium all occupy the same type of site in the lattice. X-ray diffraction confirms that the substitution is successful and long-range order is maintained, but the disparity in ionic radius between tin and the other two cations manifests in distortions of the local structure.

Sn^{4+} will obviously form a larger MO_6 unit than will Al^{3+} or Ge^{4+}. As can be visualized with the aid of Figure 4.6a, if a large MO_6 unit is adjacent to a smaller one, nearby MO_6 and PO_4 units will need to rotate and/or distort to accommodate the size difference. The PO_4 distortions are recorded in broadened peaks in the Raman spectra (Figure 4.7), and since each oxygen is shared in a bond with a $M^{4+/3+}$ cation, this implies an effect on MO_6 units as well. The heavier M atoms remain fairly ordered as observed in the XRD patterns, and the MO_6 units respond to the lattice strain primarily through rotation about the c-axis [2]. Relative rotation of MO_6 units will obviously distort the geometry of the bottleneck. A distortion and squeezing of bottleneck regions could lead to a closure of the local conduction pathway and a trapping of Li^+. The addition of thermal energy

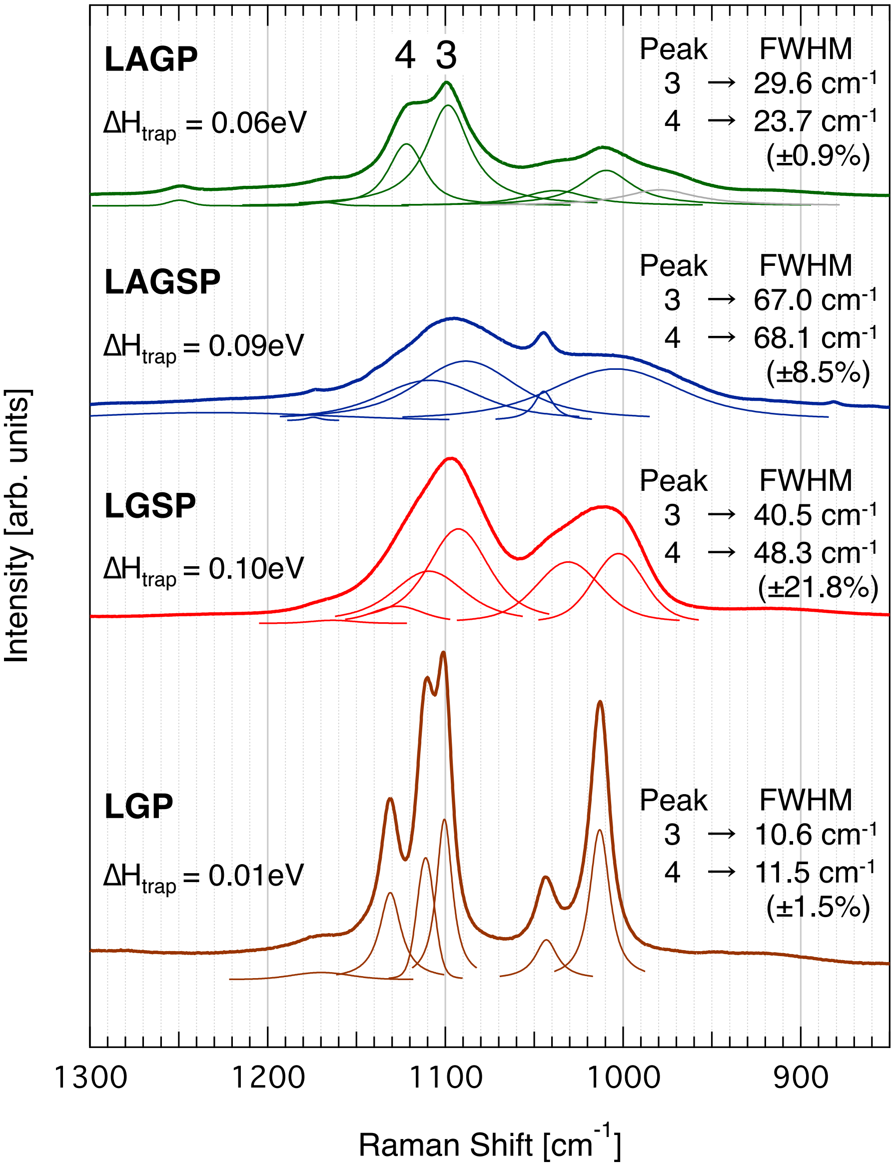

Figure 4.7: Close-up of the Raman spectra in the range 850-1300 cm^{-1} where the PO_4 stretching modes are observed. The computed FWHM of two clear peaks is presented along with the trapping enthalpy. These results provide insight into local structural distortion introduced by the various substitutions.

and the resulting structural expansion would help to reopen the closed pathways, and this will be recorded in conductivity analysis as activation energy for charge carrier generation.

By isolating the activation energy for lithium hopping (ΔH_m) and comparing with the overall activation energy for long-range lithium conduction (ΔH_c), this additional carrier generation energy (ΔH_f) can be quantified. As stated earlier, charge carriers in fast ion conductors are already generated, which means that for the materials studied here: $\Delta H_f = \Delta H_{trap}$ (see Table 4.2). This trapping enthalpy is seen to follow the trend in observed peak broadening in the Raman spectra (Figure 4.7). LAGP and LAGSP display similar values for bulk hopping activation enthalpy, as reported in Table 4.2. While the incorporation of tin appears to create enlarged bottlenecks based on unit cell enlargement, the reality is that many bottlenecks are distorted and are in fact not any easier for a lithium ion to cross. As carriers trapped in constricted conduction pathways are freed with the addition of thermal energy, they begin to participate in conduction; this is the source of the additional activation energy observed in impedance data and described by eq 4.7.

4.5 Conclusions

In this work, we have synthesized new NASICON compounds of the Ge-Sn solid solution and evaluated their structure and ionic conductivity with x-ray diffraction, Raman spectroscopy, and dielectric spectroscopy. Increases in unit cell size and c-axis length following the incorporation of Sn suggest that an enhancement in conductivity should be expected, however this is not the case. Increased activation enthalpy for ion conduction is explained by considering local distortions in structural polyhedra observed in Raman spectra. Disorder in MO_6 units results in a distortion of local bottleneck regions, partially closing the local conduction pathway and trapping Li^+ ions. An extra thermal activation is observed in EIS data that is attributed to the energy required to re-open conduction pathways and free trapped Li^+. This work demonstrates that care must be taken in the design of NASICON-type electrolytes such that the choice of constituents does not introduce a high degree of local structural distortion, which may decrease overall electrolyte performance.

References

[1] M Alami, R Brochu, J L Soubeyroux, P Gravereau, G Le Flem, and P Hagenmuller. Structure and thermal expansion of $LiGe_2(PO_4)_3$. Journal of Solid State Chemistry, 90(2):185–193, February 1991.

[2] James Alamo and Rustum Roy. Crystal chemistry of the $NaZr_2(PO_4)_3$, NZP or CTP, structure family. Journal of Materials Science, 21(2):444–450, February 1986.

[3] D P Almond, G K Duncan, and A R West. The Determination of Hopping Rates and Carrier Concentrations in Ionic Conductors by a New Analysis of Ac Conductivity. Solid State Ionics, 8(2):159–164, 1983.

[4] D P Almond and A R West. Impedance and modulus spectroscopy of "real" dispersive conductors. Solid State Ionics, 11(1):57–64, September 1983.

[5] D P Almond and A R West. The activation entropy for transport in ionic conductors. Solid State Ionics, 23(1):27–35, 1987.

[6] Hiromichi Aono, Eisuke Sugimoto, Yoshihiko Sadaoka, N Imanaka, and Gin-ya Adachi. Ionic-Conductivity and Sinterability of Lithium Titanium Phosphate System. Solid State Ionics, 40-1:38–42, August 1990.

[7] Hiromichi Aono, Eisuke Sugimoto, Yoshihiko Sadaoka, Nobuhito Imanaka, and Gin-ya Adachi. Electrical Properties and Sinterability for Lithium Germanium Phosphate $Li_{1+x}M_xGe_{2-x}(PO_4)_3$, M=Al, Cr, Ga, Fe, Sc, and In Systems. Bulletin of the Chemical Society of Japan, 65(8):2200–2204, 1992.

[8] K Arbi, M A París, and J Sanz. Li mobility in Nasicon-type materials $LiM_2(PO_4)_3$, M = Ge, Ti, Sn, Zr and Hf, followed by 7Li NMR spectroscopy. Dalton Trans, 40(39):10195, 2011.

[9] K Arbi, M Tabellout, M Lazarraga, J Rojo, and J Sanz. Non-Arrhenius conductivity in the fast lithium conductor $Li_{1.2}Ti_{1.8}Al_{0.2}(PO_4)_3$: A Li7 NMR and electric impedance study. Physical Review B, 72(9):094302, September 2005.

[10] M Barj, G Lucazeau, and C Delmas. Raman and infrared spectra of some chromium Nasicon-type materials: Short-range disorder characterization. Journal of Solid State Chemistry, 100(1):141–150, September 1992.

[11] M Barj, H Perthuis, and P Colomban. Relations between sublattice disorder, phase transitions and conductivity in NASICON. Solid State Ionics, 9-10:845–850, December 1983.

[12] Evgenij Barsoukov and James Ross Macdonald. Impedance Spectroscopy. Theory, Experiment, and Applications. John Wiley & Sons, New Jersey, 2 edition, 2005.

[13] J P Boilot, G Collin, and P Colomban. Relation Structure Fast Ion Conduction in the Nasicon Solid-Solution. Journal of Solid State Chemistry, 73(1):160–171, March 1988.

[14] Peter G Bruce. Solid State Electrochemistry. Cambridge University Press, New York, 1 edition, June 1997.

[15] M Cretin and P Fabry. Comparative study of lithium ion conductors in the system $Li_{1+x}Al_xA_{2x}{}^{IV}$ $(PO_4)_3$ with A^{IV}=Ti or Ge and 0x07 for use as Li^+ sensitive membranes. Journal Of The European Ceramic Society, 19(16):2931–2940, December 1999.

[16] Gaelle Delaizir, Virginie Viallet, Abdelmaula Aboulaich, Renaud Bouchet, Laurence Tortet, Vincent Seznec, Mathieu Morcrette, Jean-Marie Tarascon, Patrick Rozier, and Mickael Dollé. The Stone Age Revisited: Building a Monolithic Inorganic Lithium-Ion Battery. Advanced Functional Materials, 22(10):2140–2147, February 2012.

[17] Adolfo Delgado, Mario F García-Sánchez, Jean-Claude M'Peko, A Rabdel Ruiz-Salvador, Geonel Rodríguez-Gattorno, Yuri Echevarría, and Froilan Fernández-Gutierrez. An Elementary Picture of Dielectric Spectroscopy in Solids: Physical Basis. Journal Of Chemical Education, 80(9):1062, September 2003.

[18] Jinkui Feng, Hui Xia, Man On Lai, and Li Lu. NASICON-Structured $LiGe_2(PO_4)_3$with Improved Cyclability for High-Performance Lithium Batteries. Journal Of Physical Chemistry C, 113(47):20514–20520, November 2009.

[19] J G Fletcher, A R West, and J T S Irvine. The Ac-Impedance Response of the Physical Interface Between Yttria-Stabilized Zirconia and $YBa_2Cu_3O_{7-X}$. Journal of The Electrochemical Society, 142(8):2650–2654, August 1995.

[20] Germà Garcia-Belmonte and Juan Bisquert. Entropy factor in the hopping frequency for ionic conduction in oxide glasses induced by energetic clustering. The Journal of Chemical Physics, 123(7):074504, 2005.

[21] Joel Irwin Gersten and Frederick William Smith. The Physics and Chemistry of Materials. Wiley New York, New York, 1 edition, 2001.

[22] HY-P Hong. Crystal structures and crystal chemistry in the system $Na_{1+x}Zr_2Si_xP_{3x}O_{12}$. Materials Research Bulletin, 11(2):173–182, 1976.

[23] Robert Huggins. Advanced Batteries. Materials Science Aspects. Springer, New York, 1 edition, November 2008.

[24] S Li. Phase relationships and electrical conductivity of $Li_{1+x}Ge_{2-x}Al_xP_3O_{12}$ and $Li_{1+x}Ge_{2-x}Cr_xP_3O_{12}$ systems. Solid State Ionics, 28-30:1265–1270, September 1988.

[25] Enrique R Losilla, Miguel A G Aranda, Sebastián Bruque, Miguel A París, Jesús Sanz, and Anthony R West. Understanding Na Mobility in NASICON Materials: A Rietveld, 23Na and 31P MAS NMR, and Impedance Study. Chemistry of Materials, 10(2):665–673, February 1998.

[26] Pilar Maldonado-Manso, Enrique R Losilla, María Martínez-Lara, Miguel A G Aranda, Sebastián Bruque, Fatima E Mouahid, and Mohammed Zahir. High Lithium Ionic Conductivity in the $Li_{1+x}Al_xGe_yTi_{2-x-y}(PO_4)_3$NASICON Series. Chemistry of Materials, 15(9):1879–1885, May 2003.

[27] Ana Martinez, José M Rojo, Juan E Iglesias, Jesús Sanz, and Rosa M Rojas. Formation Process of $LiSn_2(PO_4)_3$, a Monoclinically Distorted NASICON-Type Structure. Chemistry of Materials, 6(10):1790–1795, October 1994.

[28] Ana Martinez-Juarez, Carlos Pecharromán, Juan E Iglesias, and José M Rojo. Relationship between Activation Energy and Bottleneck Size for Li^+ Ion Conduction in NASICON Materials of Composition LiMM'$(PO_4)_3$; M, M'= Ge, Ti, Sn, Hf. The Journal of Physical Chemistry B, 102(2):372–375, 1998.

[29] Yoshinori Noguchi, Eiji Kobayashi, Larisa S Plashnitsa, Shigeto Okada, and Jun-ichi Yamaki. Fabrication and performances of all solid-state symmetric sodium battery based on NASICON-related compounds. Electrochimica Acta, 101:59–65, July 2013.

[30] Miguel A París and Jesús Sanz. Structural changes in the compounds $LiM_2{}^{IV}(PO_4)_3$ (M^{IV}=Ge, Ti, Sn, and Hf) as followed by P31 and Li7 NMR. Physical Review B, 55(21):14270–14278, June 1997.

[31] D Tran Qui, S Hamdoune, J L Soubeyroux, and E Prince. Neutron powder diffraction study of solid solution $Li_{1+x}Ti_{2x}In_xP_3O_{12}$. Journal of Solid State Chemistry, 72(2):309–315, February 1988.

[32] R D Shannon. Revised effective ionic radii and systematic studies of interatomic distances in halides and chalcogenides. Acta Crystallographica Section A, 32(5):751–767, September 1976.

[33] Yugang Sun. Lithium ion conducting membranes for lithium-air batteries. Nano Energy, 2:801–816, 2013.

[34] P Tarte, A Rulmont, and C Merckaert-Ansay. Vibrational spectrum of nasicon-like, rhombohedral orthophosphates $M^IM_2{}^{IV}(PO_4)_3$. Spectrochimica Acta Part A: Molecular Spectroscopy, 42(9):1009–1016, 1986.

[35] C Wert and C Zener. Interstitial Atomic Diffusion Coefficients. Physical Review, 76(8):1169–1175, 1949.

[36] J M Winand, A Rulmont, and P Tarte. Ionic conductivity of the $Na_{1+x}M_x{}^{III}Zr_{2-x}(PO_4)_3$ systems (M = Al, Ga, Cr, Fe, Sc, In, Y, Yb). Journal of Materials Science, 25(9):4008–4013, September 1990.

[37] Jean-Marc Winand, André Rulmont, and Pierre Tarte. Nouvelles solutions solides $L^I(M^{IV})_{2x}(N^{IV})_x(PO_4)_3$ (L = Li,Na M,N = Ge,Sn,Ti,Zr,Hf) Synthèse et étude par diffraction x et conductivité ionique. Journal of Solid State Chemistry, 93(2):341–349, August 1991.

[38] Hiroshi Yamamoto, Mitsuharu Tabuchi, Tomonari Takeuchi, Hiroyuki Kageyama, and Osamu Nakamura. Ionic conductivity enhancement in $LiGe_2(PO_4)_3$ solid electrolyte. Journal Of Power Sources, 68(2):397–401, October 1997.

[39] Ming Zhang, Keita Takahashi, Ichiro Uechi, Yasuo Takeda, Osamu Yamamoto, Dongmin Im, Dong-Jonne Lee, Bo Chi, Jian Pu, Jian Li, and Nobuyuki Imanishi. Water-stable lithium anode with $Li_{1.4}Al_{0.4}Ge_{1.6}(PO_4)_3$-$TiO_2$ sheet prepared by tape casting method for lithium-air batteries. Journal Of Power Sources, 235(C):117–121, August 2013.

Chapter 5

The Role of Entropy and Enthalpy in NASICON-Type Electrolytes

5.1 Abstract

Herein we report a study on the energetics of ion transport in NASICON-type solid electrolytes. A sol-gel procedure was used to synthesize NASICON-type lithium-ion conductors with nominal compositions $\mathrm{Li_{1+x}Al_xGe_{2\text{-}x}(PO_4)_3}$ where $0 \le X \le 0.6$. Trends in conductivity and activation energies, including both enthalpic and entropic contributions, were examined with electrochemical impedance spectroscopy. Physical interpretations of these results are drawn from structural characterizations performed by synchrotron powder x-ray diffraction and Raman spectroscopy. Considering $X = 0 \rightarrow 0.6$, we conclude that initial drops in activation energy are driven by a growing $\mathrm{Li^+}$ population on M2 sites, while later increases in activation energy are driven by changes in average bottleneck size caused by the Al-for-Ge substitution. Values of the entropy of motion are rationalized physically by considering the changing configurational potential of the mobile $\mathrm{Li^+}$ population with changes in X value. We conclude that entropic contributions to free energy of activation amount to $\le 22\%$ of enthalpy contributions at room temperature. These insights suggest that while entropic contributions are not insignificant, more attention should be paid to lowering activation energy when designing a new NASICON-type conductor.

5.2 Introduction

With the demand for high-performing rechargeable lithium-ion batteries continually on the rise, much research effort over the last decade has been spent on the development on materials enhanced electrochemical properties. As lithium-air batteries show great promise to meet many performance needs, a targeted research effort to develop high-conducting solid-state separator materials has developed. Materials of the Sodium Superionic Conductor (NASICON) family are a promising candidate as many have demonstrated high conductivity, stability, and mechanical integrity [22, 24, 10, 29]. With many researchers working on developing these materials, it is helpful to have a clear picture of the various factors that contribute to measured conductivities.

In the case of ion-conducting solids such as the NASICON-type materials, conductivity (σ) is governed by the relation $\sigma = \mathrm{c}\ \mu\ \mathrm{q}$, where c is the density of charge carriers, μ is the mobility of the charge carriers, and q is the charge carried by each carrier. Here, we can see two obvious ways of increasing the conductivity of such a material: increasing the concentration of charge carriers, or increasing carrier mobility. Indeed, a common method of enhancing the conductivity of the established NASICON-type conductor lithium germanium phosphate is with a heterovalent doping scheme [27, 17]: $\mathrm{LiGe_2(PO_4)_3} \rightarrow \mathrm{Li_{1+x}Al_xGe_{2\text{-}x}(PO_4)_3}$. Since the $\mathrm{Ge^{4+}}$ (0.53 Å) and $\mathrm{Al^{3+}}$ (0.535 Å) ions have nearly the same radius, and there are many unfilled sites available for the additional lithium ions in the structure, the substitution is easily accomplished. This doping has been reported to increase conductivity up to three orders of magnitude. A common guideline of solid ionic conductor design is that maximum conductivity should be achieved when exactly half of the available mobile ion sites are filled. By this logic, a maximum conductivity would be reached when the X value in $\mathrm{Li_{1+x}Al_xGe_{2\text{-}x}(PO_4)_3}$ is unity; instead, maximum conductivity is typically reported in the range $0.4 \leq X \leq 0.6$ [9, 28]. This indicates that there are more factors to consider in electrolyte design than simply the concentration of charge carriers. Structure, of course, plays an important role in defining these other factors. In NASICON crystals of general formula $\mathrm{LiM_2(PO_4)_3}$, columns of $\mathrm{MO_6}$ octahedra are linked by $\mathrm{PO_4}$ tetrahedra [15]. Lithium ions reside in two possible sites, the M1 site being 6-fold coordinated and located directly between two stacked $\mathrm{MO_6}$ units, and/or the M2 site which lies in an 8-fold coordinated location between two columns of $\mathrm{MO_6}$ units. During long-range motion, the ions hop between these two sites as they traverse the crystal. Figure 5.1 shows the key points of the NASICON structure.

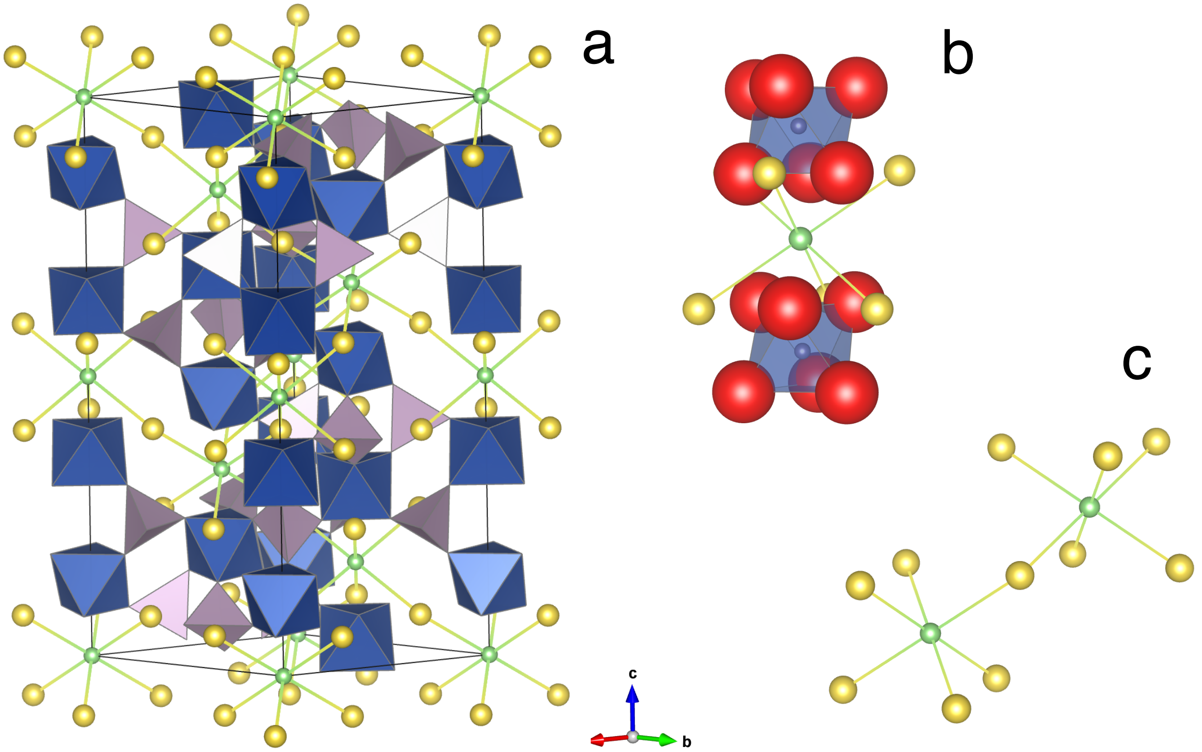

Figure 5.1: (a) Representation of a typical NASICON unit cell. Blue octahedra are MO_6 units, purple tetrahedra are PO_4 units, green spheres are M1 sites, and yellow spheres are M2 sites. Pathways for Li^+ motion are drawn between M1 and M2 sites. (b) Close-up view of the conduction bottleneck region with the oxygen atoms in red and Al/Ge visible in the middle of the octahedra. (c) Small section of the Li^+ conduction pathways showing the relative configuration of M1 (green) and M2 (yellow) sites.

Of the factors influencing this motion, we must consider the restrictive bottleneck points that form a window between mobile sites (shown in Figure 5.1b), the relative energies of each ion site, and the total lithium population in these sites. In a previous report we presented evidence that the equilibrium configuration of lithium ions across available sites is influenced by composition and plays a role in determining the overall conductivity of the material [14]. At rest, in the absence of an electric field, a certain distribution of Li^+ across M1 and M2 sites exists. Under the influence of a field which causes the activation of the charge carrier population and long-range Li^+ motion, a different distribution may exist. We hypothesize that it is the difference between these two distributions, which represent two different configurations of the Li^+ population, that gives rise to the measurable entropy of ion motion.

To provide clarity about the many factors that influence conductivity in NASICON-type conductors, and attempt to produce a better understanding of what entropy terms represent, we have designed a study around the $Li_{1+x}Al_xGe_{2-x}(PO_4)_3$ system. In this system, the similar size of Al^{3+} and Ge^{4+} allow good mixing, where the lattice parameters of such solid solutions exist in a tight range and structural distortion should be minimized. By employing a sol-gel synthesis we are afforded careful control over chemistry and crystal homogeneity. This process also produces smaller grains with a tighter size distribution, which is beneficial for the accuracy of subsequent analyses. Here, we synthesize $Li_{1+x}Al_xGe_{2-x}(PO_4)_3$ with the range of X values $0 \le X \le 0.6$. We use electrochemical impedance spectroscopy (EIS) to measure various thermodynamic parameters that define conductivity, synchrotron powder x-ray diffraction (XRD) to accurately study the crystal structure of each material, and Raman spectroscopy to study the local bonding environment of the structure. We leverage observed structural features to propose physical explanations for trends in thermodynamic parameters of conductivity, and also to provide additional evidence for our configurational entropy theory.

5.3 Experimental Methods

5.3.1 Synthesis of Powders

A Pechini-type sol-gel process using citric acid and ethylene glycol was used to synthesize all of the materials evaluated in this study. All solutions were prepared from as-received precursors in proper stoichiometric ratios. Moisture sensitive precursors were stored in a dry argon glovebox prior to use. Aqueous solutions of precursors were prepared with the [citric acid + ethylene glycol : metal ion] ratio fixed at [4:1]. First, an appropriate amount of citric acid (Alfa 99.5%+) was dissolved in deionized water heated to 60°C, followed by the addition of stoichiometric amounts of $LiNO_3$ (Alfa 99%), $Al(NO_3)_3{\cdot}9H_2O$ (Alfa 98-102%), $Ge(OC_2H_5)_4$ (Gelest >95%), and $NH_4H_2PO_4$ (Sigma ≥99.99%), in that order. Ethylene glycol (Mallinckrodt Chemicals 99%) was then added to promote polymerization of the complex upon drying, and the mixture was held at 80°C under vigorous stirring for 6 hrs. Finally, the sol was transferred to an oven and dried at 120°C overnight. The resulting dry gel was ground with mortar and pestle and treated for 8 hrs at 500°C to decompose the organics, which left a fine powder coated in carbon residue. This powder was again ground with mortar and pestle and treated an additional 8 hrs at 800-900°C to burn off carbon residue and complete the reaction to form fine particles of the NASICON-type materials. The final treatment temperature was chosen based on previously reported phase purity data for the $LiGe_2(PO_4)_3$ system [12, 20, 27], and on our own observations which show that significant phase separation into GeO_2 and $Li_9Al_3(P_2O_7)_3(PO_4)_3$, likely driven by lithium loss, occurs above the chosen temperature.

While the sol-gel synthesis procedure can yield small grain size, these grains often sinter into larger, irregular particles during the final heat treatment. To reduce and homogenize particle size for subsequent analyses, each powder was wet-milled in a planetary ball-miller for 30 min at 500 rpm. Agate milling jars and media were employed and ethanol was used as the solvent.

5.3.2 Powder X-ray Diffraction (XRD)

As synthesized and post-wet-milled powders were qualified using CuK$_\alpha$ radiation ($\lambda = 1.5418$Å) in the range 10-65° 2θ using a Bruker D2 Phaser operated at 30 kV and 10 mA. A Lynxeye 1D detector with a step size of 0.02° and collection time of 1 s per step were employed. For a detailed structural analysis, synchrotron x-ray diffraction patterns were collected on beamline 11-BM at the Advanced Photon Source at Argonne National Laboratory. Patterns were acquired using a wavelength of $\lambda = 0.4138$Å in the range 2-50° 2θ, with a step size of 0.001° and counting time of 1s.

Rietveld refinement and analysis of synchrotron XRD data was carried out using the General Structure Analysis System (GSAS) software with EXPGUI user interface. Starting structural models were created from JCPDS File Card No. 80-1922 ($LiGe_2(PO_4)_3$) and results from Ref [18]. At the start of refinement, structural models assumed nominal Al substitution and full occupancy of the lithium M1 site, with the remainder of lithium atoms placed on site M2. A basic refinement strategy was employed as follows. First, lattice constants were allowed to vary until an acceptable fit to the unit cell was found. Next, parameters affecting line shape were allowed to vary until an acceptable fit to peak profiles was obtained. Following background refinement, atomic positions were allowed to freely vary, followed by isotropic displacement parameters. Once this model had converged, the Al/Ge ratio was refined, and finally, the occupancy of the lithium M1 site. Every few refinement cycles, the occupancy of site M2 was manually updated based on Al/Ge ratio and M1 occupancy. Constraints were applied such that all O Uisos were equal, Al and Ge Uisos were equal, and Al-Ge site occupancy was unity. As it is very difficult to analyze lithium content in a material with x-rays due to poor scattering, Uiso for Li was fixed at a reasonable value of 0.025Å^2. Note, for each composition besides X = 0, the refined value of X is slightly different than the nominal value. In the discussion we reference nominal X values, but all calculations and estimations are performed with X values determined from synchrotron x-ray data.

5.3.3 Raman Spectroscopy

Raman spectra were recorded in the range 200-1300 cm^{-1} using a JASCO NRS-3100 system equipped with a 532 nm laser at a power level of 22 mW. Raman shift was calibrated using a silicon standard and accuracy was estimated to be ±2.5 cm^{-1}

5.3.4 Electrochemical Impedance Spectroscopy

Samples for EIS measurements and subsequent analysis were prepared by uniaxially pressing powders into cylindrical pellets in a stainless steel die at 330 MPa. Pellets approximately 6 mm in diameter and 1 mm in thickness resulted. Each pellet was sintered for 8 hrs at the chosen final calcination temperature on platinum foil in air. Final density was calculated from pellet geometry and weight. From the theoretical densities estimated from refined x-ray diffraction patterns, final relative density of each sample was $\geq$90%. We note an unexpected disintegration of sintered pellets of $LiGe_2(PO_4)_3$ in deionized water, which prevented Archimedes density measurements in this medium. Analysis of dried material collected from measurement beakers suggests no chemical or structural changes as a result of disintegration.

To enable electrical measurements, a Technics Hummer V Sputter Coater was used to deposit 500nm of pure gold onto each face of the pelletized samples. Pellets were dried for several hours in a vacuum oven and then sealed in a custom apparatus that allowed tests to be conducted in flowing dry argon, thereby excluding the effects of moisture.

Impedance ($Z^* = Z \quad iZ$) spectra were recorded in the range 1 Hz - 1 MHz using a Solartron 1250B FRA + 1287 electrochemical interface. Amplitude of perturbation was fixed at 100 mV. To best resolve bulk impedance contributions, it was necessary to cool the samples, thereby bringing the naturally high frequency bulk spectral features into the experimental frequency window. Cooling to -70°C was accomplished by submerging the air-tight test apparatus in a bath of ethanol and dry ice.

5.4 Results

5.4.1 Ionic Conductivity

In order to characterize conductivity and determine the thermodynamic parameters governing ion motion in these solid-state conductors, we evaluated each material using electrochemical impedance spectroscopy (EIS). Spectra were recorded for each material at temperatures from room temperature down to -65°C. This was necessary to best resolve the bulk feature of each impedance spectrum, as this naturally high frequency response can be slowed into the experimental frequency window with cooling. An example spectrum is shown in Figure 5.2. As shown in the inset of Figure 5.2, each spectrum was fit with an equivalent circuit involving resistances (R) and constant phase elements (CPE) using the software ZView®.

The constant phase element represents a non-ideal capacitor with an impedance response of the form: $\mathrm{Z_{CPE}} = 1/\mathrm{Q}(\mathrm{j}\omega)^{\mathrm{n}}$ [6], where Q is a capacitance-like empirical parameter, ω is the frequency of perturbation, and $0 \leq \mathrm{n} \leq 1$. The parameter n is typically associated with the existence of either a distribution of capacitance values, or a correlation between mobile charges in the dielectric structure [21]. When n = 1, the CPE reduces to a simple capacitive element (C). In the materials studied here, bulk values of n varied $0.87 \leq \mathrm{n} \leq 0.99$. Following the accepted criterion for order of magnitude of capacitance in electroceramics [6, 11, 13], the features attributed to Li^{+} motion in the bulk (high-frequency semicircle, $\mathrm{C}{\sim}10^{-11}\mathrm{F}$), grain boundaries (intermediate-frequency semicircle, $\mathrm{C}{\sim}10^{-9}\mathrm{F}$), and at the blocking electrode interfaces (low-frequency spike, $\mathrm{C}{\sim}10^{-6}\mathrm{F}$) were identified for each material.

In this study, we focus on the analysis of the bulk response only. Using the estimated resistance values from the spectrum fitting of room temperature data, we calculate the room temperature conductivity by applying the relationship: $\sigma_{\mathrm{B}} = \mathrm{t} / (\mathrm{A}\ \mathrm{R_B})$, where σ_{B} is the bulk conductivity, t is the sample thickness, and A is the geometrical area of the sample faces. These results are shown in Figure 5.3a.

Here, there is a clear trend of room temperature conductivity with composition. As the X

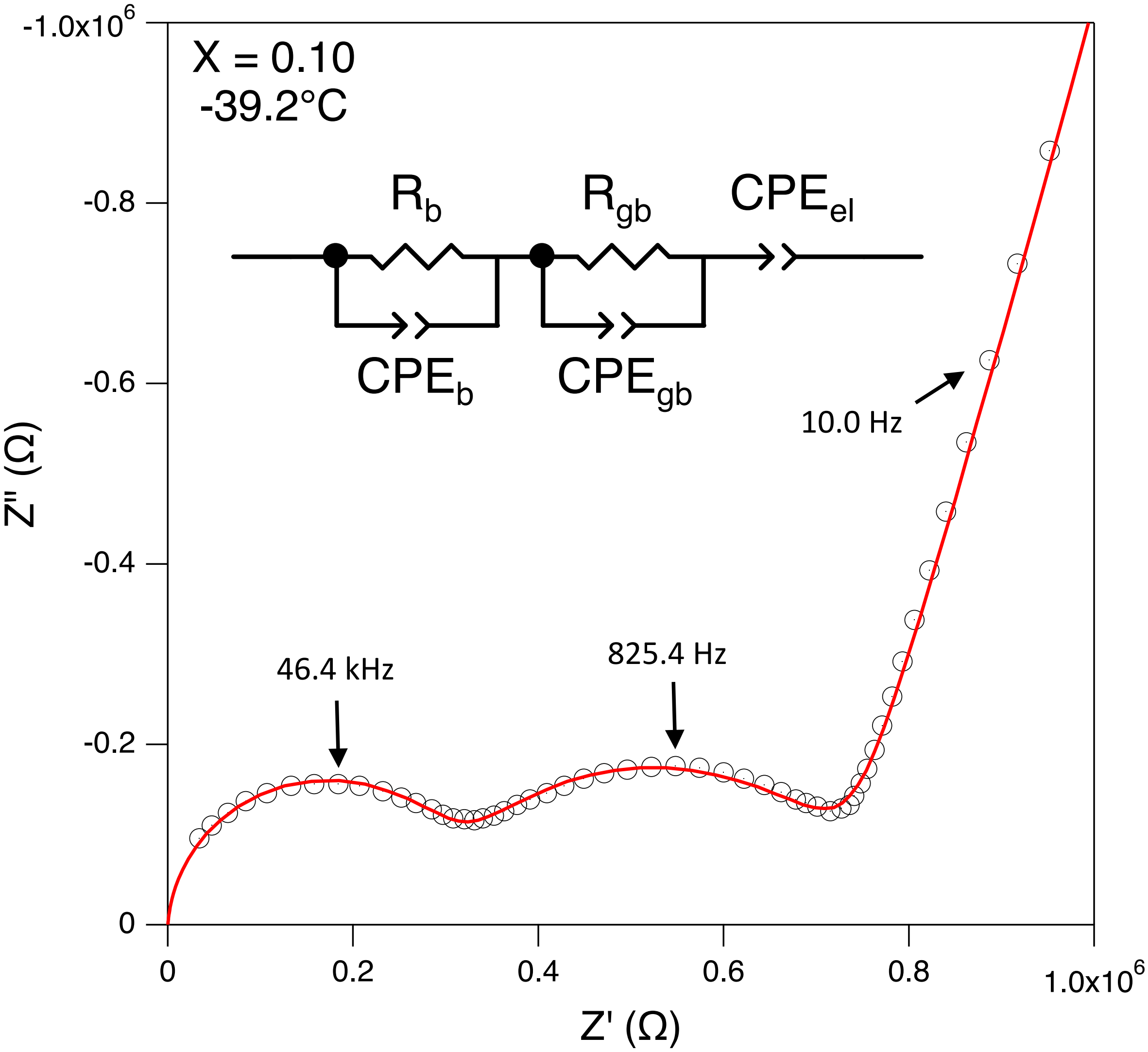

Figure 5.2: Typical complex impedance data, recorded for composition X=0.10 at -39.2°C.

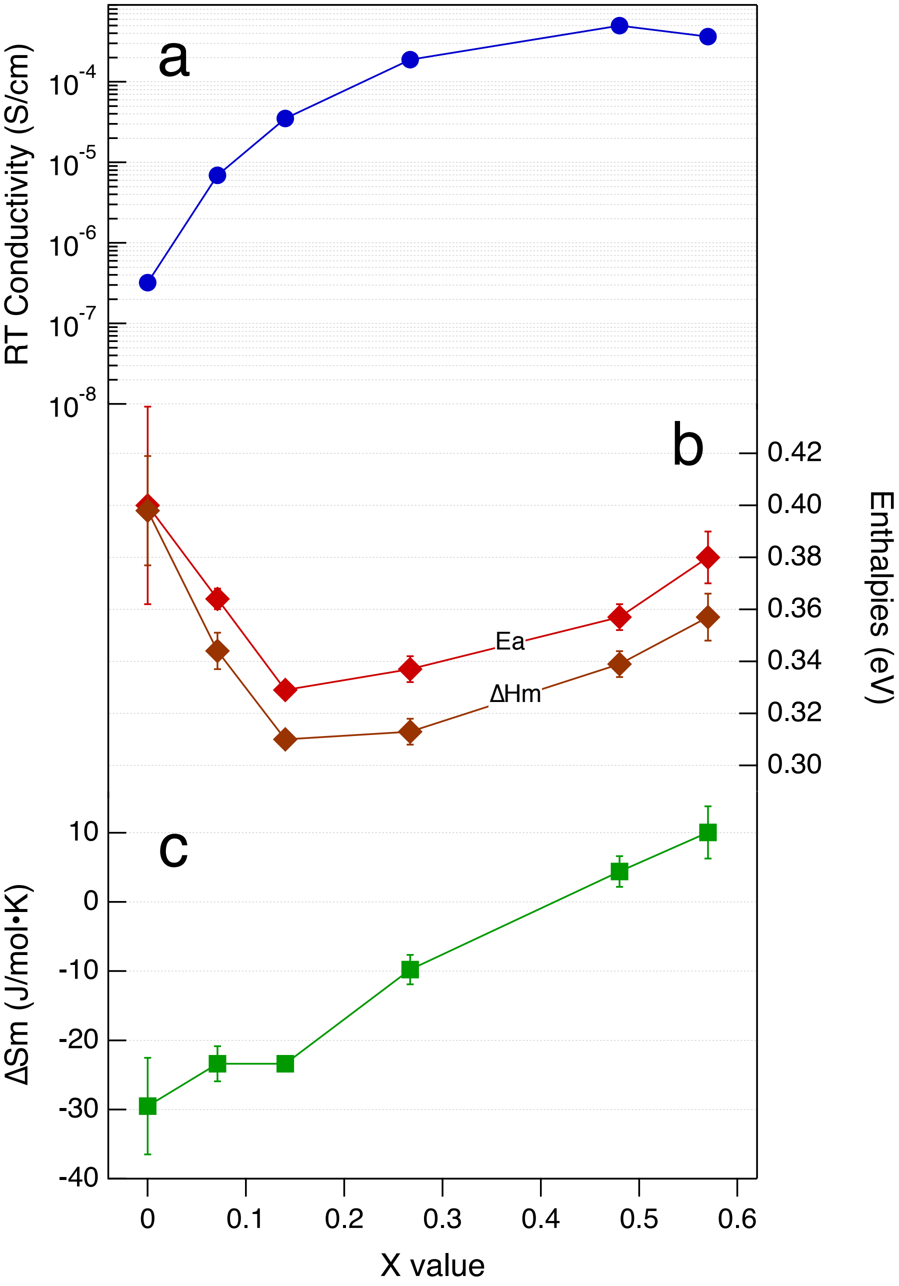

Figure 5.3: (a) Room temperature conductivity. (b) Activation energy (E_a) and enthalpy of ion motion (ΔH_m). (c) Entropy of ion motion (ΔS_m).

value increases, conductivity increases until X = 0.5, then appears to begin falling again. Typically, solid-state conductors are characterized by their conductivity and activation energy as shown in eq 5.1.

$$\sigma = \frac{\sigma_0}{T} \exp\left(\frac{-E_a}{kT}\right) \tag{5.1}$$

where σ is the conductivity, σ_0 is the exponential prefactor, E_a is the activation energy for ion conduction, k is the Boltzmann constant, T is the temperature in Kelvin. To thoughtfully design such a conductor, however, it is important to understand the various factors that contribute to E_a and σ. The value E_a represents an enthalpy for ion conduction; an energy required to move an ion long-range through the crystal. This value is a convolution of several other enthalpies, which have matching entropy contributions that are hidden in the exponential prefactor of eq 5.1 [16, 8]. These free energy terms are what comprise the thermal activation of the measured conductivity, and they result from the activation of charge carrier concentration and ion hopping rate. Activation of charge carrier concentration can be described as follows:

$$C = C_0 \exp\left(\frac{-\Delta G_c}{kT}\right) \tag{5.2}$$

$$C_0 = N n_c (1 - n_c) \tag{5.3}$$

where C is the concentration of mobile ions, C_0 is the concentration of potentially mobile ions, N is the concentration of energetically equivalent mobile-ion sites, n_c is the fraction of occupied mobile-ion sites, and ΔG_c is the free energy of charge carrier generation. The energy ΔG_c is a convolution of energies of charge carrier formation, trapping, and site occupancy: $\Delta G_c = \Delta G_f + \Delta G_t + \Delta G_g$. In this context, charge carrier formation represents a process similar to defect pair generation, whereby charge carriers are created where they did not exist previously. In fast ion conductors such as those in the NASICON family, all charge carriers are already formed, and $\Delta G_f = 0$. Charge carrier trapping can result in doped structures, where the coloumbic attraction and local elastic strain near the site of the dopant can lead to a sticking of the charge carrier. This phenomenon is typically observed in oxygen conductors where heterovalent doping introduces ions of large valence and size difference, causing the trapping of the oxygen charge carriers that they created. In NASICON materials where dopants are similar to the constituents they replace, such as the situation in this study, this type of trapping is likely negligible, and we can assume $\Delta H_t \approx 0$. The thermal activation of site occupancy can occur when there exists several types of mobile ion sites in the crystal that are not energy equivalent. Such is the case in NASICON materials when considering the M1 and M2 sites. This term represents a temperature dependence for $n_c^{M1} \rightarrow n_c^{M2}$. In the case of the NASICONs studied here, we hypothesize that this term is ultimately driven by the temperature dependence of the lattice constants; i.e., driven by thermal expansion in the lattice. As germanium-based NASICON materials are heated, they expand in the c-direction and contract in the a-direction [1]. When ions are occupying both M1 and M2 sites, the relative occupancies reflect a balance of electrostatic forces between Li-O attraction and Li-Li repulsion [7]. As the lattice dimensions change, Li-O and Li-Li distances will change as well, and the changing electrostatic equilibrium can lead to small changes in equilibrium site occupancies. Since the occupancy changes with temperature are small, the overall contribution of this term is also small.

The thermal activation of ion hopping rate can be represented as follows:

$$\nu = \nu_0 \exp\left(\frac{-\Delta G_m}{kT}\right) \tag{5.4}$$

$$\nu_0 = \sqrt{\frac{\Delta H_m}{2 m_{Li} d^2}} \tag{5.5}$$

where ν is the hopping rate of a mobile ion, also called the relaxation frequency of Li^+, ν_0 is the fundamental attempt frequency for ion hopping derived from the harmonic potential well expression [26], ΔH_m is the enthalpy of charge carrier motion, m_{Li} is the mass of a lithium cation, and ΔG_m is the free energy of ion motion. Rewriting eqs 5.2 and 5.4 and expanding the free energy terms ΔG_g and ΔG_m, we have:

$$C = C_0 \exp\left(\frac{\Delta S_g}{k}\right) \exp\left(\frac{-\Delta H_g}{kT}\right) \tag{5.6}$$

$$\nu = \nu_0 \exp\left(\frac{\Delta S_m}{k}\right) \exp\left(\frac{-\Delta H_m}{kT}\right) \tag{5.7}$$

In eq 5.6, the term ΔH_g may be understood as the energy required to reconfigure the mobile lithium population over energy inequivalent sites as the electrostatic interactions between ions change with thermal expansion in the structure [7]. The entropy term, ΔS_g, might be interpreted within the context of changing configurational potential as charge carriers are re-arranged.

In eq 5.7, the situation is slightly more complicated. There are several possible contributions to the enthalpy term, notably:

$$\Delta H_m = \Delta H_h + \Delta H_r + \Delta H_{cm} \tag{5.8}$$

where ΔH_h is the energy required to hop through the constrictive bottleneck point, ΔH_r is the energy required to make up the potential difference between starting and ending lattice sites, and ΔH_{cm} is an energy required for correlated ion motion in materials where n_c is large. The term ΔH_h exists in every ion conductor to varying degrees depending primarily on the configuration of the conduction pathways and the bottleneck points. If every mobile ion site in the structure is equivalent in terms of coordination and chemical surroundings, then ΔH_r may be small, resulting only from the fact that an occupied site has a slightly lower energy than an empty site. If an ion hops between sites that are not equivalent, then this term may be significant. Correlated ion motion results from clustering of mobile ions within the structure. When n_c becomes large and ions are fighting for vacant sites to pass through, certain structures (such as β-alumina) allow clustering of charge carriers, where the cooperative motion helps each ion move in the short range. However, there is a small energy penalty to move the larger cluster, and this is the source of the term ΔH_{cm}. The entropy term, ΔS_m, to this point, has not been well studied and is not well understood. This term will be discussed later within the context of the configuration of the lithium population. Now, we can build these derivations into a detailed relationship for conductivity:

$$\sigma = \left(\frac{fx\alpha z^2 d^2 N n_c(1 - n_c)\nu_0 \exp\left(\frac{\Delta S_m + \Delta S_g}{k}\right)}{kT} \right) \exp\left(\frac{-(\Delta H_m + \Delta H_g)}{kT} \right) \tag{5.9}$$

where f, x, and α are geometric factors related to jump path, mobile site coordination number, and dimensionality of conduction pathways, z is the charge on a carrier, and d is the jump distance from one mobile ion site to the next. Since f, x, α, z, and N are composition-independent, depending only the general structure, they can be ignored in this analysis. All other values in eq 5.9 vary with composition.

We can see from eq 5.9 that in our NASICON system, $E_a = \Delta H_m + \Delta H_g$. Considering eq 5.1, measurement of the temperature dependence of conductivity allows determination of the parameter E_a. These results are presented in Figure 5.3b. With an understanding that ΔH_m comes from the temperature dependence of ion hopping rate (eq 5.7), and ion hopping rate is the physical manifestation of the relaxation frequency, it was possible to probe this value analytically, knowing:

$$\nu = \omega_0 = \frac{1}{RC} \tag{5.10}$$

$$C = Q\omega_0^{n-1} = (QR^{1-n})^{1/n} \tag{5.11}$$

where R is the bulk resistance from the sample, C is the ideal capacitance of the sample, and Q and n have been previously defined. Using the fitted values of R, Q, and n from the bulk impedance response such as shown in Figure 5.2, we calculated the ion-hopping rate at each temperature. These results are presented in Figure 5.4.

The trendline of a linear fit to this data provides ΔH_m, and the intercept at $T = \infty$ is related to ΔS_m. It is in this way that we have produced the results for ΔH_m and ΔS_m shown in Figure 5.3b and 5.3c. The parameter ΔS_m has not been well studied and is not well understood, but we will discuss the results in Figure 5.3c with regard to the distribution of Li^+ within the structure

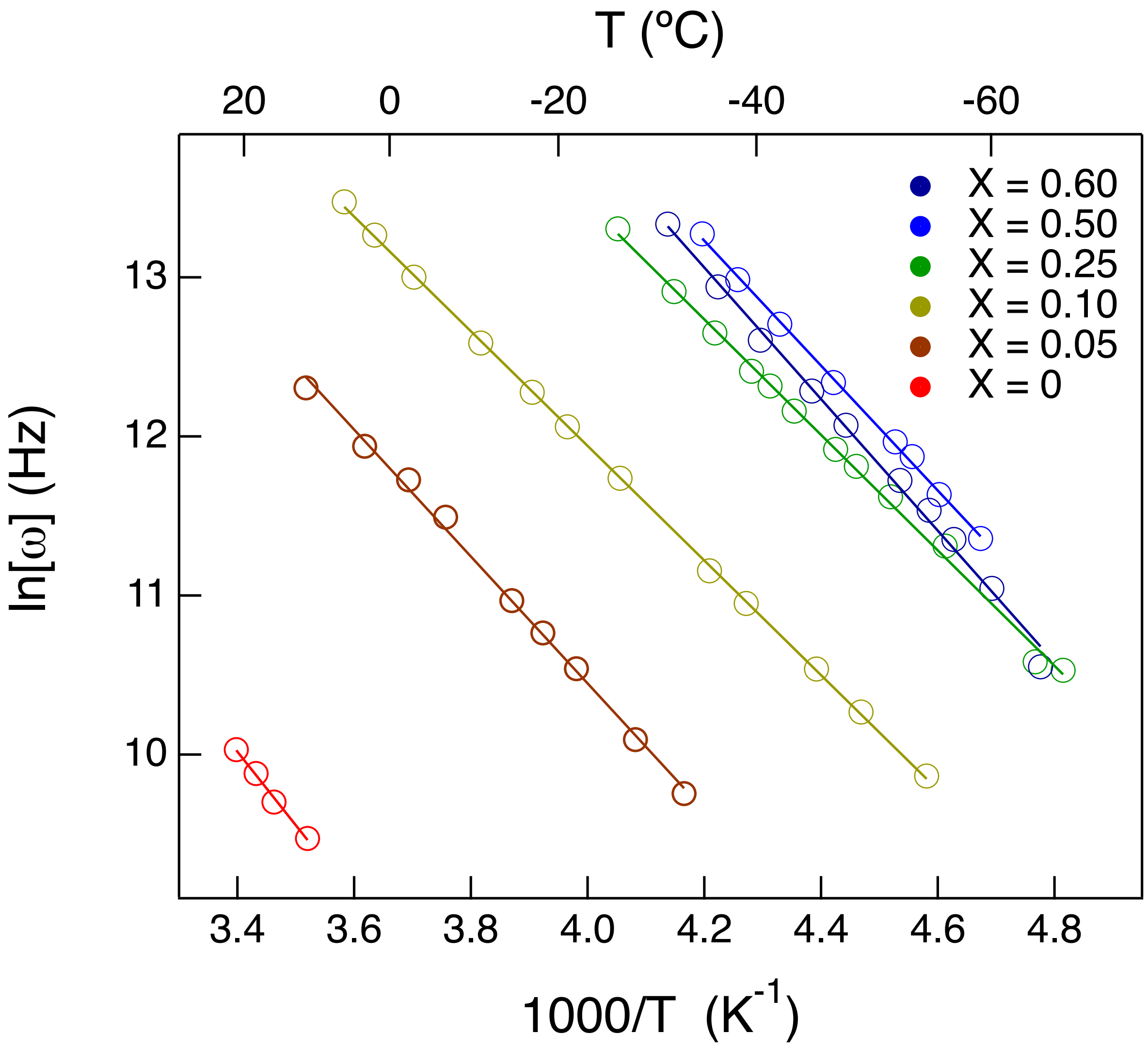

Figure 5.4: Arrhenius plot of hopping rate for all materials evaluated.

later.

In Figure 5.3b we observe that ΔH_m essentially tracks with E_a, and for all compositions except X = 0, there appears to be a small, constant difference between these two values. This would indicate that ΔH_m is the dominant contributor to E_a, and ΔH_g is small and unchanging with composition. For X > 0 we estimate $\Delta H_g = 0.04$ eV, which generally agrees with prior work [3]. Previously, this value has been attributed to an extra energy required to form vacancies on M1 sites. We interpret this changing site occupancy as being driven by changing electrostatic equilibrium with thermal expansion/contraction in the structure. In this context, with similar structures and chemistries leading to similar expansivities, it would make sense that ΔH_g would be nearly constant across the compositions studied here.

5.4.2 Crystal Structure

In order to perform an accurate analysis of the structure of each material, synchrotron powder x-ray diffraction was carried out at beamline 11-BM at the Advanced Photon Source. This instrument offers superb resolution and sensitivity, which was necessary to resolve the minute structural details of each composition. Figure 5.5 shows each diffraction pattern in the range 2-15° 2-theta (λ = 0.4138Å).

Of note is the flat baselines and sharp peaks which indicate good crystallinity, and lack of obvious impurity phases. A Rietveld refinement was carried out on each pattern with the ultimate goal of reaching an estimate for the occupancy of the M1 lithium site. During refinement, the X value of each material, as defined by the relative amounts of Al and Ge in the structure, was allowed to vary while maintaining full occupancy of this 12c site. Lithium occupancy of site M1 was assumed to be 1.0 at the start of refinements, with the remaining Li, as required by the composition, placed on site M2. These values were fixed until background, profile, lattice, and structural models had converged, at which point M1 occupancy was freely varied. Figure 5.6 provides a visual of a refined pattern, and a summary of results is presented in Table 5.1.

Listed in Table 5.1 are nominal X values as well as refined X values. The nominal values

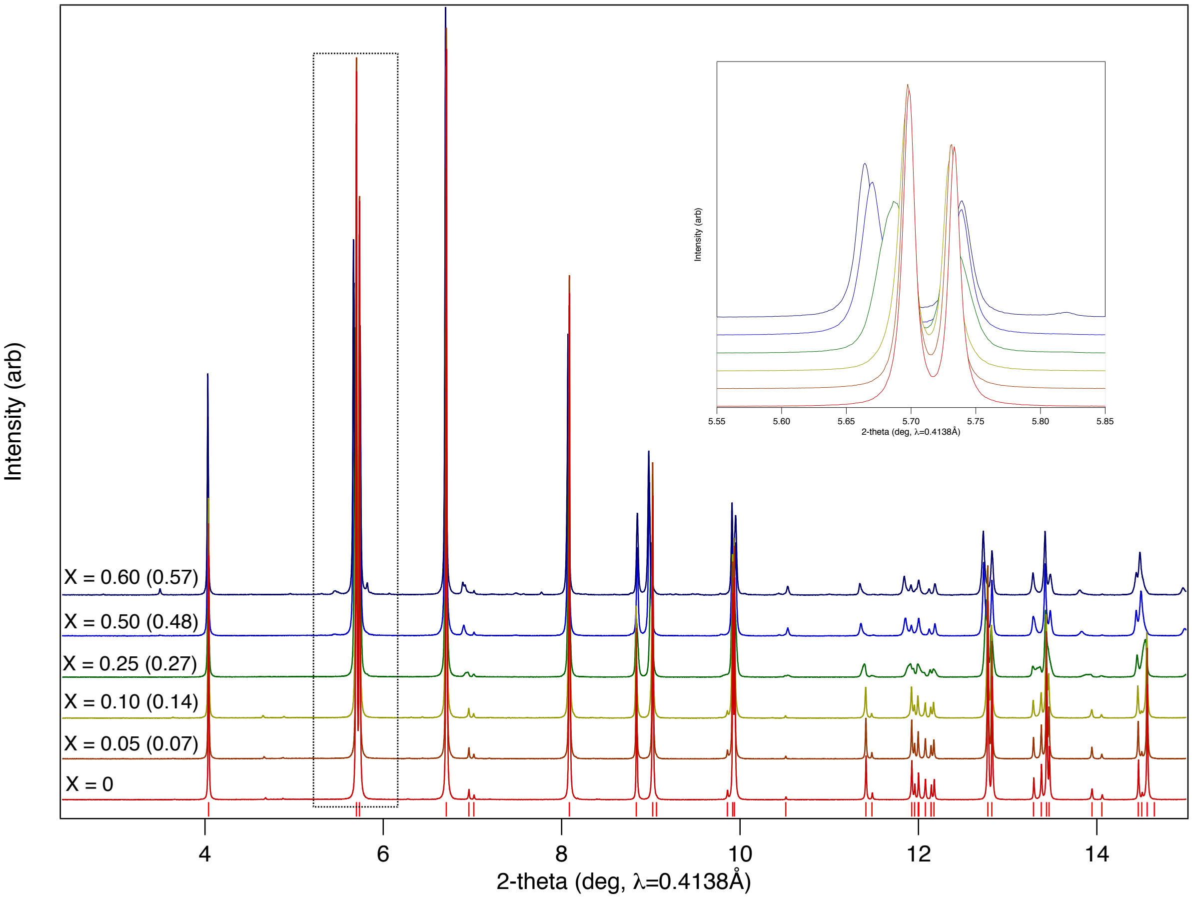

Figure 5.5: Synchrotron powder XRD patterns of all materials in this study. Nominal composition is labeled on the baseline of each pattern, with refined composition in parenthesis. The inset shows a close up view of the boxed region of the patterns, highlighting the slight lattice changes with composition.

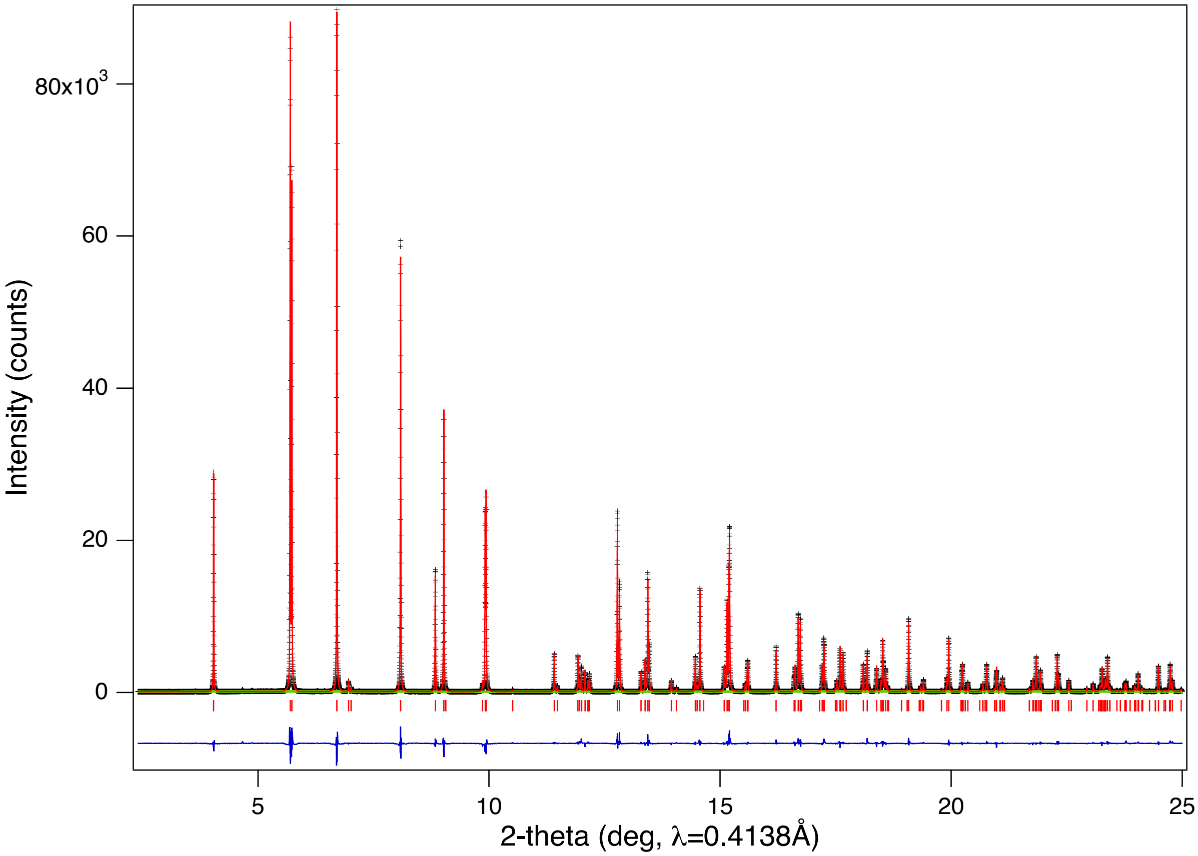

Figure 5.6: Rietveld refinement of composition X = 0.05. Shown is observed intensity (crosses), calculated intensity (red line), baseline (green line), reflection positions (tick marks), and I_{obs}-I_{calc} difference pattern (blue line).

Table 5.1: Structural data derived from Rietveld refinement of synchrotron powder x-ray diffraction data

Nominal	Refined	a	c	cell volume	density	hop distance	$M1_{occ}$	c/a ratio	Fitting Results		
X value	X value	Å	Å	Å^3	g/cm^3	Å	%	-	wRp%	RF^2%	χ^2
0	0	8.273989(7)	20.45422(2)	1212.672(2)	3.590	3.1828	1.000	2.472	9.27	5.92	4.28
0.05	0.07	8.272968(6)	20.45439(2)	1213.560(2)	3.565	3.1836	1.000	2.472	8.10	6.20	3.29
0.10	0.14	8.27895(1)	20.45914(4)	1214.420(4)	3.541	3.1844	0.979	2.471	10.84	7.56	5.96
0.25	0.27	8.27236(3)	20.5269(1)	1216.502(7)	3.497	3.1856	0.940	2.481	6.98	5.78	2.56
0.50	0.48	8.26590(2)	20.61554(9)	1219.849(7)	3.411	3.1878	0.714	2.494	9.96	7.08	5.44
0.60	0.57	8.26510(3)	20.6374(1)	1220.90(1)	3.388	3.1886	0.668	2.497	12.66	12.84	8.81

are those targeted during synthesis, and the refined values are those determined from refinement of the Al/Ge ratio. It is not unexpected that these values are slightly different. In the discussion of results, we will make reference to nominal X values as these numbers are cleaner, but all analysis was carried out in reference to the refined X values.

Worth noting is that for composition X = 0.25, the diffraction pattern was best fit with two NASICON phases with slightly different Al/Ge ratios and lattice constants. Figure 5.7 shows that this two-phase model fits the data well, and the inset highlights the contribution from each phase in a pronounced region of the pattern. Based on the similarity in chemistry and lattice dimensions of each phase, it may be reasonable to say that a single phase was initially formed during synthesis, which subsequently separated into two similar phases during the prolonged calcination at 800°C. At present, an explanation for this unexpected result cannot be given. One of the many benefits of Rietveld analysis is that the weight fractions of each phase contributing to the calculated pattern are estimated during refinement. In Table 5.1, the weighted average of values from each phase is presented. Despite the apparent phase separation, the weighted average values fall within the established trend in the data, and the overall analysis is considered valid.

As lithium atoms are weak scatterers of x-rays, powerful and sensitive synchrotron diffraction

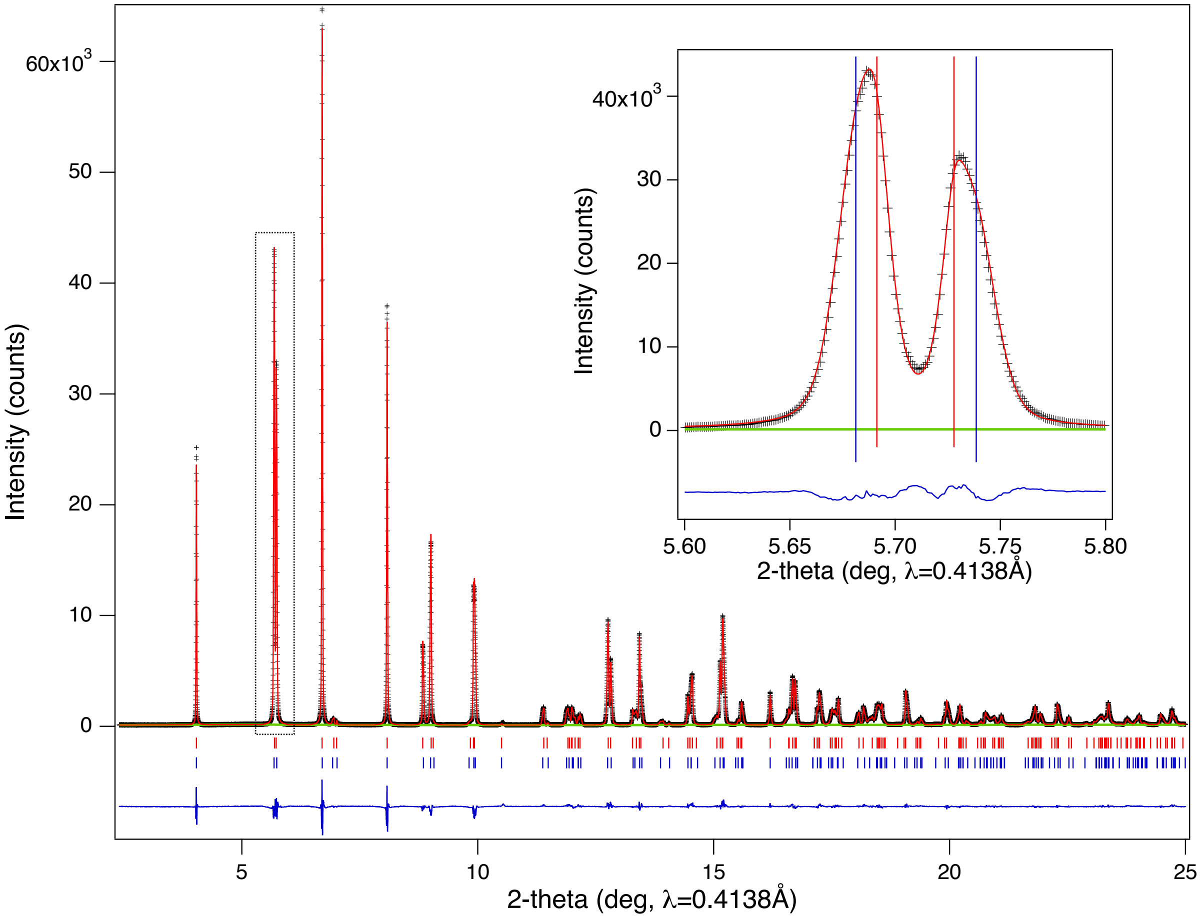

Figure 5.7: Rietveld refinement of composition X = 0.25. Shown is observed intensity (crosses), calculated intensity (red line), baseline (green line), reflection positions (tick marks), and I_{obs}-I_{calc} difference pattern (blue line). The inset highlights the contributions from each phase to the overall pattern.

measurements are the best way to analyze structures containing lithium. Nevertheless, measurements of a parameter as delicate as the occupancy factors of lithium sites may contain inaccuracies up to 10% [19]. In order to add confidence to values of M1 site occupancy obtained directly from Rietveld refinements, we can also infer this parameter from crystal dimensions. Shown in Figure 5.8 is the variation of M1 occupancy and c/a axis ratio with composition.

Earlier work has demonstrated that as Li^+ occupancy shifts from M1 to M2 sites, the structure expands in the c-direction and contracts in the a-direction [2, 7]., This is driven by electrostatic Li-O attractions at each lattice site. As Li^+ leaves site M1, the attractive force of the Li^+ on surrounding oxygen atoms of MO_6 groups vanishes, and the resulting repulsive force between these groups works to expand the c-axis [9]. Simultaneously, new Li-O interactions are formed in site M2, and with the closest oxygen atoms lying in the a-b plane, M2 site occupancy acts to shrink the a-axis. Therefore, the M1/M2 occupancy ratio can be correlated to the c/a ratio for a given material. As both the accuracy and precision of lattice constant estimations from synchrotron data analysis are very high, values of c/a ratio can be considered accurate and the relationship with M1 occupancy is meaningful. In Figure 5.8 we observe the expected trend of c/a ratio increasing as M1 occupancy decreases. This indicates that as the X value increases, the occupancy of the M1 site decreases [7, 9]. An important point to make here is that this measurement reflects site occupancies of the material while in a state of rest; i.e., while there is no applied electric field. The importance of this point will be come clear while discussing results for ΔS_m. Observed in Figure 5.8 is that M1 occupancy and c/a ratio remain basically unchanged up to $X = 0.10$. This would indicate that the additional Li^+ brought into the structure with increasing X value is placed in an M2 site, while the M1 site remains near full occupancy. For $X > 0.10$, the addition of Li^+ creates sufficient Li-Li repulsive force to reconfigure the population over M1 and M2 in such a way that vacancies are introduced at site M1. This trend is observed to continue up to $X = 0.60$.

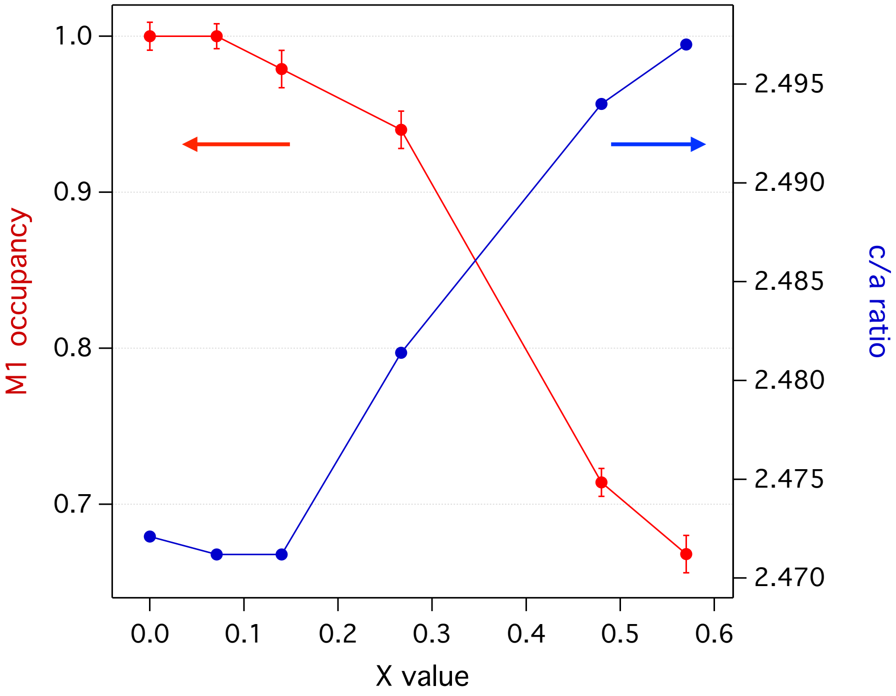

Figure 5.8: The relationship between M1 site occupancy, c/a- axis ratio, and crystal composition.

5.4.3 Local Structure and Bonding

To support discussion of crystal structural and the energetics of ion motion, a study of the local structural order and bonding was carried out using Raman spectroscopy. In phosphate compounds like those in the NASICON family, the Raman response results primarily from excitation of vibrations of the PO_4 structural group [4]. In the NASICON structure, The PO_4 group provides a link between MO_6 octahedra, sharing oxygen atoms with the Al^{3+}/Ge^{4+} and Li^+ ions in the structure. Factor group analysis of these compounds with space group $R\bar{3}c$ dictates 14 Raman active vibrational modes: 6 stretching modes and 8 bending modes for the PO_4 structural unit [25]. Figure 5.9 displays Raman spectra recorded in the range 200-1300 cm^{-1} for each material, with the groupings of bending and stretching modes labeled.

In general, we observe that peak broadness increases with X value. There are two likely explanations for this observed broadening trend. The first source of broadening may come from Al^{3+} replacing Ge^{4+} in the structure. While the ionic radii of Al^{3+} and Ge^{4+} may be similar, their ability to draw electron density from an octahedral cage of oxygen ions is not. The effectiveness of an ion at drawing electron density towards itself is roughly proportional to: (charge on the ion) / (ionic radius) [23]. Therefore, when Al^{3+} is substituted for Ge^{4+} in an MO_6 unit, there will be a change is charge distribution throughout the unit. Since oxygen atoms are shared between MO_6 and PO_4 units, there will be a concomitant change in charge distribution, and therefore bond character, in the adjacent PO_4 unit. This change in bond character will manifest as a shift in peak location in the Raman spectrum. If the Al substitution rate is low, only a small portion of total P-O bonds are affected, and the measured peak broadening will be small. As the Al/Ge ratio increases, it can be expected that observed peak broadening will become more severe. The second source of broadening is related to the distribution of lithium ions in the crystal. At $X = 0$ all Li^+ are in an M1 site, directly between two MO_6 units stacked along the c-axis [1]. However, above this X value, it is necessary that some amount of Li^+ is in an M2 site. When a Li^+ occupies an M2 site, there are new Li-O bonds created. This new and changing bonding will necessarily affect P-O

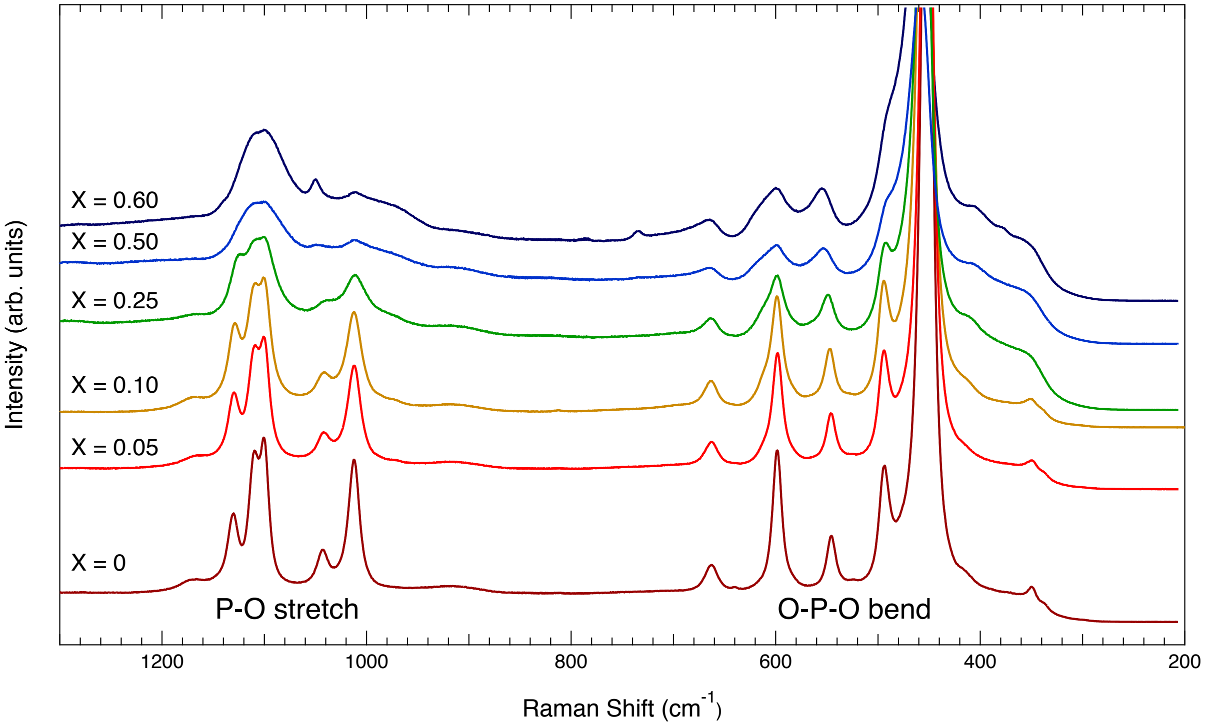

Figure 5.9: Raman spectra recorded in the range 200 - 1300 cm^{-1}

bonding, and will likely have a similar broadening effect on peaks due to PO_4 vibration [5]. It is likely that both of these effects are observed in Figure 5.9 with varying composition.

5.5 Discussion

5.5.1 Enthalpic Contributions to Conductivity

In evaluating the conductivity in this NASICON family, let us first focus on the activation enthalpy. As shown in Figure 5.3b, for composition $X = 0$, E_a and ΔH_m are, within error, the same. This indicates that any ΔH_g is negligible, and the only enthalpy contribution to the activation energy comes from the energy required for ion movement. The fact that there is no obvious contribution from ΔH_g can be explained by the absence of a driving force for carrier reconfiguration. At $X = 0$, there is exactly enough lithium in each unit cell to fill all M1 sites, and prior work has shown that this composition exists with M1 sites filled and M2 sites completely vacant [1]. Our own XRD data shown in Figure 5.8 supports this as well. Therefore, there are no Li^+ in M2 sites putting pressure on Li^+ in M1 sites to move, so even as the structure expands thermally, there is no need (i.e. no driving force) for reconfiguration and $\Delta H_g \cong 0$.

For $X = 0$, the lowest conductivity, highest E_a, and highest ΔH_m are measured. Since $E_a = \Delta H_m$, the terms of eq 5.8 are called into question. With M1 full and M2 empty, the energy difference between these sites is maximized, and ΔH_r in eq 5.8 is maximized. What can be considered a baseline value of ΔH_h is established with $X = 0$, and this of course also contributes to ΔH_m. This composition has the least amount of Li^+ of all compositions studied, and correlated ion motion should be insignificant: $\Delta H_{cm} \approx 0$. In fact, this term is likely insignificant in all materials, as the highest n_c of 0.4 at $X = 0.60$ is still not very high. An important consequence of having the lowest amount of Li^+ is that the term $n_c(1-n_c)$ in eq 5.3 is at its minimum. These factors all convolve and contribute to the lowest observed conductivity by 1.5 decades at $X = 0$.

With the increase in Al and Li to $X=0.05$, there is a dramatic increase in conductivity and a decrease in both E_a and ΔH_m, as seen in Figure 5.3a-b. The decrease in ΔH_m likely occurs in large part because of Li^+ beginning to populate M2 sites. Now, with more Li^+ than there are M1 sites, it is necessary that the additional Li^+ begin populating M2 sites. Indeed, x-ray data suggests full M1 occupancy, so the additional Li^+ should take up residence on M2 sites. With this small amount of additional Li^+ the driving force to move Li^+ off of M1 is low, and the system finds an energy minimum while maintaining full M1 occupancy (at room temperature). With $X = 0.05$, we now notice that $E_a \neq \Delta H_m$, meaning that there is a contribution from ΔH_g. With Li^+ clearly now occupying some fraction of M2 sites, there exists a driving force for population reconfiguration. Although at room temperature this force is too low to cause significant change in M1 occupancy, as the structure expands at elevated temperatures, occupancy change in likely. We see from Figure 5.3a that conductivity has increased nearly 1.5 orders of magnitude compared with $X = 0$. This is a direct result of the dramatic decrease in ΔH_m and increase in number of charge carriers.

Examining the incremental change in composition to $X = 0.1$, we see a continuation of the trend of decreasing ΔH_m and increasing conductivity. A similar rationale as with $X = 0.05$ applies here. X-ray refinements of M1 occupancy suggest that the additional Li^+ may cause some reconfiguration of the mobile ion population and vacancies to develop on M1 sites, but there is no obvious change in c/a ratio. As there will be some inherent error in the refined M1 occupancy value, it may be reasonable to conclude that M1 sites remain essentially filled in this composition. Again, $E_a \neq \Delta H_m$, and the value of ΔH_g is similar to that observed previously. Looking at this value over the remaining range of composition variation, we notice that it is essentially unchanging. In this study we are considering materials with similar structures and chemistries, so it is likely that the thermal expansion coefficients of each material will be similar. As the physical significance of ΔH_g derives from the thermal expansion of the structure, it is reasonable that it would remain essentially unchanged in all compositions with M1 and M2 occupancy.

With a further increase in Al and Li content to $X = 0.25$, we see new trends develop in ΔH_m and conductivity. Conductivity has increased relative to $X = 0.10$, but the rate of increase with X value has slowed. The enthalpy of ion motion, ΔH_m, has reversed its trend of decreasing with X value, and in fact increases slightly from $X = 0.10$. We again examine the contributions to ΔH_m, namely ΔH_h and ΔH_r. As before, the additional Li^+ must contribute to a lower ΔH_r. In this case, we observe in XRD data a decrease in M1 occupancy and an increase in c/a ratio. These observations indicate that with this increment in Li^+ content, electrostatic Li-Li repulsions are now large enough to cause significant reconfiguration of the mobile ion population across M1 and M2 sites. Now, the Li^+ population finds equilibrium with 94% of M1 sites occupied. Since ΔH_m has increased overall, ΔH_h must have increased from X = 0.10 to X = 0.25. This can be rationalized when considering that Al^{3+} and Ge^{4+} do not draw electron density from oxygen atoms equally. The effectiveness of an ion to pull electron density from bound ions towards itself is proportional to charge/radius. Al^{3+} and Ge^{4+} have similar ionic radii, but obviously different charges. The consequence is that an MO_6 unit formed with Al will leave more electron density around each oxygen atom, leaving more electron density in the conduction pathway, which has the effect of shrinking the conduction bottleneck window. A smaller bottleneck window makes it harder for a Li^+ to hop through, leading to a direct increase in ΔH_h. Evidence for this explanation can be seen in the broadening of Raman peaks in Figure 5.9. Overall, the increase in ΔH_h and decrease in ΔH_r nearly balance, and the result is only a slight increase in ΔH_m. For X = 0.25, the conductivity increase is mainly driven by the increase in number of charge carriers.

With a composition increment to X = 0.50, the trend of increasing ΔH_m and conductivity continues. ΔH_h likely continues to increase, as the Al^{3+} substitution continues to shrink the average bottleneck size in the crystal. Here we observe the highest conductivity, indicating that this composition represents a balance point between increasing enthalpy restrictions and increasing charge carrier concentration. This composition is often reported as the best conductor in the $Li_{1+x}Al_xGe_{2-x}(PO_4)_3$ family. As composition is incremented to X = 0.60, ΔH_m again increases and conductivity now decreases slightly. With this composition, enthalpic contributions are now the biggest factor determining conductivity.

5.5.2 Entropy of Motion

We would now like to turn our attention to the entropy of motion factor, ΔS_m. Variation of ΔS_m with X value is shown in Figure 5.3c. In general, we observe an increase in ΔS_m with X value. At $X = 0$ ΔS_m is negative, and at a point around $X = 0.4$, ΔS_m changes sign and becomes positive.

Until now there have not been any substantial theories for what this term might represent physically in crystalline conductors such as those in the NASICON family studied here. In a previous report we proposed a theory which relates ΔS_m to the configuration of the Li^+ population across M1 and M2 sites, and here we present further data to support that idea. Shown in Figure 5.10 is variation of c/a ratio and M1 occupancy with X value alongside variation in ΔS_m with X value.

What we see in Figure 5.10a is that ΔS_m essentially tracks with c/a ratio, and in Figure 5.10b ΔS_m seems to vary inversely with M1 occupancy. This implies a correlation between the observed ΔS_m and occupancy of the M1 site. Looking closely at the structure of a NASICON conductor (shown in Figure 5.1), we see that each M1 site is surrounded by six M2 sites, and each M2 site is surrounded by only two M1 sites. If a Li^+ was on an M1 site and made a single hop, it has six options. For a Li^+ sitting on an M2 site looking to make a single hop, there are two possible options. In this way, the Li^+ on the M1 site has a higher configurational potential than the Li^+ on the M2 site. Consider now an entire population of Li^+ spread across these sites, where the overall configurational potential is derived from a sort of weighted average of the M1-M2 distribution. Since we cannot measure the configurational potential (entropy of motion, S_m) directly, we must measure a change in this potential relative to some reference points. Within our framework of activated ion motion, we have considered ΔG with respect to the activated state and the rest state. Experimentally, the activated state is one in which energy is supplied by a time-varying electrical field such that all potential barriers ΔH can be overcome and the lithium population is set in motion, reaching steady state long-range hopping. The rest state is that where no external

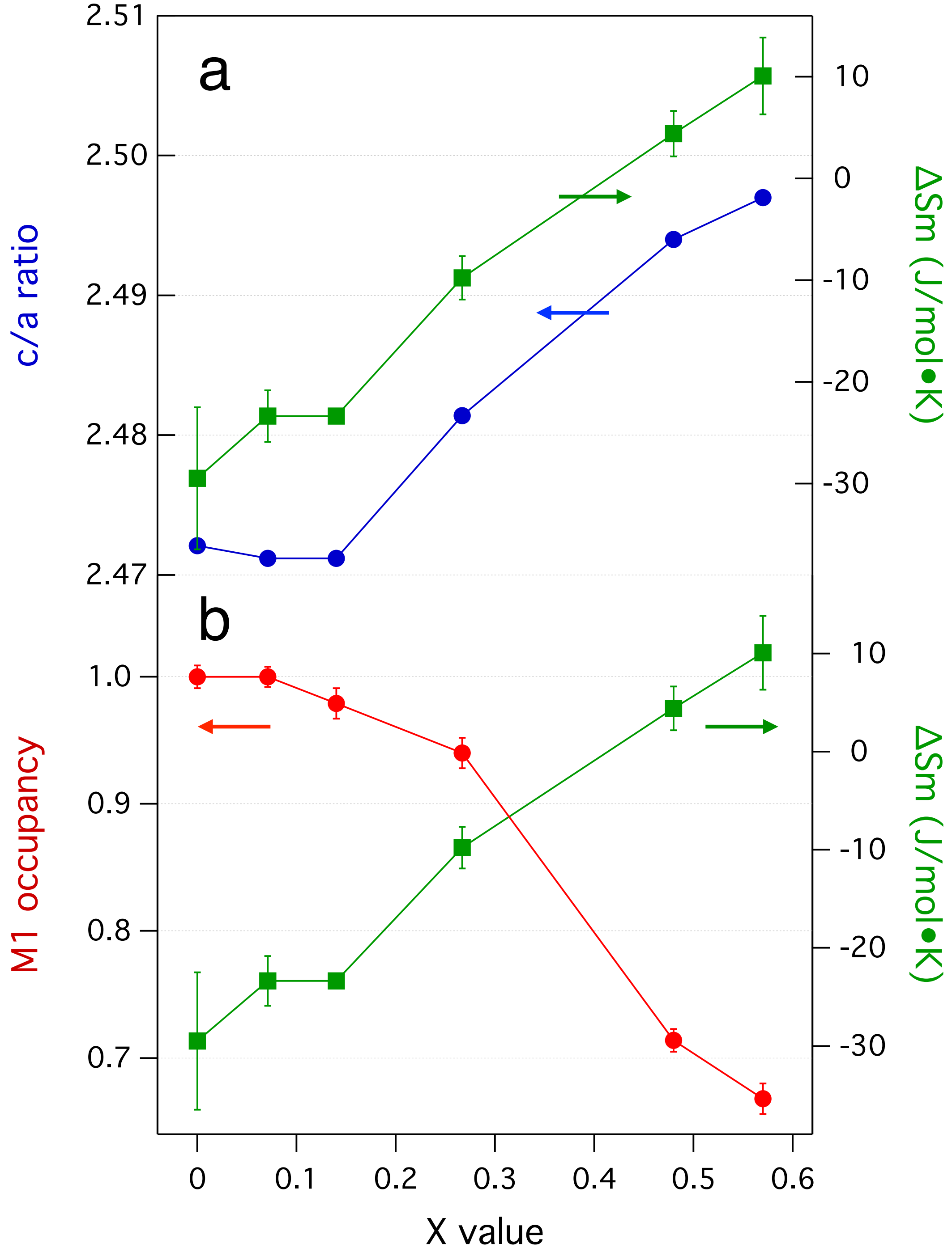

Figure 5.10: (a) Variation of c/a axis ratio and ΔS_m with X value. (b) Variation of M1 occupancy and ΔS_m with X value.

perturbations are applied, and a different equilibrium condition is met. Thus, we define: ΔS_m = [activated equilibrium] - [rest equilibrium]. In terms of configurational potential, the main focus of each equilibrium state is how the Li^+ population is configured across M1 and M2 sites.

As a starting point, consider the composition X = 0. At rest, as determined by XRD analysis, M1 sites are completely occupied and M2 sites are completely vacant. When this population is activated and long-range conduction reaches equilibrium, it is necessary that at any point in time a portion of the Li^+ population would be found at an M2 site. Since some portion of the Li^+ population can now be found on an M2 site, and M2 sites have a lower configurational potential than M1 sites, it clear that this system had a higher configurational potential in the rest state than in the activated state, and ΔS_m will be negative.

At the other end of the composition spectrum at X = 0.60, we see that ΔS_m is positive. Here, XRD data shows that Li-Li repulsions dictate a rest state M1 occupancy of 67%. When this Li^+ population is activated and long-range hopping begins, it is reasonable to deduce that this M1 occupancy must reach a steady state (time averaged) value >67%. This makes sense if we consider that every M1 site serves as a junction to three conduction pathways and would likely spend a greater fraction of time occupied by a passing ion. Having a higher M1 occupancy means having a higher configurational potential, so for this material we can understand why ΔS_m would be positive.

Somewhere around X = 0.4 we observe that ΔS_m crosses zero and changes sign. What we postulate is that at this composition, there is no appreciable difference between activated and rest state site occupancies. This would suggest that during steady-state long-range hopping in $Li_{1+x}Al_xGe_{2-x}(PO_4)_3$, M1 sites remain approximately 80% full. This information can be used to further rationalize the trends observed in Figure 5.10. For X = 0, 0.05, and 0.10, M1 occupancy is ~100% at rest and variation in ΔS_m is minimal within experimental error. With X = 0.25 it is clear that at rest M1 occupancy is 80% < M1occ < 100%. So, when this composition is activated, additional Li^+ are displaced from M1 sites to reach 80% occupancy, and the configurational potential of the system as a whole drops; the result is a smaller but still negative ΔS_m. For X =

0.50, rest state M1 occupancy is estimated at 71%. When this Li^+ population is activated, M1 occupancy increases slightly to 80%, and the configurational potential of the system as a whole increases slightly; the result is a small but positive ΔS_m.

It may be reasonable to say that for $X < 0.4$, entropy hinders conduction, and for $X > 0.4$, entropy favors conduction. Clearly, there is a link between this thermodynamic parameter and composition, as with ΔH_m, and both play a role in the observed conductivity. The role played by entropy, however, is small compared to the role played by enthalpy. At room temperature, entropy terms represent ≤ 22% of the energy contribution of enthalpy terms. While not insignificant, it is clear that in designing NASICON systems, more focus should be put on tailoring the enthalpy of motion as opposed to the entropy of motion.

5.6 Conclusions

In this work we synthesize NASICON-type solid solutions with nominal compositions $Li_{1+x}Al_xGe_{2-x}(PO_4)_3$ where $0 \leq X \leq 0.6$, and evaluate the various energetic factors contributing to observed values of room temperature conductivity. While simple conduction theory would predict a maximum conductivity when Li^+ sites are exactly half filled at $X = 1$, we observe a maximum near $X = 0.5$. With the help of a thorough structural analysis we conclude that initial drops in activation energy are driven by a growing Li^+ population on M2 sites, while later increases in activation energy are driven by changes in average bottleneck size caused by the Al-for-Ge substitution. Values of the entropy of motion are rationalized by considering the changing configurational potential of the mobile Li^+ population with changes in X value. In general: composition determines the amount of Li^+ in the structure, a complex electrostatic force balance determines M1 and M2 site occupancies, and site occupancy determines whether conduction is entropically favored or entropically hindered. We observe that entropy contributions only begin to enhance conductivity above $X = 0.4$, and they are mostly negated by increases in enthalpy. Over all compositions, entropic contributions to free energy of activation amount to ≤ 22% of enthalpy contributions at room temperature. These insights suggest that while entropic contributions are not insignificant, more attention should be paid to lowering activation energy when designing a new NASICON-type conductor.

References

[1] M Alami, R Brochu, J L Soubeyroux, P Gravereau, G Le Flem, and P Hagenmuller. Structure and thermal expansion of $LiGe_2(PO_4)_3$. Journal of Solid State Chemistry, 90(2):185–193, February 1991.

[2] James Alamo and Rustum Roy. Crystal chemistry of the $NaZr_2(PO_4)_3$, NZP or CTP, structure family. Journal of Materials Science, 21(2):444–450, February 1986.

[3] K Arbi, M Tabellout, M Lazarraga, J Rojo, and J Sanz. Non-Arrhenius conductivity in the fast lithium conductor $Li_{1.2}Ti_{1.8}Al_{0.2}(PO_4)_3$: A Li7 NMR and electric impedance study. Physical Review B, 72(9):094302, September 2005.

[4] M Barj, G Lucazeau, and C Delmas. Raman and infrared spectra of some chromium Nasicon-type materials: Short-range disorder characterization. Journal of Solid State Chemistry, 100(1):141–150, September 1992.

[5] M Barj, H Perthuis, and P Colomban. Relations between sublattice disorder, phase transitions and conductivity in NASICON. Solid State Ionics, 9-10:845–850, December 1983.

[6] Evgenij Barsoukov and James Ross Macdonald. Impedance Spectroscopy. Theory, Experiment, and Applications. John Wiley & Sons, New Jersey, 2 edition, 2005.

[7] J P Boilot, G Collin, and P Colomban. Relation Structure Fast Ion Conduction in the Nasicon Solid-Solution. Journal of Solid State Chemistry, 73(1):160–171, March 1988.

[8] Peter G Bruce. Solid State Electrochemistry. Cambridge University Press, New York, 1 edition, June 1997.

[9] M Cretin and P Fabry. Comparative study of lithium ion conductors in the system $Li_{1+x}Al_xA_{2x}{}^{IV}$ $(PO_4)_3$ with A^{IV}=Ti or Ge and 0x07 for use as Li^+ sensitive membranes. Journal Of The European Ceramic Society, 19(16):2931–2940, December 1999.

[10] Gaelle Delaizir, Virginie Viallet, Abdelmaula Aboulaich, Renaud Bouchet, Laurence Tortet, Vincent Seznec, Mathieu Morcrette, Jean-Marie Tarascon, Patrick Rozier, and Mickael Dollé. The Stone Age Revisited: Building a Monolithic Inorganic Lithium-Ion Battery. Advanced Functional Materials, 22(10):2140–2147, February 2012.

[11] Adolfo Delgado, Mario F García-Sánchez, Jean-Claude M'Peko, A Rabdel Ruiz-Salvador, Geonel Rodríguez-Gattorno, Yuri Echevarría, and Froilan Fernández-Gutierrez. An Elementary Picture of Dielectric Spectroscopy in Solids: Physical Basis. Journal Of Chemical Education, 80(9):1062, September 2003.

[12] Jinkui Feng, Hui Xia, Man On Lai, and Li Lu. NASICON-Structured $LiGe_2(PO_4)_3$with Improved Cyclability for High-Performance Lithium Batteries. Journal Of Physical Chemistry C, 113(47):20514–20520, November 2009.

[13] J G Fletcher, A R West, and J T S Irvine. The Ac-Impedance Response of the Physical Interface Between Yttria-Stabilized Zirconia and $YBa_2Cu_3O_{7-X}$. Journal of The Electrochemical Society, 142(8):2650–2654, August 1995.

[14] Brian E Francisco, Conrad R Stoldt, and Jean-Claude M'Peko. Lithium-Ion Trapping from Local Structural Distortions in Sodium Super Ionic Conductor (NASICON) Electrolytes. Chemistry of Materials, 26(16):4741–4749, August 2014.

[15] HY-P Hong. Crystal structures and crystal chemistry in the system $Na_{1+x}Zr_2Si_xP_{3x}O_{12}$. Materials Research Bulletin, 11(2):173–182, 1976.

[16] Robert Huggins. Advanced Batteries. Materials Science Aspects. Springer, New York, 1 edition, November 2008.

[17] S Li. Phase relationships and electrical conductivity of $Li_{1+x}Ge_{2-x}Al_xP_3O_{12}$ and $Li_{1+x}Ge_{2-x}Cr_xP_3O_{12}$ systems. Solid State Ionics, 28-30:1265–1270, September 1988.

[18] Enrique R Losilla, Miguel A G Aranda, Sebastián Bruque, Miguel A París, Jesús Sanz, and Anthony R West. Understanding Na Mobility in NASICON Materials: A Rietveld, 23Na and 31P MAS NMR, and Impedance Study. Chemistry of Materials, 10(2):665–673, February 1998.

[19] D Ingersoll D H Doughty M A Rodriguez. RIETVELD REFINEMENT OF LiCoO2-TYPE LAYERED STRUCTURES: SEMI-QUANTITATIVE ANALYSIS OF Li CONTENTS. Advances in X-ray Analysis, 45:1–6, December 2001.

[20] Pilar Maldonado-Manso, Enrique R Losilla, María Martínez-Lara, Miguel A G Aranda, Sebastián Bruque, Fatima E Mouahid, and Mohammed Zahir. High Lithium Ionic Conductivity in the $Li_{1+x}Al_xGe_yTi_{2-x-y}(PO_4)_3$NASICON Series. Chemistry of Materials, 15(9):1879–1885, May 2003.

[21] J C M'Peko, JSC Francis, and R Raj. Impedance Spectroscopy and Dielectric Properties of Flash Versus Conventionally Sintered Yttria-Doped Zirconia Electroceramics Viewed at the Microstructural Level - M'Peko - 2013 - Journal of the American Ceramic Society - Wiley Online Library. Journal of the American . . . , 2013.

[22] Yoshinori Noguchi, Eiji Kobayashi, Larisa S Plashnitsa, Shigeto Okada, and Jun-ichi Yamaki. Fabrication and performances of all solid-state symmetric sodium battery based on NASICON-related compounds. Electrochimica Acta, 101:59–65, July 2013.

[23] Miguel A París and Jesús Sanz. Structural changes in the compounds $LiM_2{}^{IV}(PO_4)_3$ (M^{IV}=Ge, Ti, Sn, and Hf) as followed by P31 and Li7 NMR. Physical Review B, 55(21):14270–14278, June 1997.

[24] Yugang Sun. Lithium ion conducting membranes for lithium-air batteries. Nano Energy, 2:801–816, 2013.

[25] P Tarte, A Rulmont, and C Merckaert-Ansay. Vibrational spectrum of nasicon-like, rhombohedral orthophosphates $M^IM_2{}^{IV}(PO_4)_3$. Spectrochimica Acta Part A: Molecular Spectroscopy, 42(9):1009–1016, 1986.

[26] C Wert and C Zener. Interstitial Atomic Diffusion Coefficients. Physical Review, 76(8):1169–1175, 1949.

[27] Hiroshi Yamamoto, Mitsuharu Tabuchi, Tomonari Takeuchi, Hiroyuki Kageyama, and Osamu Nakamura. Ionic conductivity enhancement in $LiGe_2(PO_4)_3$ solid electrolyte. Journal Of Power Sources, 68(2):397–401, October 1997.

[28] M Zhang, K Takahashi, N Imanishi, Y Takeda, O Yamamoto, B Chi, J Pu, and J Li. Preparation and Electrochemical Properties of Li1+xAlxGe2-x(PO4)3 Synthesized by a Sol-Gel Method. Journal of The Electrochemical Society, 159(7):A1114–A1119, January 2012.

[29] Ming Zhang, Keita Takahashi, Ichiro Uechi, Yasuo Takeda, Osamu Yamamoto, Dongmin Im, Dong-Jonne Lee, Bo Chi, Jian Pu, Jian Li, and Nobuyuki Imanishi. Water-stable lithium anode with $Li_{1.4}Al_{0.4}Ge_{1.6}(PO_4)_3$-$TiO_2$ sheet prepared by tape casting method for lithium-air batteries. Journal Of Power Sources, 235(C):117–121, August 2013.

Chapter 6

Concluding Remarks

6.1 Thoughts on this Work

The work undertaken in the making of this thesis covers the spectrum from probing device level performance down to the single hop of a lithium atom that makes charge storage possible. We began our work by attempting to create a new type of charge-storage device. The solid-state supercapacitor we created by adopting discrete interfacial engineering schemes was a promising step towards realizing this new class of device. While this demonstration is in and of itself is a contribution to the field of solid-state energy storage, we determined that greater contributions could be made by undertaking study of the materials themselves.

In working with the NASICON materials in Chapters 3-5, we have found great satisfaction in being able to correlate performance with structure. It is this sort of fundamental understanding that is required to properly explain device level performance.

6.2 Future Work

While not detailed in the proceeding chapters, often during the course of this work we encountered a fork in the road, where opportunities to study interesting phenomena diverged beyond the scope of one thesis and a difficult choice had to be made. Here, we briefly list some of these opportunities that were left unexplored.

6.2.1 Sol-gel Impregnation of Conducting Networks

At the end of the work presented in Chapter 2 we knew that to continue to improve device performance, we needed to increase contact area between the conductive carbon and the solid-state electrolyte. One way that we envisioned doing this was by impregnating a woven carbon sheet with an electrolyte precursor sol, and then executing the proper heat treatments to convert the sol to a crystalline ion conductor. This, in theory, would yield a highly-conducting carbon network with low ESR in high areal contact with the solid electrolyte; a combination that should yield high specific capacitance.

We began exploring this idea but quickly ran into engineering challenges with sols not wetting the carbon surface, and the carbon structures not surviving heat treatments. We believe it may be possible to address both of these challenges by adding a thin protective coating to the carbon structure, such as by an ALD process. A 10-layer coating of Al_2O_3 may provide both oxidation protection and surface modifications such that an aqueous sol will coat the structure.

6.2.2 Alternative NASICON Chemistries

We have conducted extensive experimentation with various M cation substitutions that are not included in any work documented here because they did not “work”. By this we generally mean that these materials did not adopt the structure we have discussed in Chapters 3-5. When M cations are too big, they may force slight rotations and shifts of the framework polyhedra seen in Figure 4.1. All of the bonding is the same, but framework and conduction pathway geometry changes, and the structure is classified in a different space group with different symmetries. In the case of pure lithium tin phosphate, for example, this altered structure with monoclinic symmetry (space group: Cc) is observed at room temperature, but converts to the familiar rhombohedral symmetry (space group: $R\bar{3}c$) above 120°C. Figure 6.1 shows XRD patterns we collected over the temperature range 20°C - 250°C. The reversible phase transition is seen very clearly in this data. In an attempt to lower this transition temperature to a point where it would be irrelevant (i.e.

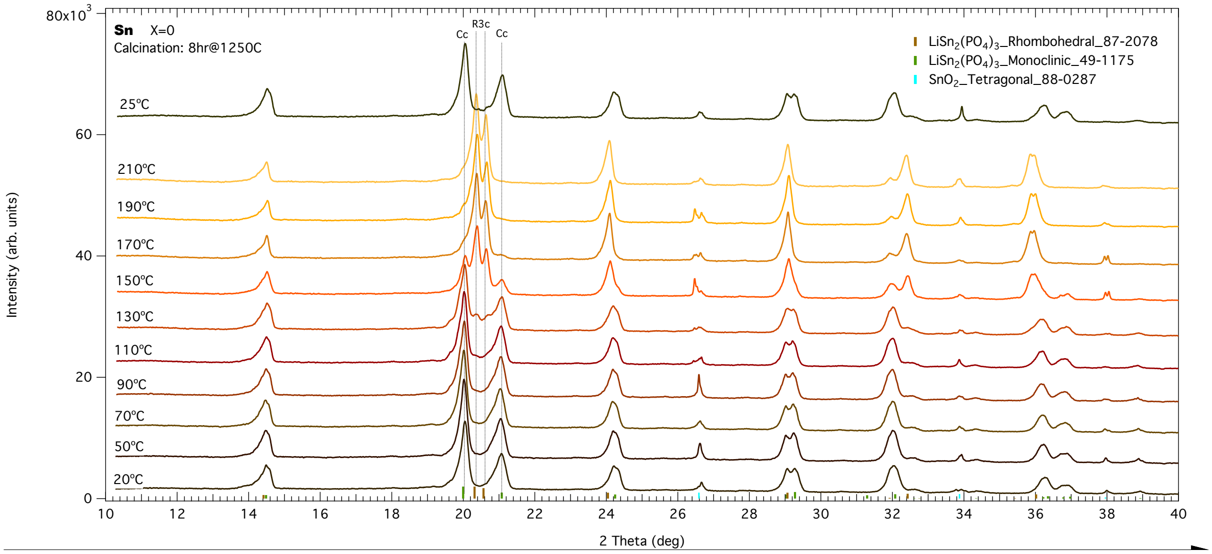

Figure 6.1: $LiSn_2(PO_4)_3$. A reversible phase transition is clearly observed, beginning around 120°C.

well below RT) and also increase conductivity through an increase in number of charge carriers, we synthesized a Ga-Sn hybrid: $Li_{1.5}Ga_{0.5}Sn_{1.5}(PO_4)_3$. Defying established logic, this material exhibited a transition temperature higher than pure $LiSn_2(PO_4)_3$, as seen in Figure 6.2. Chasing down an explanation for this could lead to fascinating new insights into the NASICON structure.

Based on insights from the work in Chapter 4, we believe that materials with the general formula $Li_{1+x}[Ga, Cr]_xZr_{2-x}(PO_4)_3$ should also be fine lithium conductors. However, we experienced difficulties in the synthesis, specifically with phase impurities. A revisitation of these systems, perhaps with better control of pH during synthesis and calcination temperatures >900°C could quite possibly yield novel materials.

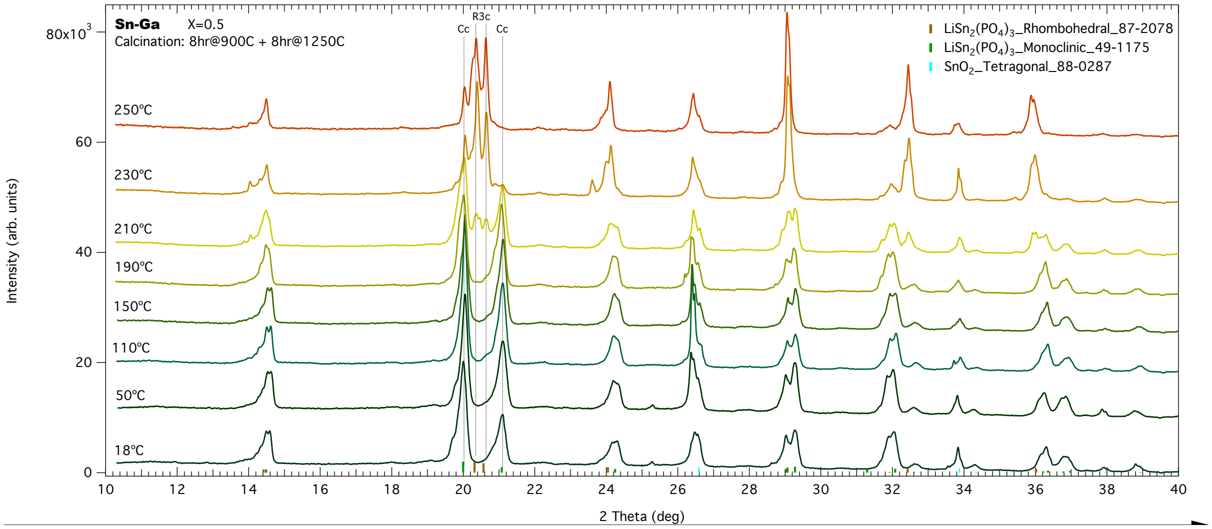

Figure 6.2: $Li_{1.5}Ga_{0.5}Sn_{1.5}(PO_4)_3$. A reversible phase transition is clearly observed, beginning around 200°C.

Complete List of References

[1] M Alami, R Brochu, J L Soubeyroux, P Gravereau, G Le Flem, and P Hagenmuller. Structure and thermal expansion of $LiGe_2(PO_4)_3$. Journal of Solid State Chemistry, 90(2):185–193, February 1991.

[2] James Alamo and Rustum Roy. Crystal chemistry of the $NaZr_2(PO_4)_3$, NZP or CTP, structure family. Journal of Materials Science, 21(2):444–450, February 1986.

[3] D P Almond, G K Duncan, and A R West. The Determination of Hopping Rates and Carrier Concentrations in Ionic Conductors by a New Analysis of Ac Conductivity. Solid State Ionics, 8(2):159–164, 1983.

[4] D P Almond and A R West. Impedance and modulus spectroscopy of "real" dispersive conductors. Solid State Ionics, 11(1):57–64, September 1983.

[5] D P Almond and A R West. The activation entropy for transport in ionic conductors. Solid State Ionics, 23(1):27–35, 1987.

[6] Glenn G Amatucci, Fadwa Badway, Aurelien Du Pasquier, and Tao Zheng. An Asymmetric Hybrid Nonaqueous Energy Storage Cell. Journal of The Electrochemical Society, 148(8):A930–A939, 2001.

[7] N Anantharamulu, K Koteswara Rao, G Rambabu, B Vijaya Kumar, Velchuri Radha, and M Vithal. A wide-ranging review on Nasicon type materials. Journal of Materials Science, 46(9):2821–2837, February 2011.

[8] Hiromichi Aono, Eisuke Sugimoto, Yoshihiko Sadaoka, N Imanaka, and Gin-ya Adachi. Ionic-Conductivity and Sinterability of Lithium Titanium Phosphate System. Solid State Ionics, 40-1:38–42, August 1990.

[9] Hiromichi Aono, Eisuke Sugimoto, Yoshihiko Sadaoka, Nobuhito Imanaka, and Gin-ya Adachi. Electrical Properties and Sinterability for Lithium Germanium Phosphate $Li_{1+x}M_xGe_{2-x}(PO_4)_3$, M=Al, Cr, Ga, Fe, Sc, and In Systems. Bulletin of the Chemical Society of Japan, 65(8):2200–2204, 1992.

[10] K Arbi, M A París, and J Sanz. Li mobility in Nasicon-type materials $LiM_2(PO_4)_3$, M = Ge, Ti, Sn, Zr and Hf, followed by 7Li NMR spectroscopy. Dalton Trans, 40(39):10195, 2011.

[11] K Arbi, M Tabellout, M Lazarraga, J Rojo, and J Sanz. Non-Arrhenius conductivity in the fast lithium conductor $Li_{1.2}Ti_{1.8}Al_{0.2}(PO_4)_3$: A Li7 NMR and electric impedance study. Physical Review B, 72(9):094302, September 2005.

[12] M Barj, G Lucazeau, and C Delmas. Raman and infrared spectra of some chromium Nasicon-type materials: Short-range disorder characterization. Journal of Solid State Chemistry, 100(1):141–150, September 1992.

[13] M Barj, H Perthuis, and P Colomban. Relations between sublattice disorder, phase transitions and conductivity in NASICON. Solid State Ionics, 9-10:845–850, December 1983.

[14] Evgenij Barsoukov and James Ross Macdonald. Impedance Spectroscopy. Theory, Experiment, and Applications. John Wiley & Sons, New Jersey, 2 edition, 2005.

[15] J P Boilot, G Collin, and P Colomban. Relation Structure Fast Ion Conduction in the Nasicon Solid-Solution. Journal of Solid State Chemistry, 73(1):160–171, March 1988.

[16] Peter G Bruce. Solid State Electrochemistry. Cambridge University Press, New York, 1 edition, June 1997.

[17] Bong Gill Choi, Jinkee Hong, Won Hi Hong, Paula T Hammond, and HoSeok Park. Facilitated Ion Transport in All-Solid-State Flexible Supercapacitors. ACS nano, 5(9):7205–7213, 2011.

[18] B E Conway. Electrochemical Supercapacitors. Scientific Fundamentals and Technological Applications. Springer, 1999.

[19] M Cretin and P Fabry. Comparative study of lithium ion conductors in the system $Li_{1+x}Al_xA_{2x}{}^{IV}$ $(PO_4)_3$ with A^{IV}=Ti or Ge and 0x07 for use as Li^+ sensitive membranes. Journal Of The European Ceramic Society, 19(16):2931–2940, December 1999.

[20] Gaelle Delaizir, Virginie Viallet, Abdelmaula Aboulaich, Renaud Bouchet, Laurence Tortet, Vincent Seznec, Mathieu Morcrette, Jean-Marie Tarascon, Patrick Rozier, and Mickael Dollé. The Stone Age Revisited: Building a Monolithic Inorganic Lithium-Ion Battery. Advanced Functional Materials, 22(10):2140–2147, February 2012.

[21] Adolfo Delgado, Mario F García-Sánchez, Jean-Claude M'Peko, A Rabdel Ruiz-Salvador, Geonel Rodríguez-Gattorno, Yuri Echevarría, and Froilan Fernández-Gutierrez. An Elementary Picture of Dielectric Spectroscopy in Solids: Physical Basis. Journal Of Chemical Education, 80(9):1062, September 2003.

[22] Jinkui Feng, Hui Xia, Man On Lai, and Li Lu. NASICON-Structured $LiGe_2(PO_4)_3$with Improved Cyclability for High-Performance Lithium Batteries. Journal Of Physical Chemistry C, 113(47):20514–20520, November 2009.

[23] J G Fletcher, A R West, and J T S Irvine. The Ac-Impedance Response of the Physical Interface Between Yttria-Stabilized Zirconia and $YBa_2Cu_3O_{7-X}$. Journal of The Electrochemical Society, 142(8):2650–2654, August 1995.

[24] E Frackowiak and F Beguin. Electrochemical storage of energy in carbon nanotubes and nanostructured carbons. Carbon, 40(10):1775–1787, 2002.

[25] Brian E Francisco, Conrad R Stoldt, and Jean-Claude M'Peko. Lithium-Ion Trapping from Local Structural Distortions in Sodium Super Ionic Conductor (NASICON) Electrolytes. Chemistry of Materials, 26(16):4741–4749, August 2014.

[26] Germà Garcia-Belmonte and Juan Bisquert. Entropy factor in the hopping frequency for ionic conduction in oxide glasses induced by energetic clustering. The Journal of Chemical Physics, 123(7):074504, 2005.

[27] Joel Irwin Gersten and Frederick William Smith. The Physics and Chemistry of Materials. Wiley New York, New York, 1 edition, 2001.

[28] Akitoshi Hayashi, S Hama, F Mizuno, K Tadanaga, T Minami, and Masahiro Tatsumisago. Characterization of Li2S-P2S5 glass-ceramics as a solid electrolyte for lithium secondary batteries. Solid State Ionics, 175(1-4):683–686, 2004.

[29] HY-P Hong. Crystal structures and crystal chemistry in the system $Na_{1+x}Zr_2Si_xP_{3x}O_{12}$. Materials Research Bulletin, 11(2):173–182, 1976.

[30] L. Hu, J.W. Choi, Y. Yang, S. Jeong, F. La Mantia, L.F. Cui, and Y. Cui. Highly conductive paper for energy-storage devices. Proceedings of the National Academy of Sciences, 106(51):21490–21494, 2009.

[31] Robert Huggins. Advanced Batteries. Materials Science Aspects. Springer, New York, 1 edition, November 2008.

[32] M M Khandpekar, R K Kushwaha, and S P Pati. Design, fabrication, and evaluation of a 5 F-5 V prototype of solid-state PANI based supercapacitor. Solid-State Electronics, 62(1):156–160, 2011.

[33] R Kotz, M Hahn, and R Gallay. Temperature behavior and impedance fundamentals of supercapacitors. Journal Of Power Sources, 154(2):550–555, 2006.

[34] A Krause, P Kossyrev, M Oljaca, S Passerini, M Winter, and A Balducci. Electrochemical double layer capacitor and lithium-ion capacitor based on carbon black. Journal Of Power Sources, 196(20):8836–8842, October 2011.

[35] Seung Woo Lee, Junhyung Kim, Shuo Chen, Paula T Hammond, and Yang Shao-Horn. Carbon Nanotube/Manganese Oxide Ultrathin Film Electrodes for Electrochemical Capacitors. ACS nano, 4(7):3889–3896, 2010.

[36] John H Lehman, Mauricio Terrones, Elisabeth Mansfield, Katherine E Hurst, and Vincent Meunier. Evaluating the characteristics of multiwall carbon nanotubes. Carbon, 49(8):2581–2602, July 2011.

[37] S Li. Phase relationships and electrical conductivity of $Li_{1+x}Ge_{2-x}Al_xP_3O_{12}$ and $Li_{1+x}Ge_{2-x}Cr_xP_3O_{12}$ systems. Solid State Ionics, 28-30:1265–1270, September 1988.

[38] Qiang Liu, Munir H Nayfeh, and Siu-Tung Yau. Brushed-on flexible supercapacitor sheets using a nanocomposite of polyaniline and carbon nanotubes. Journal Of Power Sources, 195(21):7480–7483, November 2010.

[39] Enrique R Losilla, Miguel A G Aranda, Sebastián Bruque, Miguel A París, Jesús Sanz, and Anthony R West. Understanding Na Mobility in NASICON Materials: A Rietveld, 23Na and 31P MAS NMR, and Impedance Study. Chemistry of Materials, 10(2):665–673, February 1998.

[40] F Lufrano and P Staiti. Performance improvement of Nafion based solid state electrochemical supercapacitor. Electrochimica Acta, 49(16):2683–2689, 2004.

[41] D Ingersoll D H Doughty M A Rodriguez. RIETVELD REFINEMENT OF LiCoO2-TYPE LAYERED STRUCTURES: SEMI-QUANTITATIVE ANALYSIS OF Li CONTENTS. Advances in X-ray Analysis, 45:1–6, December 2001.

[42] Pilar Maldonado-Manso, Enrique R Losilla, María Martínez-Lara, Miguel A G Aranda, Sebastián Bruque, Fatima E Mouahid, and Mohammed Zahir. High Lithium Ionic Conductivity in the $Li_{1+x}Al_xGe_yTi_{2-x-y}(PO_4)_3$NASICON Series. Chemistry of Materials, 15(9):1879–1885, May 2003.

[43] Ana Martinez, José M Rojo, Juan E Iglesias, Jesús Sanz, and Rosa M Rojas. Formation Process of $LiSn_2(PO_4)_3$, a Monoclinically Distorted NASICON-Type Structure. Chemistry of Materials, 6(10):1790–1795, October 1994.

[44] Ana Martinez-Juarez, Carlos Pecharromán, Juan E Iglesias, and José M Rojo. Relationship between Activation Energy and Bottleneck Size for Li^+ Ion Conduction in NASICON Materials of Composition LiMM'$(PO_4)_3$; M, M'= Ge, Ti, Sn, Hf. The Journal of Physical Chemistry B, 102(2):372–375, 1998.

[45] Keiichi Minami, Fuminori Mizuno, Akitoshi Hayashi, and Masahiro Tatsumisago. Lithium ion conductivity of the Li2S-P2S5 glass-based electrolytes prepared by the melt quenching method. Solid State Ionics, 178(11-12):837–841, 2007.

[46] F Mizuno, Akitoshi Hayashi, K Tadanaga, and Masahiro Tatsumisago. High lithium ion conducting glass-ceramics in the system Li2S-P2S5. Solid State Ionics, 177(26-32):2721–2725, 2006.

[47] J C M'Peko, JSC Francis, and R Raj. Impedance Spectroscopy and Dielectric Properties of Flash Versus Conventionally Sintered Yttria-Doped Zirconia Electroceramics Viewed at the Microstructural Level - M'Peko - 2013 - Journal of the American Ceramic Society - Wiley Online Library. Journal of the American . . . , 2013.

[48] Hiromasa Muramatsu, Akitoshi Hayashi, Takamasa Ohtomo, Sigenori Hama, and Masahiro Tatsumisago. Structural change of Li2S-P2S5 sulfide solid electrolytes in the atmosphere. Solid State Ionics, 182(1):116–119, 2011.

[49] Yoshinori Noguchi, Eiji Kobayashi, Larisa S Plashnitsa, Shigeto Okada, and Jun-ichi Yamaki. Fabrication and performances of all solid-state symmetric sodium battery based on NASICON-related compounds. Electrochimica Acta, 101:59–65, July 2013.

[50] Mark E Orazem and Bernard Tribollet. Electrochemical Impedance Spectroscopy. John Wiley & Sons, October 2011.

[51] Miguel A París and Jesús Sanz. Structural changes in the compounds $LiM_2{}^{IV}(PO_4)_3$ (M^{IV}=Ge, Ti, Sn, and Hf) as followed by P31 and Li7 NMR. Physical Review B, 55(21):14270–14278, June 1997.

[52] DY Qu and H Shi. Studies of activated carbons used in double-layer capacitors. Journal Of Power Sources, 74(1):99–107, 1998.

[53] D Tran Qui, S Hamdoune, J L Soubeyroux, and E Prince. Neutron powder diffraction study of solid solution $Li_{1+x}Ti_{2x}In_xP_3O_{12}$. Journal of Solid State Chemistry, 72(2):309–315, February 1988.

[54] Yuria Saito, Kazuaki Ado, Takashi Asai, Hiroyuki Kageyama, and Osamu Nakamura. Ionic conductivity of NASICON-type conductors Na1. 5M0. 5Zr1. 5 (PO4) 3 (M: Al3+, Ga3+, Cr3+, Sc3+, Fe3+, In3+, Yb3+, Y3+). Solid State Ionics, 58(3-4):327–331, 1992.

[55] R D Shannon. Revised effective ionic radii and systematic studies of interatomic distances in halides and chalcogenides. Acta Crystallographica Section A, 32(5):751–767, September 1976.

[56] Hideaki Shinohara, Yoshihiro Yamakita, and Koichi Ohno. Raman spectra of polycyclic aromatic hydrocarbons. Comparison of calculated Raman intensity distributions with observed spectra for naphthalene, anthracene, pyrene, and perylene. Journal Of Molecular Structure, 442(1):221–234, 1998.

[57] Riccardo Signorelli, Daniel C Ku, John G Kassakian, and Joel E Schindall. Electrochemical Double-Layer Capacitors Using Carbon Nanotube Electrode Structures. Proceedings of the IEEE, 97(11):1837–1847, 2009.

[58] Graeme A Snook, Pon Kao, and Adam S Best. Conducting-polymer-based supercapacitor devices and electrodes. Journal Of Power Sources, 196(1):1–12, 2011.

[59] Dang Sheng Su and Robert Schloegl. Nanostructured Carbon and Carbon Nanocomposites for Electrochemical Energy Storage Applications. Chemsuschem, 3(2):136–168, 2010.

[60] Yugang Sun. Lithium ion conducting membranes for lithium-air batteries. Nano Energy, 2:801–816, 2013.

[61] M TACHEZ, JP MALUGANI, R MERCIER, and G ROBERT. IONIC-CONDUCTIVITY OF AND PHASE-TRANSITION IN LITHIUM THIOPHOSPHATE LI3PS4. Solid State Ionics, 14(3):181–185, 1984.

[62] P Tarte, A Rulmont, and C Merckaert-Ansay. Vibrational spectrum of nasicon-like, rhombohedral orthophosphates $M^I {M_2}^{IV}(PO_4)_3$. Spectrochimica Acta Part A: Molecular Spectroscopy, 42(9):1009–1016, 1986.

[63] James Trevey, Jum Suk Jang, Yoon Seok Jung, Conrad R Stoldt, and Se-Hee Lee. Glass-ceramic Li2S-P2S5 electrolytes prepared by a single step ball billing process and their application for all-solid-state lithium-ion batteries. Electrochemistry Communications, 11(9):1830–1833, 2009.

[64] B WANG, M Greenblatt, S Wang, and S J Hwu. Ionic conductivity of lithium titanium phosphate LithiumTi2 (PO4)3(0.2 .ltoreq. x .ltoreq. 1.72) with NASICON-related structures. Chemistry of Materials, 5(1):23–26, January 1993.

[65] C Wert and C Zener. Interstitial Atomic Diffusion Coefficients. Physical Review, 76(8):1169–1175, 1949.

[66] J M Winand, A Rulmont, and P Tarte. Ionic conductivity of the $Na_{1+x}{M_x}^{III}Zr_{2-x}(PO_4)_3$ systems (M = Al, Ga, Cr, Fe, Sc, In, Y, Yb). Journal of Materials Science, 25(9):4008–4013, September 1990.

[67] Jean-Marc Winand, André Rulmont, and Pierre Tarte. Nouvelles solutions solides $L^I(M^{IV})_{2x}(N^{IV})_x(PO_4)_3$ (L = Li,Na M,N = Ge,Sn,Ti,Zr,Hf) Synthèse et étude par diffraction x et conductivité ionique. Journal of Solid State Chemistry, 93(2):341–349, August 1991.

[68] Bin Xu, Feng Wu, Shi Chen, Cunzhong Zhang, Gaoping Cao, and Yusheng Yang. Activated carbon fiber cloths as electrodes for high performance electric double layer capacitors. Electrochimica Acta, 52(13):4595–4598, 2007.

[69] Hiroshi Yamamoto, Mitsuharu Tabuchi, Tomonari Takeuchi, Hiroyuki Kageyama, and Osamu Nakamura. Ionic conductivity enhancement in $LiGe_2(PO_4)_3$ solid electrolyte. Journal Of Power Sources, 68(2):397–401, October 1997.

[70] A B Yaroslavtsev and I A Stenina. Complex phosphates with the NASICON structure (M x A2(PO4)3). Russian Journal of Inorganic Chemistry, 51(S1):S97–S116, January 2006.

[71] JJ Yoo, K Balakrishnan, J Huang, V Meunier, BG Sumpter, A Srivastava, M Conway, AL Mohana Reddy, J Yu, and R Vajtai. Ultrathin Planar Graphene Supercapacitors. Nano Letters, 11:1423–1427, 2011.

[72] Haijun Yu, Jihuai Wu, Leqing Fan, Kaiqing Xu, Xin Zhong, Youzhen Lin, and Jianming Lin. Improvement of the performance for quasi-solid-state supercapacitor by using PVA-KOH-KI polymer gel electrolyte. Electrochimica Acta, 56(20):6881–6886, 2011.

[73] K Zhang, L Zhang, and X Zhao. Graphene/polyaniline nanofiber composites as supercapacitor electrodes. Chemistry of Materials, 2010.

[74] LL Zhang and XS Zhao. Carbon-based materials as supercapacitor electrodes. Chemical Society Reviews, 38(9):2520–2531, 2009.

[75] M Zhang, K Takahashi, N Imanishi, Y Takeda, O Yamamoto, B Chi, J Pu, and J Li. Preparation and Electrochemical Properties of Li1+xAlxGe2-x(PO4)3 Synthesized by a Sol-Gel Method. Journal of The Electrochemical Society, 159(7):A1114–A1119, January 2012.

[76] Ming Zhang, Keita Takahashi, Ichiro Uechi, Yasuo Takeda, Osamu Yamamoto, Dongmin Im, Dong-Jonne Lee, Bo Chi, Jian Pu, Jian Li, and Nobuyuki Imanishi. Water-stable lithium anode with $Li_{1.4}Al_{0.4}Ge_{1.6}(PO_4)_3$-$TiO_2$ sheet prepared by tape casting method for lithium-air batteries. Journal Of Power Sources, 235(C):117–121, August 2013.

[77] Xin Zhao, Beatriz Mendoza Sanchez, Peter J Dobson, and Patrick S Grant. The role of nanomaterials in redox-based supercapacitors for next generation energy storage devices. Nanoscale, 3(3):839–855, 2011.